

Fluorescent sensor proteins to assess the cellular uptake of therapeutic peptides and small molecules

THÈSE N° 7413 (2017)

PRÉSENTÉE LE 20 JANVIER 2017

À LA FACULTÉ DES SCIENCES DE BASE

LABORATOIRE D'INGÉNIERIE DES PROTÉINES

PROGRAMME DOCTORAL EN CHIMIE ET GÉNIE CHIMIQUE

ÉCOLE POLYTECHNIQUE FÉDÉRALE DE LAUSANNE

POUR L'OBTENTION DU GRADE DE DOCTEUR ÈS SCIENCES

PAR

Silvia SCARABELLI

acceptée sur proposition du jury:

Prof. U. Röthlisberger, présidente du jury

Prof. K. Johnsson, directeur de thèse

Dr T. Vorherr, rapporteur

Dr S. Matile, rapporteur

Dr C. Heinis, rapporteur



ÉCOLE POLYTECHNIQUE
FÉDÉRALE DE LAUSANNE

Suisse
2017

Abstract

The determination of cell membrane permeability and of the absorption and clearance rates is an important step in the pharmacokinetic profiling of a new drug candidate. In a similar way, research in cell biology relies on the development of cell penetrating biochemical probes allowing to study and interfere with cellular functions and physiology.

A variety of methods have been developed to estimate the ability of molecules to enter the intracellular space. They are based either on artificial membranes or on cellular models, with consequently different abilities to mimic the cellular permeation mechanisms. However, these techniques are often laborious, expensive and have to be combined to get a reliable characterization of the properties of the molecule of interest.

This thesis introduces a new strategy to evaluate real-time absorption and clearance kinetics of different classes of molecules in living cells. The approach is based on the use of intracellular single-chain FRET-based biosensors with a versatile modular design. First, a proof-of-concept bioprobe for inhibitors of the enzyme human carbonic anhydrase II (HCAII) was developed and optimized for intracellular use: the cell-entry dynamics of a selection of well-known sulfonamide drugs was compared and monitored in real time. Then, we adapted the design of the sensory protein to generate a label-free biosensor for inhibitors of the p53-HDM2 interaction, a highly studied protein-protein interaction in cancer biology. The permeability and the kinetics of cell entry and washout of various underivatized small molecule and peptidic inhibitors could be measured.

This thesis represents a step towards the introduction of a general approach for a low-cost, rapid and minimally invasive evaluation of molecular permeabilities in the cell type of choice. Their modular design lends itself to be adapted to the detection of other families of molecules, provided that a binding protein for the molecule of interest is known.

Keywords

Permeability, FRET-based sensor protein, cellular absorption rate, cellular clearance, HCAII, p53-HDM2 interaction

Riassunto

La determinazione della permeabilità, della velocità di assorbimento e di efflusso cellulari è una delle fasi più importanti nella valutazione delle proprietà farmacocinetiche di un nuovo candidato farmaco. Similmente, in biologia cellulare lo sviluppo di sensori biochimici permeabili è essenziale per studiare ed interferire con le funzioni e la fisiologia delle cellule.

Attualmente esistono una varietà di metodi per stimare la capacità delle molecole ad accedere lo spazio intracellulare. Tali metodi sono basati su membrane artificiali o modelli cellulari, e conseguentemente permettono di simulare i meccanismi di penetrazione cellulare in modo più o meno appropriato. Ciononostante queste tecniche sono spesso laboriose, costose e necessitano di essere combinate per fornire una caratterizzazione completa della molecola di interesse.

La presente tesi introduce una nuova strategia per valutare in tempo reale in cellule viventi il grado e la velocità di assorbimento ed efflusso di diverse classi di molecole. L'approccio si fonda sull'uso di biosensori proteici modulari e a catena unica basati sul fenomeno di FRET. In primo luogo, un sensore per inibitori dell'enzima anidrase carbonica umana II (HCAII) è stato sviluppato ed ottimizzato per uso intracellulare: le dinamiche di penetrazione cellulare di note sulfonammidi hanno potuto essere comparate e monitorate in tempo reale. Successivamente, il design della proteina è stato modificato per generare un biosensore codificabile geneticamente per il rilevamento di inibitori dell'interazione tra p53 e HDM2, oggetto di attenti studi in biologia del cancro. Il sensore ha permesso di misurare la permeabilità e le cinetiche di ingresso ed fuoriuscita cellulare di diversi piccole molecole e peptidi non-derivatizzati.

I biosensori presentati in questo lavoro di tesi costituisce un progresso nell'introduzione di un approccio generale per una valutazione low-cost, veloce e non-invasiva delle permeabilità molecolari sulla specie cellulare di interesse. Il design modulare si presta ad essere adattato al rilevamento di altre classi di molecole per le quali esiste una proteina legante.

Parole chiave

Permeabilità, biosensore, FRET, velocità di assorbimento cellulare, velocità di efflusso cellulare, HCAII, interazione tra p53 e HDM2.

Acknowledgements

First and foremost, I would like to thank my advisor Professor Kai Johnsson for offering me the opportunity to make my PhD in his group, a unique collection of front-rank scientists with pronounced social intelligence. I am particularly grateful for his trust and the sincere consideration he always showed for my ideas since our first conversation, when I was still an inexperienced Master student. I will always hold him in high regard for his brilliant mind, approachable personality and sincere humility.

I wish to thank Dr. Thomas Vorherr for his scientific advices and his team for having contributed to my thesis project by providing small molecules and peptides for the experiments on the p53-based sensor project.

Moreover, I would like to thank Professor Ruud Hovius for having repeatedly shared with me his boundless scientific knowledge and, most importantly, for taking the time and the patience to review my thesis.

I also wish to thank Dr. Fabien Kuttler from the Biomolecular Screening Facility of EPFL for his kindness and the huge amount of time he spent to train me on the InCell 2200 microscope and on the softwares Knime and CellProfiler.

Very special thanks to all the beautiful personalities of the Johnsson group for having created a wonderful family-like atmosphere, in which both science- and life-related exchanges have been the order of the day. I am deeply grateful for the time every single member of the group took to answer my questions and for the moral support I received from many sides in difficult moments.

This thesis is dedicated to:

- *The ATP synthase protein complex, for the absolute perfection of its extraordinary working mechanism which fascinated me so much that I decided to study Biochemistry many years ago;*
- *Professor Ludovic Jullien, Director of the Department of Chemistry of the École Normale Supérieure of Paris, for having been a precious mentor: his help has been fundamental for me to find my way;*
- *Diego, for the boundless affection and constant enlightenment and for being my inexhaustible source of force and determination.*

Contents

Abstract	iii
Keywords	iii
Riassunto	v
Parole chiave.....	v
Aknowledgements	vii
List of Figures	xiii
List of Tables.....	xvii
List of Abbreviations	xix
Chapter 1 Introduction	1
1.1 Cellular uptake of molecules	1
1.1.1 Relevance in drug development and background	1
1.1.2 Methods to assess drug permeability <i>in vitro</i>	2
1.1.3 Methods to achieve the cellular delivery of small molecules	5
1.2 FRET-based biosensors.....	8
1.2.1 Semisynthetic FRET-based sensors, previous work.....	9
Chapter 2 Aim of the project	13
Chapter 3 HCA-based sensor for sulfonamides	15
3.1 Carbonic Anhydrases, an introduction	15
3.2 Sensor design	16
3.2.1 The protein moiety	17
3.2.2 SNAP-tag labelling molecules	17
3.3 Sensing sulfonamides <i>in vitro</i>	18
3.3.1 SNAP-tag labeling <i>in cellulo</i> with the substrates.....	19
3.3.2 Sensor-labelling reactivity of the substrates <i>in vitro</i>	20
3.3.3 <i>In vitro</i> titration of sulfonamide inhibitors.....	21
3.3.4 <i>In vitro</i> opening kinetics of the sensor in presence of sulfonamide inhibitors.....	24

3.4	Sensing sulfonamides <i>in cellulo</i>	25
3.4.1	<i>In cellulo</i> titration of sulfonamide inhibitors	26
3.4.2	<i>In cellulo</i> kinetic characterization of the sensor in presence of sulfonamide inhibitors	27
3.4.3	Conclusions and outlook.....	29
Chapter 4 Label-free p53-based sensor for inhibitors of the p53-HDM2 interaction		31
4.1	Introduction.....	31
4.1.1	Protein-protein interactions as therapeutic targets	31
4.1.2	p53 and HDM2	32
4.2	Sensor design	34
4.3	Sensing inhibitors of the interaction p53-HDM2 <i>in vitro</i>	35
4.3.1	<i>In vitro</i> titration of inhibitors of the p53-HDM2 interaction.....	35
4.3.2	<i>In vitro</i> opening kinetics of the sensor in presence of inhibitors of the interaction p53-HDM2	38
4.4	Sensing inhibitors of the interaction p53-HDM2 <i>in cellulo</i>	39
4.4.1	<i>In cellulo</i> titration of the p53-HDM2 interaction inhibitors	40
4.4.2	<i>In cellulo</i> kinetic characterization of the sensor in presence of inhibitors of the interaction p53-HDM2	41
4.4.3	Conclusions and outlook.....	42
Chapter 5 General conclusions		45
Chapter 6 Materials and Methods		47
6.1	Chemical synthesis	47
6.1.1	General information	47
6.1.2	Synthesis of compounds	47
6.2	Biology	56
6.2.1	Cloning.....	56
6.2.2	Sensor expression and purification from HEK293 EBNA1 cells	58
6.2.3	Determination of the HCA sensor labeling kinetics <i>in vitro</i>	59
6.2.4	Titration of analytes <i>in vitro</i>	59
6.2.5	Determination of the sensor's opening kinetic <i>in vitro</i>	61
6.2.6	Semi stable adherent cell line generation.....	61
6.2.7	Determination of the cell permeability of SNAP-tag substrates	62
6.3	Microscopy	62
6.3.1	General information	62

6.3.2 Titration of analytes <i>in cellulo</i>	65
6.3.3 Cell entry and washout kinetics <i>in cellulo</i>	66
References	67
Curriculum Vitae	73

List of Figures

Figure 1:1 Schematic representation of <i>in vivo</i> barriers to drug delivery to the target. Adapted from Kerns <i>et al.</i> ¹⁰	1
Figure 1:2 Scematic illustration of the PVPA barrier structure, where small and large liposomes are deposited on the membrane filter. Adapted from Gomes <i>et al.</i> ¹⁶	3
Figure 1:3 Schematic representation of the PAMPA experiment. Adapted from Kerns <i>et al.</i> ²⁰	3
Figure 1:4 Schematic representation of the major permeability mechanisms. Adapted from Kerns <i>et al.</i> ²⁴	4
Figure 1:5 The comparison between Caco-2 and PAMPA assays provides insight on the permeability mechanisms of a given molecule. Adapted from Kerns <i>et al.</i> ²⁰	5
Figure 1:6 Schematic representation of the possible mechanisms of cellular entry of cell penetrating peptides. Adapted from Ramsey <i>et al.</i> ⁴⁰ . 7	
Figure 1:7 Schematic representation of the specific and orthogonal labelling reactions of SNAP and CLIP fusion proteins respectively with BG and BC derivatives. Adapted from Gautier <i>et al.</i> ⁴⁷	9
Figure 1:8 Design and working principle of the SNIFITs based on the FRET between a fluorescent protein (FP) and a synthetic fluorophore introduced by SNAP-labelling (red star) (A) or on the FRET between two synthetic fluorophores introduced by orthogonal labelling of SNAP and CLIP-tag (red and green star respectively) (B). Adapted from Brun <i>et al.</i> ⁴⁴	10
Figure 3:1 Schematic representation of the Zn-bound HCAII active site in presence of CO ₂ (A), bicarbonate (B) and an arylsulfonamide inhibitor (C). Adapted from Krishnamurthy, <i>et al.</i> ⁵⁷	16
Figure 3:2 Design and working mechanism of the HCA-based sensor....	17
Figure 3:3 Final structure of the substrates for SNAP-tag labelling of the HCA-based sensor.	18
Figure 3:4 SDS-PAGE of the HCA-based sensor protein purified from HEK 293 cells.	18
Figure 3:5 Fluorescence scan of an SDS-PAGE of the lysates of SNAP-CLIP cell line incubated with the SNAP-substrates. [a]: In the lysate of cells treated with SNAP-Cell Block there is no labelling with TMR-Star. The fluorescence detected in the TMR-channel is due to the bleed-through of the SiR signal; the labelling yield for the other substrates was adjusted taking into consideration this effect.....	19
Figure 3:6 Sensor-labelling yields achieved by the substrates over time.....	20

Figure 3:7 Fluorescence titration curve of methazolamide with the HCA-based sensor labelled with different substrates. Each plot shows the ratio donor (CFP) over acceptor (YPet) emission against the concentration of inhibitor.	21
Figure 3:8 (A) Fluorescence titration curve of different inhibitors with the HCA-based sensor labelled with the substrate 3b BG-C ₆ -EG ₂ -pSA. Each plot shows the ratio donor (CFP) over acceptor (YPet) emission against the concentration of inhibitor; the data were fitted to a single-site binding isotherm (cfr. Chapter 6.2.4). (B) Fluorescence emission spectra of the HCA-based sensor in presence of different concentrations of ethoxzolamide. (C) Chemical structures of the HCA inhibitors used.	22
Figure 3:9 Fluorescence emission intensities of CFP and YPet and titration curve of the HCA-based sensor in presence of varying the concentration of methazolamide. The values of <i>C50</i> and <i>KD comp</i> for methazolamide are indicated by dashed lines.	23
Figure 3:10 Example of opening kinetics <i>in vitro</i> of the HCA-based sensor labelled with 3b in presence of methazolamide 300 μ M or HEPES buffer.	24
Figure 3:11 Example of microscopy images of the U2OS cell line expressing the HCA-based sensor and labelled with the compound 3b . After CFP excitation, the CFP emission image (A) and the YPet emission image (B) were registered.....	25
Figure 3:12 <i>In cellulo</i> fluorescence titration curve of different inhibitors with the HCA-based sensor labelled with the substrate 3b BG-C ₆ -EG ₂ -pSA.	26
Figure 3:13 (A) Opening kinetics measured by live cell imaging of the intracellular HCA-based sensor labelled with 3b in presence of acetazolamide 300 μ M, methazolamide 300 μ M, compound 5 or HBSS buffer. (B) Closing kinetics after removal of the inhibitors and after incubation with fresh HBSS buffer.	27
Figure 4:1 Schematic representation of covalent linkages to lock α -helices in peptides. Adapted from Jamieson <i>et al.</i> ⁹⁸	32
Figure 4:2 Frequency of mutations, deletions and combination of alterations in the genes of p53 and MDM2 in cancers. Adapted from Burgess <i>et al.</i> ¹⁰⁹	33
Figure 4:3 Crystal structure of HDM2 ₁₇₋₁₂₅ (grey) in complex with p53 ₁₅₋₂₉ (red). The C-terminus of the p53 ₁₅₋₂₉ -peptide is shown in green and the N-terminus of HDM2 ₁₇₋₁₂₅ is shown in blue. The side chains of the triad of p53 amino acids crucial for the interaction with HDM2 are coloured in yellow (PDB: 1YCR ¹¹⁵).	34
Figure 4:4 Design and working mechanism of the p53-based sensor.....	35
Figure 4:5 SDS-PAGE of the p53-based sensor protein purified from HEK 293 cells.	35

Figure 4:6 Chemical structures of the inhibitors of the interaction p53-HDM2 employed in the experiments.	36
Figure 4:7 (A) Fluorescence titration curve of different inhibitors with the p53-based sensor. Each plot shows the ratio donor (CFP) over acceptor (YPet) emission against the concentration of inhibitor; the data were fitted to a single-site binding isotherm or to a Hill's equation (cfr. Chapter 6.2.4). (B) Fluorescence emission spectra of the p53-based sensor in presence of different concentrations of sMTide CIS.	37
Figure 4:8 Example of opening kinetics <i>in vitro</i> of the p53-based sensor in presence of the inhibitors or HEPES buffer.	38
Figure 4:9 Example of microscopy images of the U2OS cell line expressing the p53-based sensor. After CFP excitation, the CFP emission image (A) and the YPet emission image (B) were registered.	39
Figure 4:10 <i>In cellulo</i> fluorescence titration curve of different inhibitors with the p53-based sensor.	40
Figure 4:11 Microscopy images of the U2OS cell line 2h after incubation with sMTide CIS 40 μ M. After CFP excitation, the CFP emission image (A) and the YPet emission image (B) were registered.	40
Figure 4:12 Opening kinetics measured by live cell imaging of the intracellular p53-based sensor in presence of (A) 5CGU 100 μ M, Nutlin 3a 100 μ M or (C) sMTide CIS 10 μ M, D-peptide 10 μ M or HBSS buffer. (B) Closing kinetics after removal of the small molecule inhibitors and after incubation with fresh HBSS buffer.	41
Figure 6:1 Example of microscopy image (YPet emission) of the U2OS cell line expressing the HCA-based sensor.	63
Figure 6:2 Outline of the cells identified after the first image manipulation modules.	63
Figure 6:3 Outline of the 5 pixels-expanded cells.	63
Figure 6:4 Outline of the 15 pixels-expanded cells.	64
Figure 6:5 Outline of the regions included between the 15 pixels and the 5 pixels-expanded cells.	64
Figure 6:6 Assignment of an ID number to each cell.	64
Figure 6:7 (A) Overlay of the outlines of the cells (green), the 5 pixels-expanded cells (red) and the 15 pixels-expanded cells (blue). As background, the region included between the red and the blue line was used. (B) Output table summarizing the average intensity values per cell and per time. (C) Output table of the mathematical analysis of the data collected in (B).	65

List of Tables

Table 3:1 <i>In vitro</i> C ₅₀ , <i>KD comp</i> and <i>KD</i> of the inhibitors for the HCA-based sensor labelled with 3b . The reference <i>KD</i> are for HCAII. The values of <i>KD</i> for each analyte was calculated using Equation 3:1 (see below).	23
Table 3:2 <i>In vitro</i> opening half-lives at 37°C of the HCA- based sensor labelled with 3b in presence of saturating concentrations of inhibitors.	24
Table 3:3 Comparison between <i>in cellulo</i> and <i>in vitro</i> C ₅₀ s of the HCA-inhibitors for the sensor labelled with 3b .. Error! Bookmark not defined.	
Table 3:4 Opening half-lives measured <i>in cellulo</i> and <i>in vitro</i> of the HCA-based sensor labelled with 3b in presence of saturating concentrations of inhibitors.	28
Table 4:1 Sequences of the p53 ₁₅₋₂₉ -peptide and of the peptide inhibitors employed in the experiments. The <i>i</i> , <i>i</i> +7 isomeric stapling sites in sMTide CIS are indicated with X _R and X _S . D-amino acids are indicated in lowercase letters. W _{6-Cl} is a tryptophan derivatized with a Cl on carbon-6, f _{CF3} is a <i>para</i> -trifluoromethyl derivatized D-phenylalanine.	36
Table 4:2 <i>In vitro</i> C ₅₀ , <i>KD comp</i> and <i>KD</i> of the analytes for the p53-based sensor. The reference <i>KD</i> were either published for analogues of the peptide used or calculated by the coworkers at Novartis by TR-FRET assay (displacement of N-terminally Cy5- labelled p53(18-26)). The solubility limits were calculated: [a] by the coworkers at Novartis ¹²⁵ , at pH=6.8; [b] in our laboratory by light absorbance at 280 nm, at pH=7.2.	37
Table 4:3 <i>In vitro</i> opening half-lives of the first component of the bi-exponential fitting function of the p53- based sensor in presence of inhibitors at 37°C.	38
Table 4:4 Comparison between <i>in cellulo</i> and <i>in vitro</i> C ₅₀ s of the p53-HDM2 interaction inhibitors.	40
Table 4:5 Comparison between the opening half-lives measured <i>in cellulo</i> and <i>in vitro</i> of the p53-based sensor in presence of inhibitors.	42

List of Abbreviations

ACN	acetonitrile
ADMET	absorption, distribution, metabolism, excretion and toxicity
AMP	antimicrobial peptide
BBB	blood-brain barrier
BCS	Biopharmaceutics Classification System
BG	benzylguanine
BP	binding protein
BSA	bovine serum albumine
Caco	Caucasian colon adenocarcinoma
CFP	cyan fluorescent protein
CP	chloropyrimidine
CPP	cell penetrating peptide
DBU	1,8-Diazabicyclo[5.4.0]undec-7-ene
DIPEA	N,N-diisopropylethylamine
DMEM	Dulbecco's modified eagle medium
DMSO	dimethyl sulfoxide
DNA	deoxyribonucleic acid
EDC	1-Ethyl-3-(3-dimethylaminopropyl)carbodiimide
eDHFR	<i>E. Coli</i> dihydrofolate reductase
EDTA	ethylenediaminetetraacetic acid
EG	ethylene glycol
ESI	electron spray ionization
FDA	Food and Drug Administration
FP	fluorescent protein
FRET	fluorescence resonance energy transfer
GABA	γ -aminobutyric acid
hAGT	O ⁶ -alkylguanine-DNA alkyltransferase

HBSS	Hank's balanced salt solution
HBTU	N,N,N',N'-Tetramethyl-O-(1H-benzotriazol-1-yl)uronium hexafluorophosphate
HCA	human carbonic anhydrase
HDM2	human double minute 2
HEK293	human embryonic kidney cells 293
HEPES	4-(2-hydroxyethyl)-1-piperazineethanesulfonic acid
HIV	human immunodeficiency virus
HOBt	hydroxybenzotriazole
HRMS	high resolution mass spectrometry
IAM-HPLC	immobilized artificial membrane – high pressure liquid chromatography
iGluR5	ionotropic glutamate receptor 5
LC	liquid chromatography
MDCK	madin darby canine kidney
MS	mass spectrometry
mSA	<i>meta</i> -sulfonamide
Ni-NTA	nickel-nitriloacetic acid
NMR	nuclear magnetic resonance
PAMPA	parallel artificial membrane permeability assay
PBS	phosphate buffered saline
PEI	polyethylenimine
PK	pharmacokinetics
PPI	protein-protein interaction
pSA	<i>para</i> -sulfonamide
PVPA	phospholipid vesicle-based permeability assay
RPMI	Roswell Park Memorial Institute
SDS-PAGE	sodium dodecyl sulfate polyacrilamide gel electrophoresis
siRNA	small interfering ribonucleic acid
SNIFIT	SNAP-tag based indicator protein with a fluorescent intramolecular tether

SPR	structure-property relationship
TAT	transactivator
Tf	transferrin
TFA	trifluoroacetic acid
TfR	transferrin receptor
TMR	tetramethylrhodamine
TSTU	O-(N-Succinimidyl)-N,N,N',N'-tetramethyluronium tetrafluoroborate
UCA	ultrasound contrast agent
UV	ultraviolet
YPet	yellow fluorescent protein

Chapter 1 Introduction

Cells membranes serve as biological selective barriers, permeable mainly to small, hydrophobic molecules. Over the years scientists from different disciplines (chemistry, biology, material science, physics and engineering) have developed various tools and techniques to circumvent this limitation, with the aim to observe and interfere with cellular processes. DNA¹, siRNA^{2, 3}, proteins^{4, 5}, quantum dots⁶, radiotracers, magnetic resonance imaging contrast agents⁷ are just some examples of macromolecules that have been successfully delivered to the intracellular environment. Despite the richness of techniques and applications and the attention that they would deserve, the work presented here focuses on the cellular uptake of small molecules and peptides which represent by far the biggest families of molecules employed for therapeutic applications.

1.1 Cellular uptake of molecules

1.1.1 Relevance in drug development and background

Of the thousands of novel molecules developed by drug discovery projects that bind to their therapeutic target, typically a few (1 out of 5000) become commercialized drugs⁸. The reason of such a high failure rate is the presence of many physical and biochemical barriers between drug molecules and their targets: metabolic enzymes, cell membrane, efflux transporters (*e.g.* P-glycoprotein, Pgp), unspecific binders, toxicity, the possible chemical instability and insolubility. All of these elements challenge the applications of a molecular species in a living organism⁹.

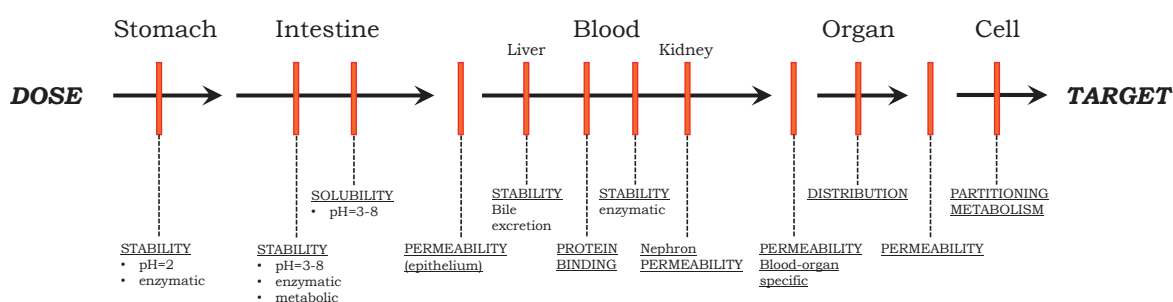


Figure 1:1 Schematic representation of *in vivo* barriers to drug delivery to the target. Adapted from Kerns *et al.*¹⁰.

The effect of some of these barriers is predictable to some extent and can be controlled or even circumvented at the drug-design stage by structural modifications. In this context, the "Lipinski's rule of 5"¹¹ is a useful collection of rules of thumb that identify five chemical properties that a compound has to fulfill in order to have good cell permeability. The rules state that good absorption or permeation of a molecule are more likely when:

- ✓ It has less than 5 H-bond donors (sum of all OHs and NHs)
- ✓ Its molecular weight is below 500
- ✓ Its logP is below 5 (or MlogP is above 4.15)
- ✓ It has less than 10 H-bonds acceptors (sum of all Os and Ns)
- ✓ Substrates of biological transporters are exception to the rule

The rules have been established on the basis of empirical data and computational predictions by Dr. Christopher A. Lipinski of Pfizer in 1997, and have since then a high impact on the drug development strategies and on the evaluation of drug candidates in pharmaceutical industries.

Solubility and permeability of the compounds are so crucial that the U.S. Food and Drug Administration (FDA) created an ad hoc Biopharmaceutic Classification System (BCS), useful for defining criteria of similarity between approved and not-yet-approved molecules, with the aim of accelerating the review process and biowaivers attribution¹². The BCS divides the drugs into four classes based on their parameters of solubility and permeability both *in vitro* and in humans; the class boundaries are quantitatively defined and the measurement methods are specified. Class I compounds are those showing high permeability and high solubility; these are the only compounds eligible for biowaivers. Class IV instead gathers the poorly soluble and poorly permeable compounds; these are high-risk compounds that likely will not reach the market.

It is important to underline that drug profiling is not an exact science: even though guidelines are available for the prediction and the improvement of Absorption (which directly correlates with solubility and permeability), Distribution, Metabolism, Excretion and Toxicity (ADMET) are very complex features that are subject to a high degree of uncertainty. Nevertheless, the pharmacokinetic (PK) profiling of drug candidates is fundamental in drug discovery programs because it alerts developers about potential issues and it allows early selection of lead compounds, therefore shortening the development process and increasing the chances of success¹³.

1.1.2 Methods to assess drug permeability *in vitro*

Although Lipinski's rules speak in favour of the presence of recurrent correlations between chemical structures and molecules' degree of permeability, they still remain non-exhaustive¹⁴ qualitative observations. It is not trivial to derive *in vivo* quantitative data about molecules' permeability due to the complexity and the costs of studies in humans, too high for early drug discovery. As an alternative, several high-throughput scalable methods have been developed for measurements of *in vitro* permeability. The methods can be divided in two main classes, the non-cell-based and the cell-based, which differ in costs and degree of similarity to the tissues in living organisms.

The non-cell-based techniques to assess permeability are essentially phospholipids-based techniques. Among the most important there are:

- i. Phospholipid Vescicle-based Permeability Assay (PVPA): the model consists in layers of small and large liposomes prepared by hydration in phosphate buffer and deposited on a filter support by centrifugation¹⁵. The filter undergoes several freeze-thaw cycles which originate a compact barrier of layers of liposomes of different dimensions that well mimic the heterogeneity of the intestinal epithelia. The filter is then loaded with a solution of the drug of interest (constituting the donor chamber) and placed on top of an acceptor chamber containing buffer. At different time points the

filter with the drug solution on the top are moved to a new acceptor chamber containing fresh buffer. At the end of the experiment the amount of drug found in the different acceptor chambers is calculated and plotted over incubation time.

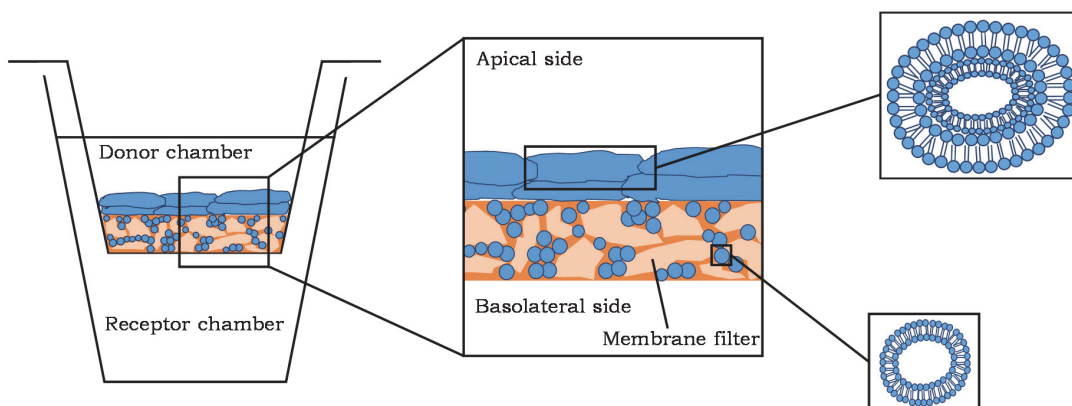


Figure 1:2 Schematic illustration of the PVPA barrier structure, where small and large liposomes are deposited on the membrane filter. Adapted from Gomes *et al.*¹⁶.

- ii. **Immobilized Artificial Membrane-HPLC (IAM-HPCL)**: the technique is based on the use of a chromatographic column in which the stationary phase is made of silica covalently functionalized with phospholipids, like phosphatidylcholine (PC) which is the most commonly used. The affinity of the compound of interest for the lipid monolayer correlates to its interaction with the cell membrane, and ultimately with its cellular permeability^{17, 18}. Known internal standards are often used as reference for the calibration of the retention time. One of the major assets of the method consist in the fact that chromatographic systems are extremely common pieces of equipment in research laboratories and allow rapid and automated measurements.
- iii. **Parallel Artificial Membrane Permeability Assay (PAMPA)**: the method was developed by Manfred Kansy from Hoffmann-La Roche in 1998¹⁹ and became quickly popular in both industrial and academic research laboratories. Similarly to the PVPA assay, acceptor and donor chambers are separated by a porous synthetic filter soaked with a solution of phospholipids in organic solvent (*e.g.* lecithin or PC in dodecane). Typically these separate reservoirs are created in 96-well plates, perfectly suited for High Throughput Screening (HTS). Differently from the PVPA assay, the lipids are not treated to form liposomes and in PAMPA the donor solution containing the compound of interest is located below the membrane, which carries on top the acceptor aqueous buffer.

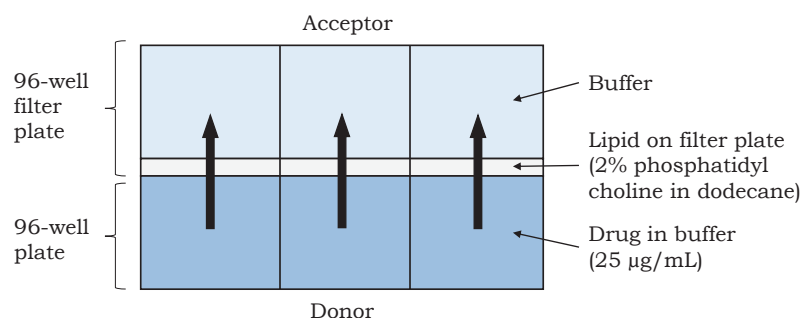


Figure 1:3 Schematic representation of the PAMPA experiment. Adapted from Kerns *et al.*²⁰

After the desired period of incubation, the amount of compound present in both the donor and acceptor chamber is measured by LC/MS or UV absorbance; the permeability through the membrane is then calculated with respect to the original concentration of the donor solution. Nowadays several variants of the method exist, where the lipid composition of the membrane is varied to improve the biomimetics of the model, to better simulate the membrane of specific tissues²¹ (e.g. the blood-brain barrier, BBB) or to better fit the acid-base properties and lipophilicity of the drugs tested²².

The non-cell-based methods offer the advantages of being simple, fast and cheap and therefore suitable for the screening of large families of molecules, essential in early drug discovery. They also provide versatility: the lipid composition employed in all these assays can be modified at choice according to the compound's properties²³ and to the specificities of the tissue to mimic.

Nevertheless, non-cell-based assays are valuable only for mimicking one single cellular permeation mechanism: passive diffusion. Other cellular access routes require either the consumption of energy (active transport) or the passage through paracellular junctions driven by gradients of concentration (passive transport, like diffusion). Active transport is carried out by endocytic proteins, membrane transport proteins and efflux pumps which are expressed and displayed on the surface of cells but cannot be integrated into artificial lipid-based membranes.

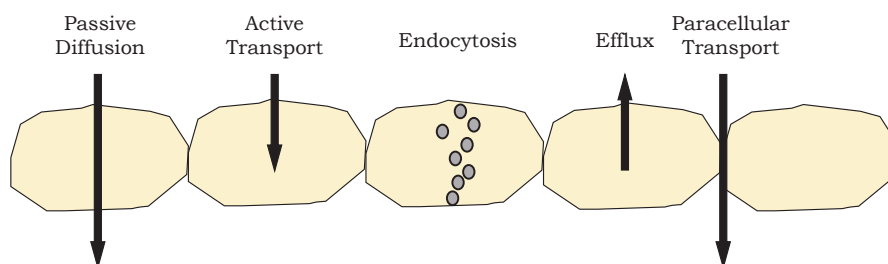


Figure 1:4 Schematic representation of the major permeability mechanisms. Adapted from Kerns *et al.*²⁴.

Passive permeation has been historically considered as the most common route of drug absorption²⁵. However, this belief was shown to be an oversimplification: the progress made in the field helped the discovery of membrane transport proteins for many active drugs. The scenario in a living organism is the one of highly diversified tissues, where expression levels of transporters, transporter's nature and drug concentrations at different biological membranes can vary²⁶. In light of this complexity and despite their costs and slow handling, cell-based permeability assays are better simulators, crucial in the early development of therapeutics. Two most commonly used are described below:

- i. Madin Darby Canine Kidney (MDCK) cells: the use of this non-human cell line became a helpful alternative to the more popular Caco-2 especially because of its faster growing rate and its robustness, which consequently allow a reduction of costs and effort for permeability testing. The formation of MDCK functional monolayers takes 3-4 days of culture, and during this time the cells differentiate into columnar epithelium, just like Caco-2²⁷ (*vide infra*). The cells are plated in devices that are very similar to those employed in PVPA assays: they settle and grow on a porous filter support which separates donor and acceptor chamber. When the culture reaches

confluency and forms a tight layer, the test compound is added on its upper surface (apical side), where the cells develop microvilli, microscopic rod-shaped cell membrane protrusions that increase the cell surface; the acceptor chamber is filled with just buffer, instead. At different time points aliquots from the two chambers are taken and the compound from each is quantified and plotted against incubation time.

- ii. Caco-2 cells: is the gold standard cell-line for *in vitro* permeability assay. Caco-2 cells derive from a human colon carcinoma, have appreciable morphological similarity to gastro-intestinal epithelial cells and, in contrast with MDCK cells, express a variety of cell membrane carrier proteins on their apical surface, therefore allowing the evaluation of the full spectrum of mechanisms of permeability. Caco-2 cells are plated and treated in the same way as MDCK cells, with the difference that they require 3 weeks of culture to express their maximum amount of transporters and therefore to get ready to use²⁸.

Also the test conditions of cell-based systems are prone to some variations: the pH of the buffers in donor and acceptor solutions can be modified to better simulate specific biological environments, buffer stirring systems can be employed to avoid undesired dishomogeneities and surfactants or organic solvents can be added to enhance drug solubility²⁵. The comparison of results from multiple assays enriches the characterization of the drug of interest, allowing to discern in particular which permeability mechanism is predominant case by case.

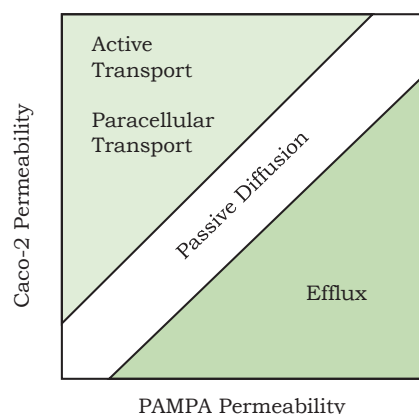


Figure 1:5 The comparison between Caco-2 and PAMPA assays provides insight on the permeability mechanisms of a given molecule. Adapted from Kerns *et al.*²⁰.

In fact, the stronger the correlation between results from non-cell-based and cell-based assays, the more dominant is passive diffusion. The more divergences are pronounced, the more active transport mechanisms become influential.

1.1.3 Methods to achieve the cellular delivery of small molecules

The intracellular access has been subject to extensive interdisciplinary studies in both academic research and pharmaceutical industries. If in academic research the primary aim is to gain a better understanding of cell biology by manipulating and observing with relatively small scale *in vitro* experiments, in pharmaceutical companies the aim is to change the cell biology of entire tissues in a living organism. Clearly, the approaches that

have been developed to achieve cellular delivery in the two fields are very different in terms of invasiveness and scale applicability.

In academic research, several physical and mechanical methods that involve the temporary disruption of the plasma membrane have been developed. Among them the most important are:

- i. Microinjection: is performed by punching the cell membrane of single cells with customized micropipettes, whose movement is controlled with a microscope. The technique has been employed to deliver a large variety of molecular entities: exogenous proteins, DNA, siRNA, peptides, drugs and nanoparticles²⁹. It is a laborious technique that requires a precision and care to target the cell of interest and piercing it without provoking cell perturbation.
- ii. Electroporation: is based on the application of high-intensity electrical impulses to the cell membrane. The impulses provoke a temporary strong polarization of the intracellular environment that induces in its turn the formation on the plasma membrane of pores ³⁰, by which macromolecules can penetrate the cytoplasm. Duration and intensity of the electric pulse determine the size of pores formed and therefore of the macromolecules that can penetrate the cell.
- iii. Sonication: relies on the use of ultrasounds, which induce strong vibrations of gas-containing microbubbles (called ultrasound contrast agents, UCAs) in proximity of cell membranes. These vibrations promote the temporary deformation and opening of the membrane at multiple sites, allowing the influx of molecules³¹.
- iv. Particle bombardment: developed in 1987 for DNA transfer in plants³², this technique was soon adapted to the transfection of mammalian cells and tissues, and this is still nowadays the main application of the technique. Plasmid DNA is coated on the surface of tungsten or gold particles that are successively accelerated by the application of either a strong electric discharge or of a controlled gas pulse, typically helium. The particles in these conditions act as bullets and can penetrate the plasma membrane by collision, delivering the genetic material. The technique has been successfully used also for the introduction of dyes³³, antigens³⁴ and nanosensors³⁵ into cells.
- v. Cationic polymers (e.g. polyethylenimine, PEI) and liposomes: under the effect of hydrophilic/hydrophobic and coulombic interactions, cationic polymers and cationic lipids form respectively aggregates and vesicles containing various molecules of interest. The positively charged external surface of these objects interacts with plasma membrane lipids and receptors, triggering their internalization mainly by endocytosis³⁶. Currently they represent the most common non-viral gene delivery method, but they were also shown effective in the delivery of other molecular entities, like nanoparticles³⁷.

When instead of DNA, dyes and particles the object that has to be introduced into cells is a therapeutic molecule and the scale of the target system switches from a cell/tissue culture to humans, factors like toxicity, scalability, and localized delivery become crucial and none of the techniques listed above is suitable. Here is a non-exhaustive list of methods that are more compatible with therapeutic applications and that are currently protagonists of clinical trials:

- i. Transferrin conjugation: transferrin (Tf) is an 80 kDa protein that works as iron transporter by chelating iron in the extracellular environment, binding to the transferrin receptors (TfR1, TfR2) on the cell membrane and getting internalized by endocytosis. The uptake of the complex Tf-TfR can be exploited to deliver different cargos in the cell: if chemically conjugated to Tf, anti-TfR antibody or their fragments, toxins, DNA, nanoparticles and, more importantly, chemotherapeutic drugs³⁸ are also internalized. Additionally, cancer cells have been proven to extensively overexpress Tf receptors, and this makes the drug delivery even more tumor-specific, lowers the toxicity and increases the therapeutic efficacy.
- ii. Toxins conjugation: toxins are peptides and proteins that have evolved in organisms as defensive systems to exert a detrimental effect on external biological targets. In the same manner as transferrin, toxins bind cell membrane receptors, are internalized by endocytosis and can therefore be used as carriers to achieve localized delivery of therapeutic molecules to diseased tissues³⁹. In order to limit the side effects induced by the administration of toxins, mutations or subunits selection can be applied, provided that they do not affect the interaction to the target membrane receptors.
- iii. Cell Penetrating Peptides (CPPs) and Antimicrobial Peptides (AMPs): are two families of short peptides of mainly cationic and hydrophobic residues (up to 30) known for their intrinsic ability to cross the cell membrane and eventually to carry a variety of different cargo objects together with them⁴⁰. CPPs and AMPs share many characteristics, but the latter are in particular studied for their antibiotic potential⁴¹. The discovery of CPPs dates back to about 30 years ago, when a fragment of the trans-activator (TAT) protein of the HIV-1 virus was recognized to be responsible for its cellular uptake. Since then hundreds of various peptide sequences of either natural or synthetic origin or a combination of both (chimaeric peptides) have been discovered. Extensive studies have been run to reveal their mechanism of cell entry and to compile a list of peptides in order of internalization potency and endosomal escape ability.

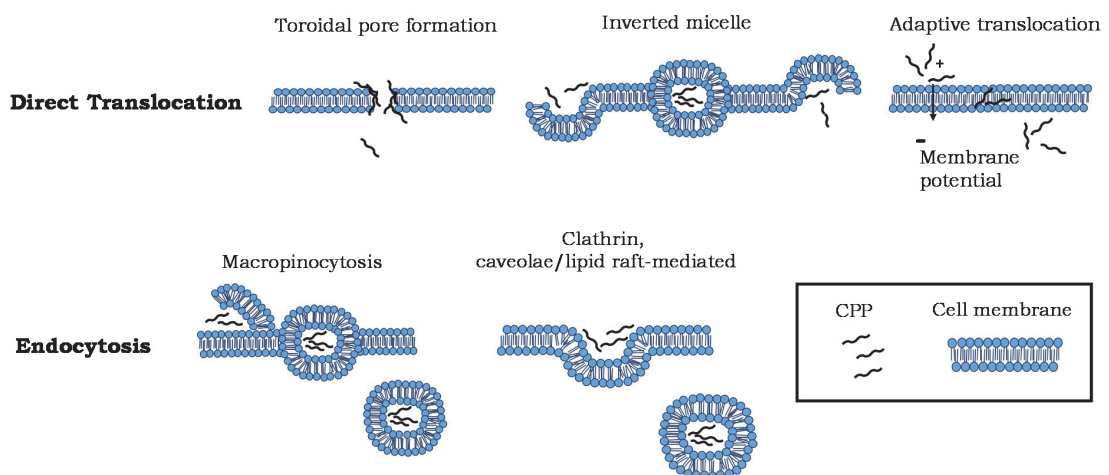


Figure 1:6 Schematic representation of the possible mechanisms of cellular entry of cell penetrating peptides. Adapted from Ramsey *et al.*⁴⁰.

Comprehensively several mechanisms of entry can occur at the same time: they depend on the type of peptide, on its extracellular concentration, on the cell type tested and on the type of label/cargo they may carry along⁴². For these reasons cell entry routes result unpredictable, and require case by case investigations.

- iv. Structure modification: is the gold standard to improve the permeability of compounds, it is the strategy that pharmaceutical companies explore since the beginning of drug development programs. The chemical structure of the molecule is modified in such a way that its cellular transport is increased with the minimum detriment to its function on the biological target. If this delicate task is achievable, then the compound can be employed without any need of derivatization, conjugation to carriers, special devices and additives, and this results in simplified ADME profiling procedures and reduced production costs. The identification of Structure-Property Relationships (SPRs) provides medicinal chemists with guidelines for adjusting the permeability of drug candidates by varying their chemical structure. Examples of modifications identified in this way are²⁴:
 - ✓ replacement of ionizable, polar and H-donor/acceptor groups with isoelectronic/isosteric atoms/functional groups;
 - ✓ reduction of size;
 - ✓ addition of apolar side-chains;
 - ✓ design of prodrugs (provisional inactive drug with improved permeability that gets metabolized *in vivo* to release the active moiety).

1.2 FRET-based biosensors

Cell biology still hides many secrets to the scientific community: the elucidation of cause/effect relationships in enzymatic cascades or metabolic events, the deciphering of physiological processes dynamics with spatial and temporal resolution are very topical needs in the field. In this context, biosensors, namely tools for the detection of cofactors or metabolites and for the sensing of protein-protein interactions, are essential. In particular biosensors based on the phenomenon of Fluorescence Resonance Energy Transfer (FRET) offer the advantage of being minimally invasive, genetically encodable in specific sub-cellular compartments and detectable with ordinary instrumentation.

Fluorescence Resonance Energy Transfer (FRET) is a photophysical phenomenon which consists in the transfer of energy from a radiatively excited donor fluorophore to a second fluorophore that acts as acceptor. Some conditions have necessarily to be satisfied for FRET to occur:

- ✓ The emission spectra of the donor fluorophore has to overlap with the excitation spectra of the acceptor: the wider the overlap, the higher the FRET yield;
- ✓ Donor and acceptor fluorophores have to be in spatial proximity (approx. up to 10 nm): the closer the fluorophores, the higher the FRET yield;
- ✓ The dipole moment of donor and acceptor fluorophore have to be properly oriented relatively to each other: the closer the parallelism, the higher the FRET yield.

The efficiency of the energy transfer is expressed by the following equation:

$$E = \frac{R_0^6}{R^6 + R_0^6}$$

where R represents the distance between the donor and acceptor fluorophores and R_0 , also called Föster radius, is a factor that characterizes each FRET couple in a defined environment: it depends on the spectral overlap between donor emission and acceptor excitation, on the quantum yield of the donor, on the refractive index of the medium and finally on the orientation of the transition dipoles of the fluorophores.

FRET-based biosensors are very often composed of fluorescent protein (FP) pairs, which allow to bypass labeling steps and which can be fused ideally to any sensing motif of interest. Independently from its nature (small molecule or protein), the object to detect has to trigger a relative movement of the two fluorescent proteins upon binding to the sensing motif: the relative movement in fact translates into a measurable reduction or increase of FRET efficiency. In the past decades various FRET-based biosensors that rely on different molecular mechanisms have been designed⁴³. In the next section we will present the sensors developed in our research group that are based on intramolecular conformational change.

1.2.1 Semisynthetic FRET-based sensors, previous work

In the recent past the Johnsson research group has developed a new category of biosensors, the so called SNIFITs, acronym for SNAP-tag based Indicator proteins with a Fluorescent Intramolecular Tether⁴⁴. SNIFITs are semisynthetic biosensors because they are based on both a genetically encodable protein moiety and a chemically synthesized moiety.

The protein moiety of the SNIFITs is a fusion of a binding protein (BP) for the analyte of interest, a FRET-donor and a self-labeling protein tag, like SNAP-tag^{45, 46}. The FRET-donor can be either a fluorescent protein or a second self-labeling protein tag orthogonal to SNAP-tag, like CLIP-tag⁴⁷ that can be labeled with a fluorophore. SNAP and CLIP-tag derive from the human DNA repair protein O⁶-alkylguanine-DNA alkyltransferase (hAGT), a protein that can covalently bind to O⁶-benzylguanine derivatives with one of its cysteine residues. The two tags have been evolved to be specific to O⁶-benzylguanine (BG) or to benzylchloropyrimidine (CP) in the case of SNAP-tag, and to O²-benzylcytosine (BC) derivatives in the case of CLIP-tag, and this allows the simultaneous labeling of the two proteins with different substrates^{48, 49}.

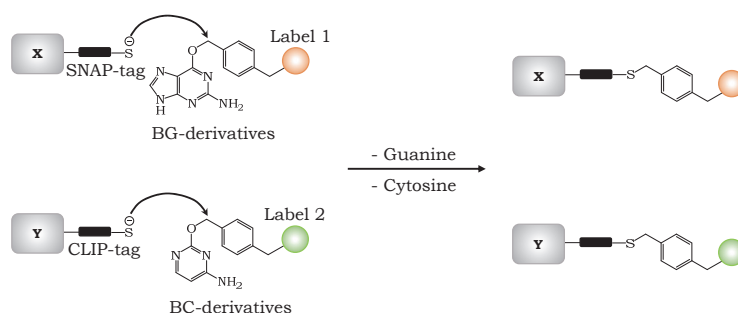


Figure 1:7 Schematic representation of the specific and orthogonal labelling reactions of SNAP and CLIP fusion proteins respectively with BG and BC derivatives. Adapted from Gautier *et al.*⁴⁷.

The chemically synthesized moiety of the SNIFITs consists in a BG-derivative containing an acceptor fluorophore and a second ligand for BP. After labeling of SNAP-tag with the BG-

substrate, this second ligand works as an internal binder that competes with the analyte of interest for the binding to the BP.

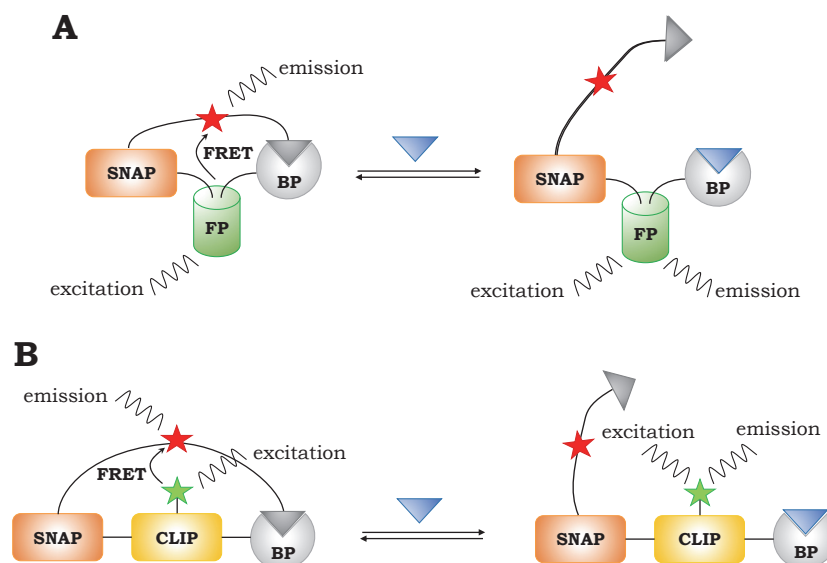


Figure 1:8 Design and working principle of the SNIFITs based on the FRET between a fluorescent protein (FP) and a synthetic fluorophore introduced by SNAP-labelling (red star) (A) or on the FRET between two synthetic fluorophores introduced by orthogonal labelling of SNAP and CLIP-tag (red and green star respectively) (B). Adapted from Brun *et al.*⁴⁴

In absence of analyte (blue triangle in Figure 1:8) the sensor is in the closed conformation, where BP is bound to the internal binder, the donor fluorophore is in proximity of the acceptor fluorophore and the FRET efficiency therefore is high. When present, the analyte displaces the internal binder shifting the sensor to the open conformation, where the acceptor fluorophore can freely move around the bond to SNAP and the FRET efficiency is low. The quantification of the analyte in an unknown solution is enabled by the correlation between analyte concentration and ratio of the donor over acceptor fluorescence (FRET ratio).

On the base of this design the following SNIFITs have been developed in the past:

- ✓ a proof of concept sensor⁴⁴ and a cell surface sensor⁵⁰ based on the protein HCAII (very well known and far and wide characterized enzyme) for HCA-inhibitors (a variety of them are commercially available);
- ✓ a sensor for γ -aminobutyric acid (GABA) based on the GABA_B receptor⁵¹;
- ✓ a sensor for glutamate based on the ionotropic glutamate receptor 5 (iGluR5)⁵²;
- ✓ a sensor for acetylcholine based on acetylcholinesterase⁵³;
- ✓ a sensor for methotrexate based on *E. Coli* dihydrofolate reductase (eDHFR)⁵⁴.

SNIFITs offer some assets in comparison to other protein-based biosensors. First of all, the working mechanism is independent from the fact that, upon interaction with the analyte, the BP undergoes a significant conformational change: in fact the latter is often too small and this limits the dynamic range of the biosensor. Moreover, thanks to its modularity, the analyte concentration's range of response of a SNIFIT can be tuned simply by choosing appropriate internal binders, showing suitable affinity for the BP. Lastly, SNIFITs provide ratiometric responses, which are independent from the sensor concentration and therefore

advantageous for quantitative applications⁵⁵ *in vitro* but more importantly *in cellulo*, where the sensor concentration cannot be easily controlled.

Chapter 2 Aim of the project

The rationalization of the factors that regulate the access to the intracellular compartment is an objective pursued by many researchers in different fields. In the world of biomedical research the determination of absorption and clearance rates of drug candidates in mammalian cells is a key step in the early understanding of their pharmacokinetic properties. Similarly, in academic research the development of cell penetrating probes is crucial for the investigation and the manipulation of cellular processes.

The aim of this thesis is to provide a versatile and minimally invasive strategy to answer this need. The approach entails the use of genetically encodable FRET-based protein probes for *in cellulo* time-resolved molecular sensing. The correlation between the probes' responses and the cellular uptake/clearance of the compounds tested enables the identification of the determiners in molecular permeability.

First, a proof of principle intracellular sensor based on the Human Carbonic Anhydrase II (HCAII) as binding protein was developed. This sensor was used as model to validate the protein geometry and the experimental setup and to test the feasibility of the approach.

Second, driven by the aim of diversifying the applications of our strategy, we engineered an entirely genetically encoded biosensor for inhibitors of a protein-protein interaction (PPI) important in oncology, the one between the tumor suppressor p53 and its negative regulator Human Double Minute 2 (HDM2)⁵⁶. Small molecule and peptide inhibitors of the interaction p53-HDM2 could be characterized and evaluated with respect to their potential to penetrate the cell membrane.

As a long term perspective, the work presented in this thesis could be adapted to the detection of other families of therapeutically relevant molecules and peptides, enabling their profiling and the rational-design of improved variants.

Chapter 3 HCA-based sensor for sulfonamides

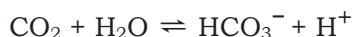
As briefly mentioned in Chapter 2, the starting point for the development of sensors for the assessment of the permeability of molecules was the conception of a sensor based on the protein HCAII, whose most important class of inhibitors are sulfonamides. The main reasons of the choice are as follows:

- ✓ a Snifit based on HCAII was already engineered and characterized in the Johnsson group and this provided a solid base of knowledge and a useful reference for comparison⁴⁴;
- ✓ HCAs have served as model proteins for studies in biophysics and medicinal chemistry and therefore their properties and structures have been described in great detail⁵⁷;
- ✓ HCAs are clinically relevant enzymes and their inhibitors are widely used as therapeutics⁵⁸;
- ✓ HCAII, among the 16 isozymes existing in mammals, is one of the most characterized and the most catalytically efficient⁵⁹ (*i.e.* diffusion controlled);
- ✓ HCAII is a very stable cytoplasmic protein, easy to express and to purify in large amounts.

This chapter contains an overview of the basics about the biological role of HCAs and of their inhibitors, a description of the sensor design and its working mechanism and, more importantly, the presentation of the performance of the sensor in the assessment of sulfonamides' permeability.

3.1 Carbonic Anhydrases, an introduction

Carbonic anhydrases (CAs) are enzymes present in both prokaryotic and eukaryotic organisms that contain a metal ion as an essential cofactor (Zn^{2+} in most cases) and catalyze the reversible hydration of CO_2 :



As a consequence of their role as regulators of the interconversion between CO_2 and bicarbonate, CAs are involved in many physiological processes like CO_2 transport from tissues to lungs, pH homeostasis and several biosynthetic cascades (*e.g.* lipogenesis, ureagenesis and gluconeogenesis)⁶⁰.

In mammals, 16 different CA isozymes have been discovered, each with its specific function, tissue and subcellular localization. Their active site is at the bottom of a deep cavity, where a Zn^{2+} ion is coordinated by three histidine residues and a water-derived hydroxide

anion. In the hydrophobic pocket surrounding the metallic centre the enzyme accommodates a CO₂ molecule that undergoes nucleophilic attack by the hydroxide group present in the coordination sphere of Zn²⁺; bicarbonate is formed and it can leave the active site upon displacement by a water molecule, which is transformed to hydroxide by proton transfer and the catalytic cycle can restart.

The mechanism of inhibition of CAs by sulfonamide derivatives (the biggest family of inhibitors and the only ones used in this work) is based on the substitution of the hydroxide in the coordination sphere of Zn²⁺ with the deprotonated nitrogen atom of the sulfonamide group⁶¹. Moreover, the interaction with sulfonamides is further stabilized by the formation of hydrogen bonds with the amino acids present in the vicinity of the active site⁶².

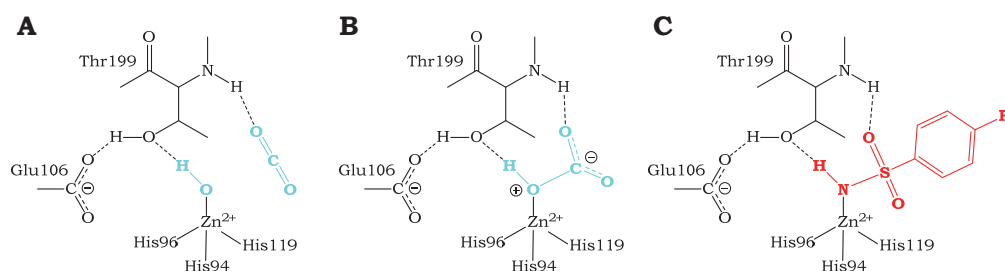


Figure 3:1 Schematic representation of the Zn-bound HCAII active site in presence of CO₂ (A), bicarbonate (B) and an arylsulfonamide inhibitor (C). Adapted from Krishnamurthy, *et al.*⁵⁷

Several sulfonamide-based HCA inhibitors are currently undergoing clinical trials while others are already widespread therapeutics used for the treatment of various diseases⁶³. Some of the most important examples are acetazolamide, methazolamide and ethoxzolamide used mostly as antiglaucoma, antiepileptic drugs and as diuretics; topiramate and zonisamide, known as antiepileptic and antiobesity drugs; indisulam, studied for cancer treatment⁶⁴; hydrochlorothiazide, for the treatment of osteoporosis and hypertension⁶⁵. The diversity of the clinical applications is the proof of the involvement of CAs in numerous critical life processes and motivates the long lasting interest of the scientific community for these enzymes, still at the centre of many open questions.

3.2 Sensor design

Three HCA-based SNIFITs were developed in the Johnsson group before the project described in this thesis was engaged: two were tested for sensing different HCA-inhibitors *in vitro*⁴⁴ and one on the surface of mammalian cells⁵⁰. The three sensors are based on the combination of a fusion protein, either SNAP-CLIP-HCA or SNAP-mCherry-HCA, with a SNAP-labelling substrate containing the fluorophore Cy5 and an aromatic sulfonamide as internal HCA ligand⁴⁴. In the case of the CLIP-based fusion protein, a further labelling with a DY-547-containing CLIP-substrate is necessary for the formation of a FRET pair. Cy5 acts as FRET acceptor while mCherry and DY-547 act as donors. These sensors allowed to reach FRET ratio changes (*i.e.* donor over acceptor fluorescence) up to 80% in *in vitro* measurements and up to 60% with the sensor on the cells surface.

Despite the successful results of the approaches already developed, the need of a biosensor more suitable for intracellular sensing led former members of the group to explore new designs. They engineered a biosensor based on two fluorescent proteins (FPs) as FRET partners and whose functioning relies on the labelling of SNAP-tag with a non-fluorescent

substrate⁶⁶. This strategy offers some important advantages: the elimination of the background fluorescence due to the labelling with synthetic dyes⁶⁷; it increases the chances of the SNAP-substrate to be cellular permeable by reducing its size and hydrophilicity.

3.2.1 The protein moiety

The fusion protein of the sensor for sulfonamides contains SNAP-tag, HCAII as sensory protein and a fluorescent module. The new strategy is based on the integration of the FRET partners in the protein moiety, as FPs. In the specific case, eCFP and YPet were chosen for their suitability for FRET ratiometric experiments⁶⁸: the two proteins show a good spectral overlap, photostability, short maturation times⁶⁹ and an direct hydrophobic interaction which in the closed sensor increases the FRET efficiency and improves the dynamic range of the sensor⁷⁰. In the construct eCFP and YPet are separated by a semi-rigid protein linker constituted by two Gly-Gly-Ser repetitions, that guarantee flexibility^{71, 72}, inserted between two 15-residues-long poly-L-proline chains, that fold into a rigid helical structure^{73, 74}. Such a linker is expected to keep the FPs apart in the open state of the sensor, without hampering the closure in the closed state, leading to an increased FRET ratio dynamic range.

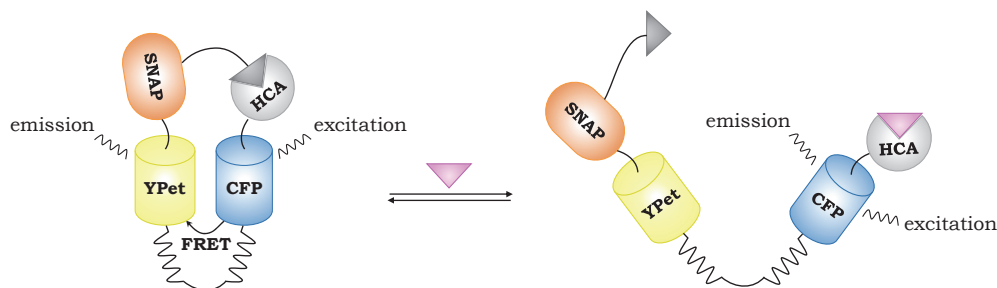


Figure 3:2 Design and working mechanism of the HCA-based sensor.

3.2.2 SNAP-tag labelling molecules

The synthetic molecules necessary to create the reversible connection between SNAP-tag and HCAII are composed of three main parts:

- ✓ a SNAP-tag reactive moiety: as mentioned in Chapter 1.2.1, both BG- and CP-derivatives are substrates for the covalent labeling of SNAP-tag. Since there is no evidence of generalizable differences between BG- and CP-containing compounds in terms of labeling kinetics and cellular permeability, both kinds of derivatives were synthesized;
- ✓ a spacer: spacers of different lengths and polarities, containing polyethylene glycol units (EG₅ or EG₁₁) or alkyl chains (C₆) or their combination (C₆-EG₂) were employed;
- ✓ an HCAII ligand: as HCAII internal binder, a benzenesulfonamide terminal moiety was used. *Meta*- and *para*- derivatives were synthesized: they have different dissociation constants for HCA (respectively high and low nM range⁵⁷), and therefore they offer the possibility to choose the suitable opening/closing sensor kinetics and the range of analyte concentrations in which the sensor is responsive.

Eight SNAP-substrates were synthesized and submitted characterization, in search for the best compromise between the needs of an appropriate length, of good solubility in aqueous

solution, of fast labeling kinetics and of high cellular permeability. Detailed synthetic procedures and spectral data for the compounds are reported in Chapter 6.1.

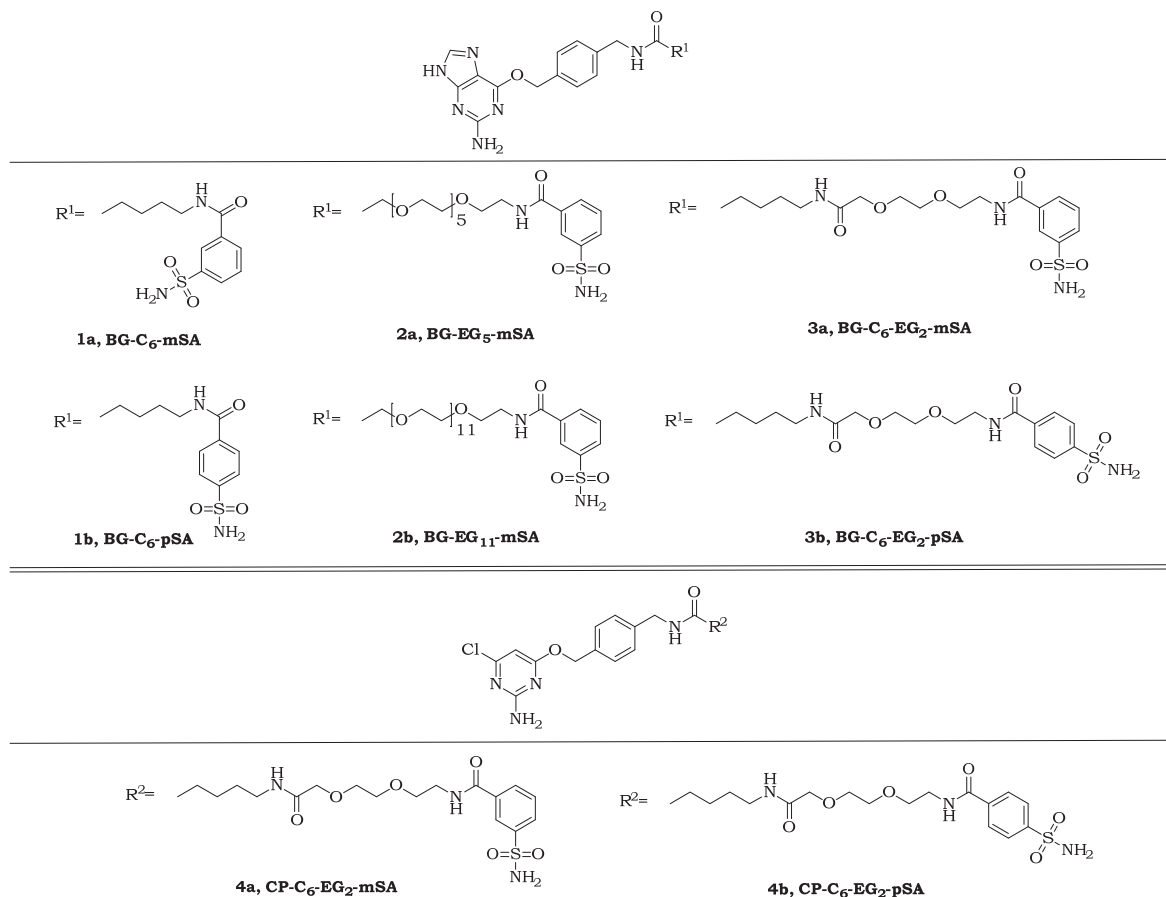


Figure 3:3 Final structure of the substrates for SNAP-tag labelling of the HCA-based sensor.

3.3 Sensing sulfonamides *in vitro*

The starting point of the study and of the optimization of sensor's features *in vitro* was the successful expression and purification of its protein moiety SNAP-YPet-Pro₁₅(GGS)₂Pro₁₅-CFP-HCA from HEK 293 cells by means of its C-terminal His-tag and the N-terminal Strep-tag fusion. 1L of doxycycline-induced HEK 293 cell culture yielded 8.8 mg of pure sensor (cfr. Figure 3:4).

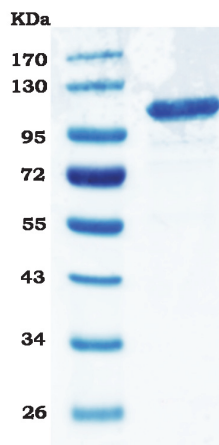


Figure 3:4 SDS-PAGE of the HCA-based sensor protein purified from HEK 293 cells.

Subsequently, a qualitative evaluation of the properties of the synthetic SNAP-substrates presented in Chapter 3.2.2 was performed. In view of the application of the sensor for intracellular measurements, the substrates were first evaluated on the basis of their cellular permeability and ability to react with SNAP-tag *in cellulo*. Then their activity towards SNAP-tag in the sensor construct was assessed. Finally, the best performers were characterized with sulfonamides titrations *in vitro*, which led to select the substrates embodying the best compromise among all these factors.

3.3.1 SNAP-tag labeling *in cellulo* with the substrates

For the assessment of the substrates' ability to penetrate the cells and to react with a SNAP-tag containing fusion protein, a doxycycline-inducible U2OS semi-stable cell line expressing the protein SNAP-CLIP was established and treated as described in Chapter 6.2.7. After overnight incubation with the SNAP-substrate to test, an excess of the fluorescent SNAP-substrate TMR-Star was added and the cells were incubated for further 30 min. The cells were subsequently lysed in presence of a fluorescent CLIP-substrate, BC-SiR, used as internal standard. The cells lysate was analysed by SDS-PAGE (sodium dodecyl sulfate polyacrylamide gel electrophoresis, cfr. Figure 3:5) and fluorescence scan: the intensity in the TMR channel, inversely proportional to the achieved degree of labelling with the SNAP-substrate of interest, was normalized by the intensity in the SiR channel, making the quantification independent from the amount of sensor loaded on the gel. The labelling yield for the tested substrates was calculated by comparison of the corresponding fluorescence band to that of a positive (100% labelling) and of a negative (0% labelling) control, represented respectively by lysates of cells incubated with the non-fluorescent quencher SNAP-Cell Block and with just TMR-Star.

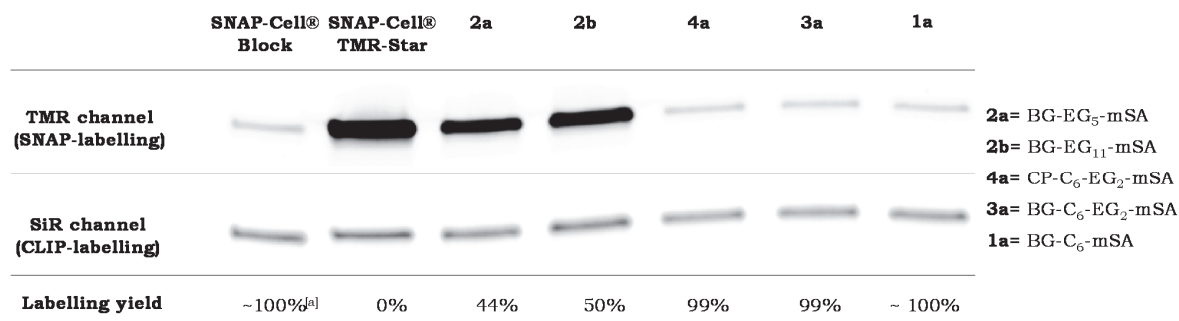


Figure 3:5 Fluorescence scan of an SDS-PAGE of the lysates of SNAP-CLIP cell line incubated with the SNAP-substrates. ^[a]: In the lysate of cells treated with SNAP-Cell Block there is no labelling with TMR-Star. The fluorescence detected in the TMR-channel is due to the bleed-through of the SiR signal; the labelling yield for the other substrates was adjusted taking into consideration this effect.

The described experiment was performed only with mSA-containing substrates. The interpretation of the results relies on the following assumptions:

- ✓ the permeability of a SNAP-substrate is independent on whether the HCA internal binder is *meta*- or *para*-sulfonamide;
- ✓ the efficiency of intracellular SNAP-labelling of the auxiliary construct SNAP-CLIP by a substrate is the same for both its *meta*- and *para*-sulfonamide isomers;

- ✓ the efficiency of intracellular SNAP-labelling is the same for both the auxiliary construct SNAP-CLIP and the protein SNAP-YPet-Pro₁₅(GGG)₂Pro₁₅-CFP-HCA. This is realistic since the crystal structure of SNAP-tag shows⁷⁵ that its C-terminus (CLIP-tag or YPet attachment site) is relatively far from the active site and points to a different direction, which reduces the probability for the protein fused at the C-terminus to affect the labelling efficiency.

The substrates **1a**, **3a**, **4a** (respectively BG-C₆-mSA, BG- and CP-C₆-EG₂-mSA) showed an almost quantitative intracellular labelling, which made them interesting candidates for the continuation of the project. On the contrary, compounds **2a** and **2b** (BG-EG₅-, EG₁₁-mSA) showed only partial labelling, which could be explained either by a poor cellular permeability or by a low reactivity of SNAP-tag towards these substrates. For the purpose of answering this question, they were included among the compounds further investigated.

3.3.2 Sensor-labelling reactivity of the substrates *in vitro*

The progression of the sensor-labelling reaction by each of the substrates was quantified over time: compounds **2a** and **2b** (BG-EG₅-, EG₁₁-mSA) were tested with the aim of clarifying the reason of the low labelling yield measured in cells, whereas for the other substrates the goal was defining the proper labelling incubation time required for the *in vitro* use of the sensor.

The details of the experimental protocol are described in Chapter 6.2.3. At different time points aliquots from a solution of protein SNAP-YPet-Pro₁₅(GGG)₂Pro₁₅-CFP-HCA and substrate of interest were taken and quenched by addition of a large excess of TMR-Star. Similarly to the procedure described in Chapter 3.3.1, the aliquots were analysed by SDS-PAGE and fluorescence imaging. The intensity of the TMR fluorescence was quantified, compared to a negative control (0% labelling) and related to the degree of labeled protein.

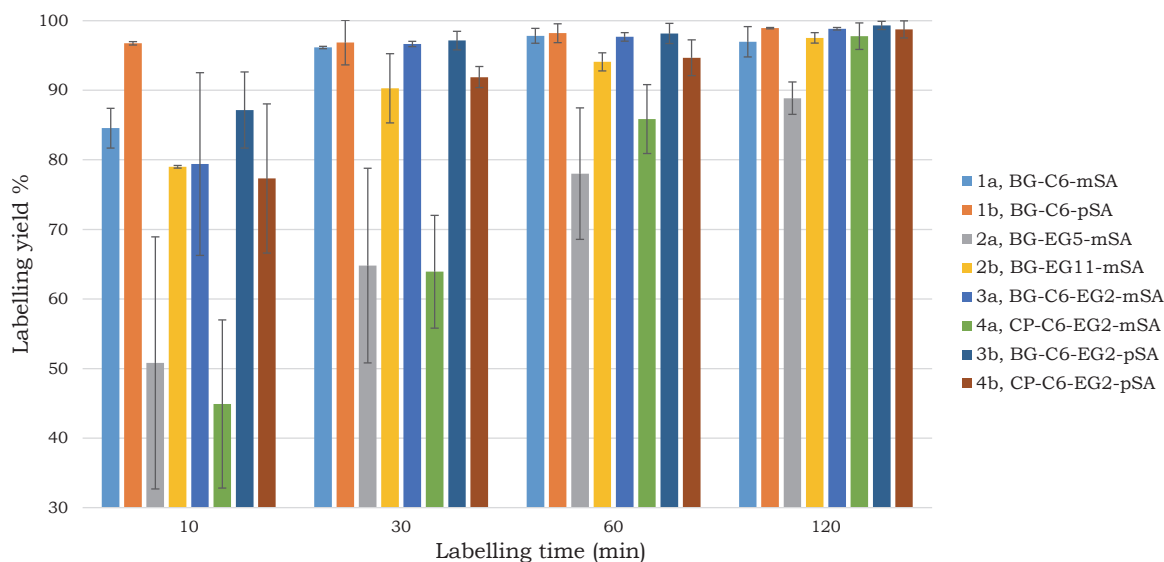


Figure 3:6 Sensor-labelling yields achieved by the substrates over time.

The data summarized in Figure 3:6 shown that after two hours of incubation the labelling of SNAP-tag in the sensor construct was complete for all the substrates except for compound **2a** BG-EG₅-mSA, which after the same time showed about 90% of labelling. Very

interestingly, these results proved that the *in cellulo* low reactivity of compounds **2a** and **2b** (BG-EG₅-, EG₁₁-mSA) was likely due to their poor cellular permeability, rather than to a slow SNAP-labelling rate: in fact, while improving the solubility of the molecules, the ethylene glycol units increased their overall hydrophilicity, reducing their ability to cross the hydrophobic cell membrane. This effect was counterbalanced in compounds **3a**, **3b** (BG-C₆-EG₂-mSA, -pSA), **4a** and **4b** (CP-C₆-EG₂-mSA, -pSA) by a 6-alkyl chain; the shorter EG₂ linker was yet sufficient for assuring good solubility in aqueous solutions.

Two other noteworthy trends could be identified in the results: CP-derivatives were less reactive towards SNAP-tag than their BG-equivalents and mSA-derivatives were less reactive than their pSA-equivalents. The first outcome confirmed what had already been found by former members of the group, who compared the labelling kinetics of CP- and BG-carboxyrhodamine dyes⁷⁶ and found that BG-derivatives show slightly faster labelling kinetics *in vitro*. As for the effect of the internal ligand, it could be rationalised by considering that since pSA-derivatives are stronger HCA-binders than the mSA-derivatives (cfr. Chapter 3.2.2) the local concentration of the former around SNAP-tag in the sensor construct was higher than the local concentration of the latter. The reaction rate is directly proportional to the concentration and this explains the difference in reactivity between isomers.

Compounds **1a**, **1b** (BG-C₆-mSA, -pSA), **3a** and **3b** (BG-C₆-EG₂-mSA, -pSA) proved to be the best performers in terms of both cellular permeability and of SNAP-reactivity; for this reason they were selected for the continuation of the project.

3.3.3 *In vitro* titration of sulfonamide inhibitors

The HCA-sensor labelled with each of the four selected substrates was tested for its ability to sense methazolamide, a commercially available HCA-inhibitor with a reported K_D of 55 nM⁷⁷. As explained in Chapter 1.2.1, in absence of methazolamide the sensor was expected to stay in the closed conformation, where the close proximity of CFP to YPet would lead to high FRET; in presence of methazolamide the intramolecular sulfonamide would be displaced, the sensor would shift to the open conformation progressively with the increase of inhibitor concentration, while the energy transfer would decrease. Following the titration experiment, the ratio between donor emission (CFP) and acceptor emission (YPet) was plotted against the increasing concentrations of methazolamide (cfr. Figure 3:7).

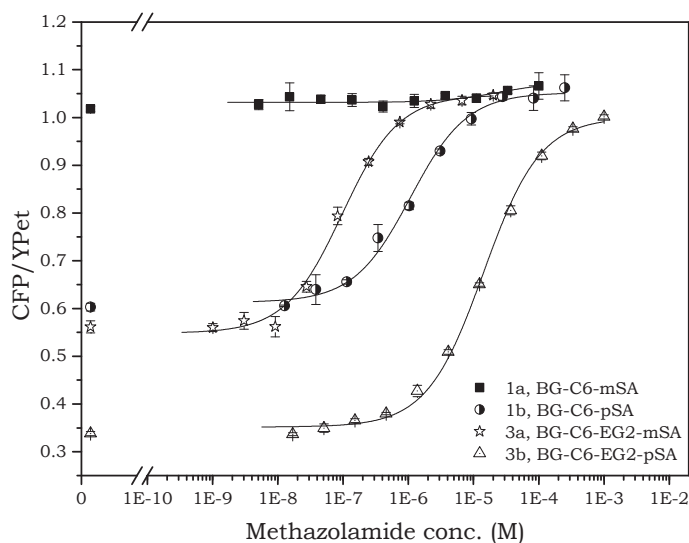


Figure 3:7 Fluorescence titration curve of methazolamide with the HCA-based sensor labelled with different substrates. Each plot shows the ratio donor (CFP) over acceptor (YPet) emission against the concentration of inhibitor.

The conformational shift was clearly recognizable in the case of the sensor labelled with substrate **3b** BG-C₆-EG₂-pSA, whereas it was just partially observed for the sensor labelled with **1b** BG-C₆-pSA and **3a** BG-C₆-EG₂-mSA and not observed at all with **1a** BG-C₆-mSA. In the case of the last three substrates the high values of FRET ratio in absence of methazolamide (last point on the left of the titration curve, cfr. Chapter 6.2.4) indicated that part of the sensor molecules were still in the open conformation. The factors that controlled this effect were likely to be the limited molecular length, the weakness of the mSA moiety as HCA-intramolecular binder or a combination of the two. In particular, the backbone BG-C₆- forces the construct in a constrained geometry and makes the binding constant of the internal ligand thermodynamically achievable just in the case of the sensor labelled with the pSA-containing substrate **1b**, which showed yet a fractional degree of closing in absence of inhibitor. As for substrate **3a**, while the incorporation of EG₂ in the molecule increased its length, the binding of the mSA moiety to HCA seemed to be still only moderately favourable and the closing remained incomplete.

In light of the performances of the different substrates in the test titration with methazolamide, compound **3b** was selected as the most suitable for the successive applications and it was therefore tested for the sensing of a selection of other HCA inhibitors (cfr. structures in Figure 3:8 (C)): ethoxzolamide, acetazolamide, benzenesulfonamide which are commercially available and a molecule made in house containing a pSA moiety, a C₆ linker and a cysteic acid (compound **5**). Compound **5** was synthesized as an example of supposed impermeable sulfonamide, due to the presence of a negative charge on the cysteic acid moiety at physiological pH: we hoped we could demonstrate the suitability of the biosensor to differentiate cell permeable and impermeable molecules.

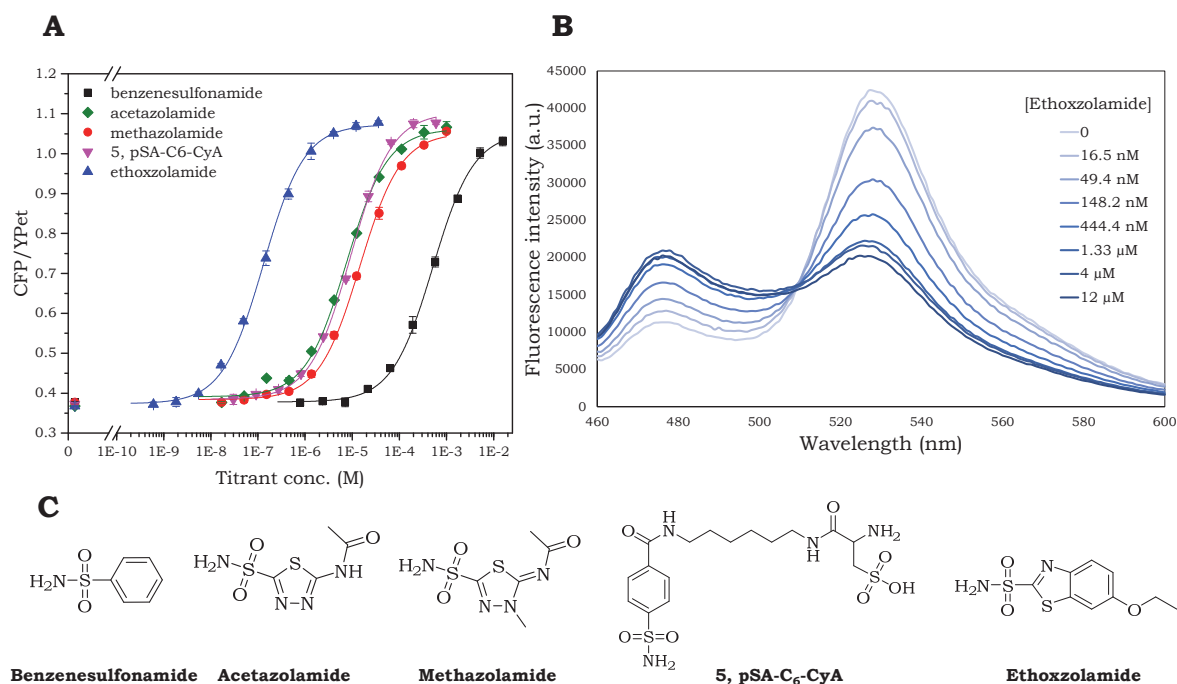


Figure 3:8 (A) Fluorescence titration curve of different inhibitors with the HCA-based sensor labelled with the substrate **3b** BG-C₆-EG₂-pSA. Each plot shows the ratio donor (CFP) over acceptor (YPet) emission against the concentration of inhibitor; the data were fitted to a single-site binding isotherm (cfr. Chapter 6.2.4). (B) Fluorescence emission spectra of the HCA-based sensor in presence of different concentrations of ethoxzolamide. (C) Chemical structures of the HCA inhibitors used.

<i>Inhibitor</i>	C_{50} (μM)	K_D^{comp} (μM)	K_D (nM)	K_D ref. (nM)
<i>Benzenesulfonamide</i>	546 ± 33	229 ± 32	2100 ± 400	200-1500 ⁵⁷
<i>Acetazolamide</i>	7.8 ± 0.1	3.8 ± 0.5	35 ± 6	20 ⁷⁷
<i>Methazolamide</i>	14.5 ± 0.2	6.1 ± 0.3	55 ± 4	55 ⁷⁷
<i>5, pSA-C₆-CyA</i>	9.9 ± 0.8	4.1 ± 0.8	37 ± 10	n.d.
<i>Ethoxzolamide</i>	0.16 ± 0.03	0.06 ± 0.02	0.5 ± 0.3	0.2 ⁷⁸ , 4 ⁷⁷

Table 3:1 *In vitro* C_{50} , K_D^{comp} and K_D of the inhibitors for the HCA-based sensor labelled with **3b**. The reference K_D are for HCAII. The values of K_D for each analyte was calculated using Equation 3:1 (see below).

The sensor labelled with the substrate **3b** BG-C₆-EG₂-pSA exhibited a maximum FRET-ratio change of 189 ± 8 %. For each HCA inhibitor tested the titration curve is reported in Figure 3:9 (A). Different fittings of the intensity ratio data (cfr. Chapter 6.2.4) allowed the calculation of the C_{50} and of the K_D^{comp} , which are the concentrations of inhibitor that lead respectively to 50% of the maximum FRET-ratio change and to 50% of the maximum change in either donor or acceptor channel. Noteworthy, the C_{50} value is not necessarily equal to the K_D^{comp} ⁷⁹, as shown in Figure 3:9 for methazolamide.

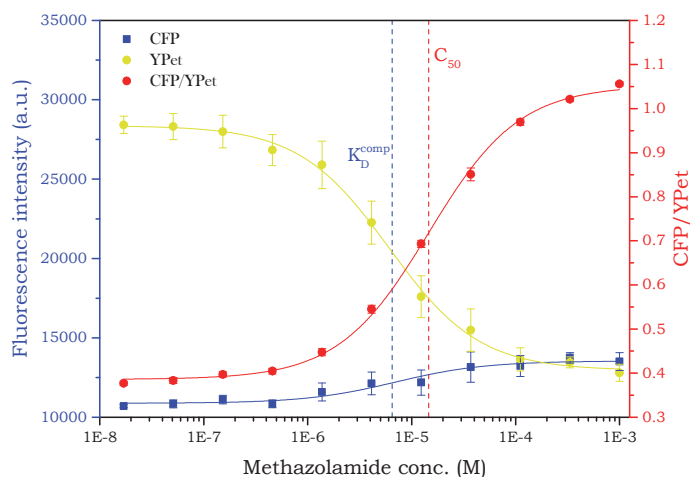


Figure 3:9 Fluorescence emission intensities of CFP and YPet and titration curve of the HCA-based sensor in presence of varying the concentration of methazolamide. The values of C_{50} and K_D^{comp} for methazolamide are indicated by dashed lines.

For a given analyte, the K_D^{comp} value is always higher than the absolute K_D : it results in fact from the combination of the pure affinity of binding protein (BP) for the analyte and the ability of the latter to outcompete the intramolecular ligand. The relation between these quantities is expressed by the following equation:

$$\frac{M_{eff}}{K_D^{int. ligand}} = \frac{K_D^{comp, analyte}}{K_D^{analyte}}$$

in which the effective molarity M_{eff} corresponds to the concentration of the free intramolecular ligand necessary to open half of the sensor molecules if the sensor would be labelled with the very same intramolecular ligand, $K_D^{int. ligand}$ is the dissociation constant of the free intramolecular ligand for the BP, $K_D^{comp, analyte}$ is the dissociation constant of the analyte for the sensor, $K_D^{analyte}$ is the dissociation constant of the analyte for the BP. M_{eff} is a parameter that characterizes a sensor labelled with a given substrate and is equivalent

to the $K_D^{comp,analyte}$ when the analyte is the substrate itself. In the case of the HCA-based sensor labelled with **3b** BG-C₆-EG₂-pSA, it was impossible to measure directly by titration the K_D^{comp} of **3b** because of its limited solubility. Nevertheless, knowing that the K_D of pSA-derivatives similar to **3b** is approximatively 100 nM⁵⁷ and considering the results for one of the HCA inhibitors of Table 3:1 (e.g. methazolamide), the M_{eff} of the sensor could be estimated:

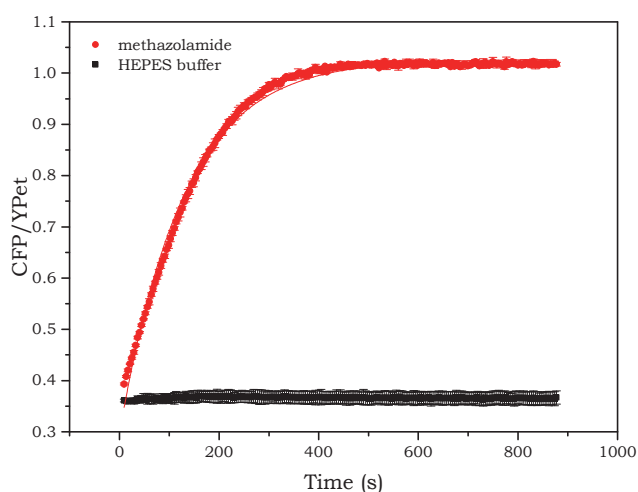
$$M_{eff} = \frac{K_D^{comp,analyte}}{K_D^{analyte}} \times K_D^{int. ligand} = \frac{6100 \text{ nM}}{55 \text{ nM}} \times 100 \text{ nM} = 11 \mu\text{M}$$

Equation 3:1 Calculation of the effective molarity M_{eff} of the HCA-based sensor.

The $K_D^{analyte}$ listed in Table 3:1 were calculated on the basis of this value of M_{eff} and they are in close agreement with those found in literature. Noteworthy, the value of M_{eff} found is lower than those previously published⁴⁴ by former members of the Johnsson group for other sensors. The opening is thermodynamically more favourable for the sensor with the new design with respect to the HCA-based SNIFITs. In these latter constructs just one fluorescent protein⁴⁴ or CLIP-tag⁵⁰ were inserted between SNAP-tag and HCA, whereas our biosensor carries two fluorescent proteins: this likely increases the constraints in the geometry of the new construct.

3.3.4 *In vitro* opening kinetics of the sensor in presence of sulfonamide inhibitors

In the prospect of investigating the uptake rate of HCA inhibitors in living cells, the sensor's opening kinetics were measured at 37°C *in vitro* in the first place. The inhibitors were added to the sensor labelled with compound **3b** at the highest concentrations employed in titration experiments, in order to trigger the fastest opening of the sensor molecules; the FRET-ratio was plotted against time and fitted with a single exponential function.



Inhibitor	$t_{1/2,open}$ (s) <i>in vitro</i>
<i>Benzenesulfonamide</i> (7 mM)	68 ± 1
<i>Acetazolamide</i> (300 μM)	83 ± 1
<i>Methazolamide</i> (300 μM)	75 ± 1
<i>5, pSA-C6-CyA</i> (600 μM)	73 ± 1
<i>Ethoxzolamide</i> (20 μM)	88 ± 1

Table 3:2 *In vitro* opening half-lives at 37°C of the HCA- based sensor labelled with **3b** in presence of saturating concentrations of inhibitors.

Figure 3:10 Example of opening kinetics *in vitro* of the HCA-based sensor labelled with **3b** in presence of methazolamide 300 μM or HEPES buffer.

As previously demonstrated for the sensors developed in the Johnsson group⁵⁰ (based on interaction and displacement of an intramolecular tether, cfr. Chapters 1.2.1 and 3.2), the kinetics of opening is mainly governed by the rate of unbinding (k_{off}) of the intramolecular

ligand, which can eventually be interchanged to tune the sensor's kinetics at will. However, due to the reasons presented in the previous paragraphs, the HCA-based sensor described in this thesis was fully functional only upon labelling with the pSA-containing compound **3b** (cfr. Figure 3:7). In these conditions, the average opening half-life measured with the tested inhibitors was $t_{1/2,open} = 77 \pm 8$ s, which corresponds to a $k_{off} = (9 \pm 1) \cdot 10^{-3} \text{ s}^{-1}$ of the pSA-containing intramolecular ligand. This value was globally slower than the one reported for similar pSA-derivatives⁵⁷ ($k_{off} \sim 30 \cdot 10^{-3} \text{ s}^{-1}$) but very similar to the one previously measured on cells surfaces with the HCA-based SNIFIT also labelled with a pSA-containing substrate⁵⁰ ($k_{off} \sim 10 \cdot 10^{-3} \text{ s}^{-1}$).

3.4 Sensing sulfonamides *in cellulo*

After having elucidated some of its key properties *in vitro*, the ability of the sensor to allow direct, non-invasive intracellular detection of HCA inhibitors was tested. The protein moiety of the sensor was expressed in a doxycycline-inducible U2OS cell line and it was found having a uniform, mainly cytosolic distribution (cfr. Figure 3:11).

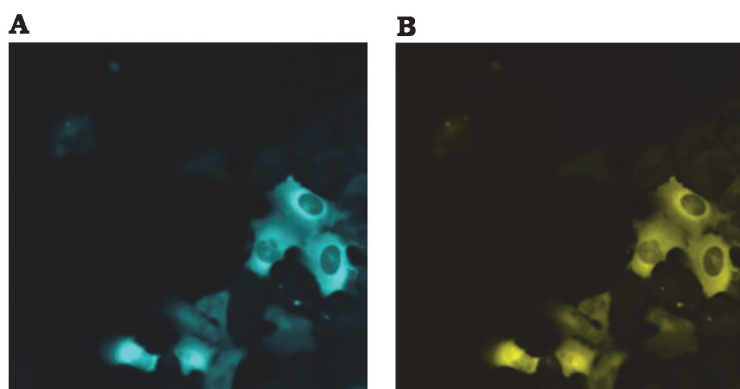


Figure 3:11 Example of microscopy images of the U2OS cell line expressing the HCA-based sensor and labelled with the compound **3b**. After CFP excitation, the CFP emission image (A) and the YPet emission image (B) were registered.

The labelling was performed by over-night incubation with the dye-free substrate **3b**.

3.4.1 *In cellulo* titration of sulfonamide inhibitors

The intracellular concentration-dependent response of the sensor to HCA inhibitors was evaluated by fluorescence microscopy on the labelled cell line in titration experiments.

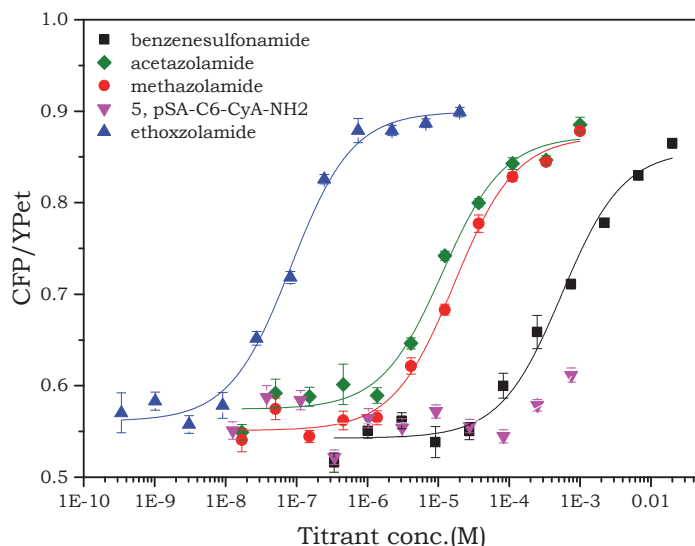


Figure 3:12 *In cellulo* fluorescence titration curve of different inhibitors with the HCA-based sensor labelled with the substrate **3b** BG-C6-EG2-pSA.

<i>Inhibitor</i>	<i>C₅₀ in cellulo</i> (μ M)	<i>C₅₀ in vitro</i> (μ M)
<i>Benzenesulfonamide</i>	$(4 \pm 2) \cdot 10^2$	$(5.5 \pm 0.3) \cdot 10^2$
<i>Acetazolamide</i>	8 ± 4	7.8 ± 0.1
<i>Methazolamide</i>	14 ± 5	14.5 ± 0.2
<i>5, pSA-C6-CyA</i>	n.d.	9.9 ± 0.8
<i>Ethoxzolamide</i>	0.07 ± 0.02	0.16 ± 0.03

Table 3:3 Comparison between *in cellulo* and *in vitro* C_{50} s of the HCA-inhibitors for the sensor labelled with **3b**.

With the only exception of compound **5** pSA-C6-CyA, the C_{50} s of the inhibitors measured *in vitro* and *in cellulo* were very similar (cfr. Table 3:3), which suggested that the sensor retained its properties when expressed in mammalian cells and that the inhibitors entered the cells by passive diffusion. In fact, the presence of active efflux or influx pumps would have altered the titration profile of a compound by shifting its C_{50} respectively to higher or lower concentrations. The case of compound **5** was separate: while *in vitro* it displayed a good affinity for the HCA-sensor (comparable to the one of acetazolamide and methazolamide), it turned out to be totally ineffective *in cellulo*, where it did not trigger any FRET ratio change (cfr. Figure 3:12). Considering that it contains a sulfonic acid moiety which is negatively charged at physiological pH ($pK_a=1.3$)⁸⁰, the molecule is very likely impermeable to the cell membrane. Thus compound **5** represented a good control, since it allowed to demonstrate that differences in molecular permeability of sulfonamides could indeed be detected with the help of the developed biosensor.

The passage from the *in vitro* to the *in cellulo* sensor's use provoked however a loss of FRET-ratio dynamic range of more than 60%, from about 190% to about 70% (cfr. open and close FRET-ratio values in Figure 3:8 and Figure 3:12). This might be due to the fact

that the cellular space is densely occupied by biomacromolecules, like proteins, nucleic acids, sugars and organelles⁸¹; these objects are responsible for a background autofluorescence which can alterate the absolute results of the measurement by reducing the signal-to-noise ratio (SNR)^{82, 83}. Moreover, the macromolecules can interact with the sensor and therefore have an often unpredictable and unclear effect on its response. Despite these limitations, the HCA-based sensor exhibited a dynamic range sufficiently wide to allow reliable measurements of intracellular concentrations of sulfonamides.

3.4.2 *In cellulo* kinetic characterization of the sensor in presence of sulfonamide inhibitors

The evaluation of the *in cellulo* kinetic response of the HCA-based sensor was performed with batch experiments in 96-well plates on the labelled cell line. The cells were imaged over time by fluorescence microscopy following the addition of the analyte of interest; after attainment of equilibrium, the supernatant solution containing the analyte was exchanged with fresh buffer and the microscopy imaging over time was restarted.

Ideally, the application of the biosensor to time-resolved intracellular concentration measurements requires opening and closing rates faster than the rate of the analyte's intracellular concentration change. This condition becomes particularly stringent when the analyte to sense can pass very rapidly through the cell membrane: in this case the opening and closing rates (which depend on the k_{off} respectively of the tether ligand and of the analyte) can represent the bottleneck of the measurement and prevent the recognition of differences in cell entry and exit kinetics between species.

The studies conducted *in vitro* revealed that the fully functional version of the HCA-based sensor (labelled with the pSA-containing substrate **3b**) is characterized by a relatively slow opening rate, determined by the k_{off} of the intramolecular tether. Indeed, the experiments *in cellulo* showed that the opening half-life of the sensor was very similar for all the inhibitors tested with the exception of the sulfonic acid-derivative **5**, which proved to be impermeable (cfr. Figure 3:13 (A)).

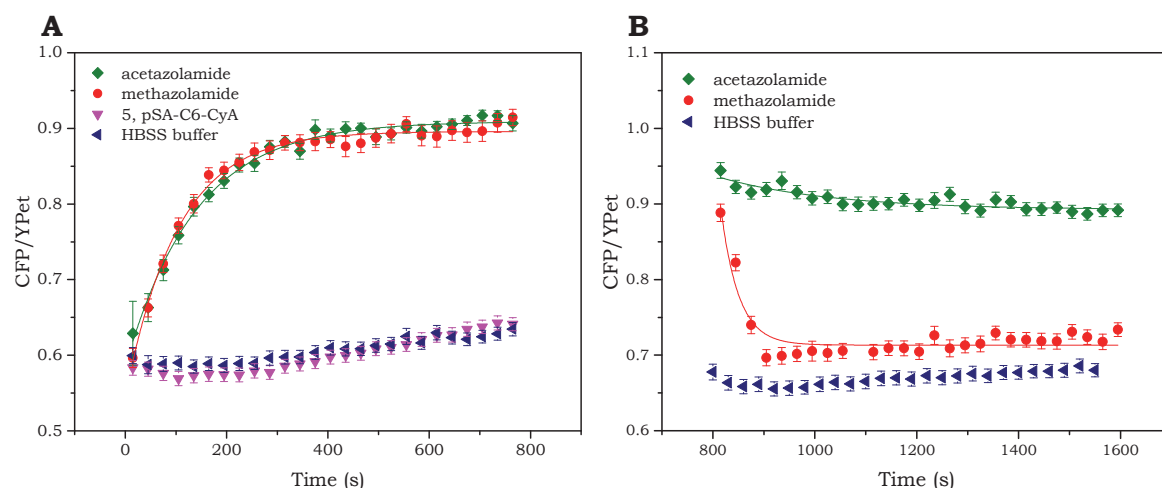


Figure 3:13 (A) Opening kinetics measured by live cell imaging of the intracellular HCA-based sensor labelled with **3b** in presence of acetazolamide 300 μM , methazolamide 300 μM , compound **5** or HBSS buffer. (B) Closing kinetics after removal of the inhibitors and after incubation with fresh HBSS buffer.

Inhibitor	$t_{1/2,open}$ (s) in <i>cellulo</i>	$t_{1/2,open}$ (s) in <i>vitro</i>
<i>Benzenesulfonamide</i> (7 mM)	74 ± 12	68 ± 1
<i>Acetazolamide</i> (300 µM)	113 ± 25	83 ± 1
<i>Methazolamide</i> (300 µM)	88 ± 21	75 ± 1
5, pSA-C6-CyA (600 µM)	n.d.	73 ± 1
<i>Ethoxzolamide</i> (20 µM)	89 ± 21	88 ± 1

Table 3:4 Opening half-lives measured *in cellulo* and *in vitro* of the HCA-based sensor labelled with **3b** in presence of saturating concentrations of inhibitors.

For all the cell permeable inhibitors the opening half-life values *in cellulo* were comparable to the one attained *in vitro*: this proved that benzenesulfonamide, acetazolamide, methazolamide and ethoxzolamide are all characterized by high cellular permeability and that their cell entry rates exceed the biosensor's opening rate, preventing the differentiation of their permeabilities.

The clearance rates of the inhibitors from the cells were also evaluated. The solutions containing the inhibitors were manually removed and fresh HBSS buffer was added to the cells right before the restarting of the time course imaging (dead time of about 30 s). This technique presented two main drawbacks: it only allowed to dilute the inhibitor, instead of removing it completely with continuous buffer exchange; also, the addition of fresh buffer to the cells provoked systematically an artificial upshift of the FRET ratios of about 0.05 units with respect to the plateau attained at the end of the internalization. For these reasons these experiments were accounted just for the qualitative information provided.

For all the inhibitors (but compound **5**) the plateau of FRET ratio achieved after incubation with the HBSS buffer was higher than the FRET ratio value of control cells, treated just with buffer (cfr. Figure 3:13 (B)). Small differences with respect to the control can be justified by the fact that, despite the important dilution, the inhibitors were not completely eliminated from the batch setup and therefore they could still be partially in the cells.

However, the case of acetazolamide was different: the FRET-ratio decrease over time upon incubation with fresh buffer in fact was minimal and it seemed to stabilize at a much higher value than the one of the control, as if the molecule was retained in the cells. Acetazolamide and methazolamide, which have very similar chemical structures, have been found to unbind HCAII with very similar kinetics⁸⁴, which made the difference detected in the washout experiment even more surprising. This outcome could explain the disagreement between the cell entry kinetics of acetazolamide measured with the biosensor and the results of another study⁸⁵, reporting that the permeability of acetazolamide measured with the Caco-2 cells model is poor, more than 10 times lower than the reference compound carbamazepine. In fact, the experiments on the cellular monolayer do not allow to distinguish the two steps of the process of transport through cells, entry and escape; on the contrary, the biosensor revealed that, after a quick penetration, acetazolamide is held in the cell, and for this reason it might not reach the acceptor chamber of the Caco-2 cells reservoir.

Acetazolamide and methazolamide displayed very different clearance profiles with the sensor, although they have very similar polar surface areas (115 and 105 Å², respectively^{86, 87})

and they both seem to enter the cells by passive diffusion⁶⁶. Based on the information available on the DrugBank database reporting that the degree of plasma protein binding is 98% for acetazolamide⁸⁶ against 55% for methazolamide⁸⁷, it was proposed that the reason for the different behavior of the two molecules lied in the different degree of binding to albumin, which represents around 19% of the cytosolic and 60% of the plasma protein content^{88, 89}. However, for this hypothesis to be realistic, the C_{50} of acetazolamide obtained *in vitro* (where the BSA concentration was 0.5 mg/ml) should have been significantly lower than the one obtained *in cellulo* (where the BSA concentration is about 40 mg/ml); since it was not the case, the issue was left without answer.

3.4.3 Conclusions and outlook

The present chapter focuses on the engineering and testing of a novel FRET-based biosensor for inhibitors of the enzyme Human Carbonic Anhydrase II (HCAII). Its design, based on the use of fluorescent proteins as FRET-partners, constitutes an innovation with respect to the previously developed sensory proteins SNIFITs, inasmuch as it does not require labelling with synthetic fluorophores and it is therefore more suitable for intracellular applications.

Initially, a selection of SNAP-tag non-fluorescent substrates was successfully synthesized and evaluated with respect to the ability to penetrate the cell membrane and to convert rapidly the sensor into a functional state. Following the identification of the best-performing substrate, the labelled sensor was used to sense multiple sulfonamides *in vitro*, where it displayed a large FRET-ratio change of about 190%, a high signal-to-noise ratio and a good correlation between the affinities measured and those reported in literature. Then the biosensor was expressed, assembled and tested in living cells, where its suitability for quantifying and comparing real-time absorption and clearance kinetics of various sulfonamides was proved. In particular, it was found that the pSA and sulfonic acid-containing compound **5** was cell impermeable, whereas all the other tested inhibitors required less than 5 minutes to saturate the intracellular bioprobe. Also, the sensor revealed remarkable differences in the washout kinetics of two very similar approved drugs, acetazolamide and methazolamide: they were both taken up by the cells fairly quickly, but while methazolamide could be also rapidly removed from the cytosol, acetazolamide had extremely long clearance times. These findings highlighted the limitations of permeability studies based on the Caco-2 cells model, classifying acetazolamide as poorly permeable and unable to provide detailed information on the two separate processes of cellular absorption and washout.

The described biosensor provides the opportunity to investigate the cell permeabilities of multiple sulfonamide drugs or sulfonamide-derivatives, while comparing their absorption and clearance kinetics in a single experiment on the same living cells of choice. Further work on the project would focus on the search of an HCA-internal ligand with an affinity strong enough to guarantee the achievement of the sensor's close conformation, but able to provide at the same time faster opening kinetics, which would increase the temporal-resolution of the bioprobe. Also, more tests would be performed to elucidate the reasons of the cytosolic retention of acetazolamide, which unfortunately are still unclear. Finally, the approach and the sensor's design presented in this chapter can be potentially adapted to study the permeability of many other classes of molecules, provided that a binding protein for the molecule is known and that a suitable intramolecular ligand can be synthesized.

Chapter 4 Label-free p53-based sensor for inhibitors of the p53-HDM2 interaction

The successful development of an intracellular sensor for HCA inhibitors and its efficient use to assess the permeability of sulfonamides encouraged us to adapt the bioprobe design to sense disruptors of a protein-protein interaction (PPI) highly studied in cancer biology, the one between the transcription factor p53 and its negative regulator HDM2.

This chapter starts with essentials of the biological relevance of PPIs in general, and more precisely of the role and the features of the p53-HDM2 interaction; the distinctive characteristics of their small molecule and peptide inhibitors are also presented. Then, the design of the label-free biosensor and its performance under physiological and non-physiological conditions are described.

4.1 Introduction

4.1.1 Protein-protein interactions as therapeutic targets

The development of high-throughput technologies and decades of research in proteomics, genomics and network biology have revealed the importance of protein-protein interactions in the control of critical cellular processes like gene regulation⁹⁰, signaling cascades, metabolism and control of the cell cycle⁹¹. Because of their implication in key physiological functions, defective PPIs have been linked to a large number of diseases^{92, 93} and represent highly investigated therapeutic targets. The development of PPIs' inhibitors is yet a big challenge⁹⁴: while the ligand binding pockets of enzymes are usually deep and well-framed, the contact surface of protein-protein interfaces is often wide, flat and hydrophobic, which badly matches with drugs bioavailability determinants like solubility and low molecular weight. However, alanine-scanning mutagenesis studies revealed that frequently most of the protein-protein binding energy depends on localized regions of few key residues, called "hot spots"⁹⁵, whose identification facilitates targeted modulators' development and therefore enables PPIs druggability.

PPI inhibitors can be divided into three categories, depending on the degree of complexity of the surface where the hot spots are located⁹⁶:

- i. small, linear epitopes can be targeted by small molecules and short peptides;
- ii. secondary-structural epitopes (which are often groove-shaped) require small molecules and peptides able to organize in 3D-structures, *e.g.* α -helixes, β -sheets or mimics;

- iii. tertiary-structural epitopes are shallow and dynamic and therefore require inhibitors able to undergo or trigger structural rearrangements.

An interesting example from the second category are peptides constrained in an α -helical conformation which seems to be well suited to mimic the topology of a large portion of PPI's interfaces⁹⁷.

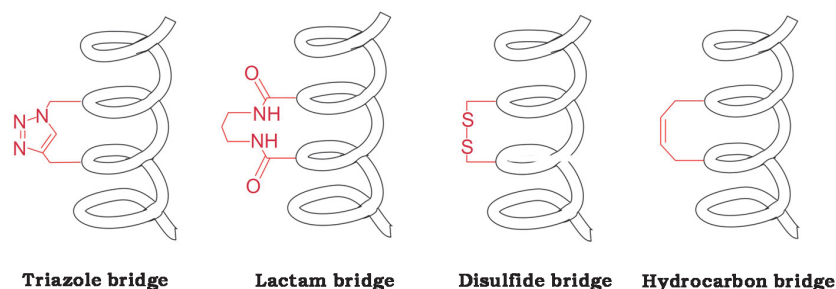


Figure 4:1 Schematic representation of covalent linkages to lock α -helices in peptides. Adapted from Jamieson *et al.*⁹⁸.

The geometrical constraints can be created through a variety of covalent chemical bonds, such as triazole⁹⁹, disulfide¹⁰⁰, lactam¹⁰¹ and hydrocarbon bridges (cfr. Figure 4:1). The peptides locked via this latter kind of connection are called "stapled peptides": they are synthesized¹⁰² by ruthenium-catalysed olefin metathesis between the side chains of residues i and $i+4$ or i and $i+7$, which originate respectively 8- and 11-carbon tethers responsible for the stabilization of helices of one or two turns. Stapled peptides stand out from the variety of therapeutic peptides for some key characteristics¹⁰³:

- ✓ their excellent pharmaceutical stability, due to the fact that the alkyl linkage protects the peptides from proteolysis;
- ✓ their improved affinities with respect to the corresponding native sequences, due to formation of additional hydrophobic interactions between the hydrocarbon staple and the surface of the target protein⁹⁸;
- ✓ their good cellular penetration, promoted both by the increased hydrophobicity of the overall structure and by their interaction with the cell membrane proteins and sugars¹⁰⁴.

The success encountered by this class of peptides in clinical trials¹⁰⁵ encourages researchers to explore their therapeutic potential in many diseases-related PPIs.

4.1.2 p53 and HDM2

p53 is a nuclear transcription factor that controls, among other functions¹⁰⁶, cellular apoptosis and growth arrest in response to DNA damage and to a variety of stress signals¹⁰⁷. Since its activation prevents the propagation of cells containing potentially oncogenic DNA mutations, it is considered to function as a tumor suppressor protein, and loss of function mutations in the p53 gene have been discovered to promote the development of over half of human cancers¹⁰⁸ (cfr. Figure 4:2).

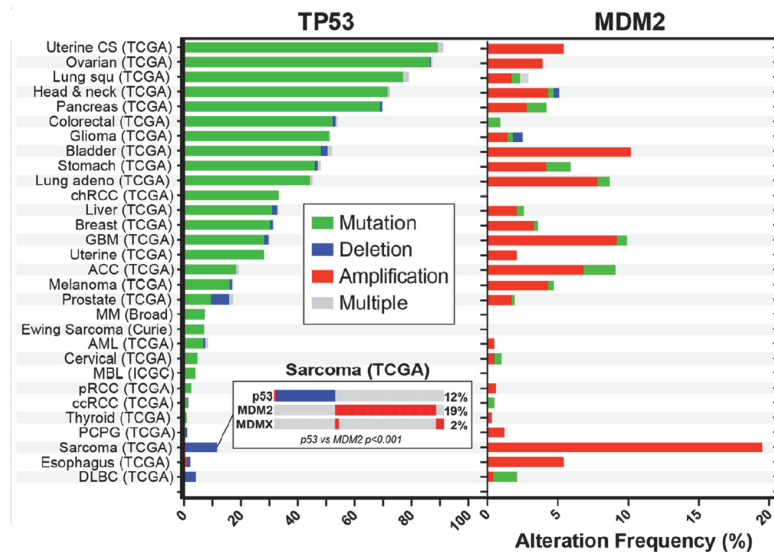


Figure 4:2 Frequency of mutations, deletions and combination of alterations in the genes of p53 and MDM2 in cancers. Adapted from Burgess *et al.*¹⁰⁹

In healthy cells, the cellular concentration of p53 is very low and tightly regulated by the presence of several antagonists¹¹⁰. HDM2 is the most important of them, and its expression levels are controlled by p53 itself, which forms an auto-regulated negative feedback loop¹¹¹. HDM2 exerts the function of an oncogene, mostly in a p53-dependent manner (but not only¹¹²): high HDM2 levels reduce p53 concentrations and therefore are associated with increased cancer risk. The negative regulation of p53 by HDM2 relies mainly on the following mechanisms¹¹²:

- ✓ ubiquitination: HDM2 serves as an E3 ubiquitin protein ligase that targets p53 for proteasomal degradation;
- ✓ nuclear export: HDM2 promotes the translocation of p53 from the nucleus, where it is functional, to the cytoplasm, where it gets degraded¹¹³;
- ✓ occupation of the transactivation domain: the HDM2-binding site of p53 coincides with its N-terminal α -helical domain that is also responsible for its transcriptional activity;
- ✓ block of p53-translational activators: HDM2 is responsible for the ubiquitination of the ribosomal protein L26, known as a p53-translational activator¹¹⁴.

The surface of contact between p53 and HMD2 is notably hydrophobic and small: just a limited number of amino acids have been identified as hot-spots, and they are located on the N-terminal domain for both the partners. In particular, three amino acids on p53 (Phe19, Trp23 and Leu26) have been identified as crucial for the interaction to take place: they all belong to the portion of the transcription factor that has been resolved by crystal-lization in complex with HDM2 (p53₁₅₋₂₉) and that is know to adopt an α -helical confor-mation upon binding¹¹⁵ (cfr. Figure 4:3). Only HDM2 has a structurally defined binding site, and for this reason the vast majority of inhibitors of the p53-HDM2 PPI is represented by molecules that bind to HDM2.

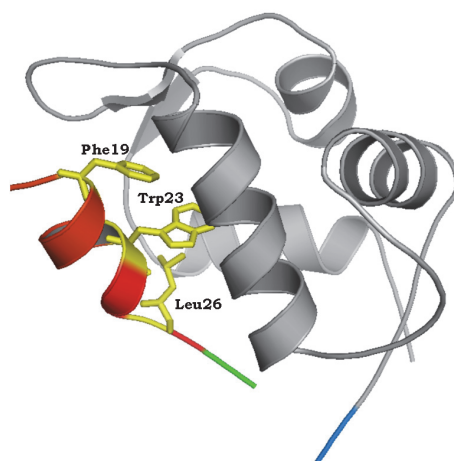


Figure 4:3 Crystal structure of HDM2₁₇₋₁₂₅ (grey) in complex with p53₁₅₋₂₉ (red). The C-terminus of the p53₁₅₋₂₉-peptide is shown in green and the N-terminus of HDM2₁₇₋₁₂₅ is shown in blue. The side chains of the triad of p53 amino acids crucial for the interaction with HDM2 are coloured in yellow (PDB: 1YCR¹¹⁵).

Both p53-derived peptides and small molecules with hydrophobic groups able to mimic the triad of p53's hot spots have been successfully developed as disruptors of the interaction p53-HDM2. Examples of inhibitors are: nutlins, family of cis-imidazolines developed by Roche and displaying K_D s between 0.09 and 14 μM ¹¹⁶ and currently involved in clinical trials¹⁰⁹; the small molecule RG7112 discovered by a team of researchers in Hoffmann-La Roche^{117, 118} and having an IC_{50} of 18 nM; ATSP-7041 developed by Aileron Therapeutics¹¹⁹ and PMI¹²⁰, two cell permeable α -helical staple peptides with binding constants respectively of 0.9 and 3 nM.

4.2 Sensor design

The p53-based sensor follows the model of the HCA-based sensor, differing just in that SNAP-tag is substituted by a portion of p53 and that HCA is replaced by HDM2. As p53 wild-type peptide, the fragment containing residues 15-29 was chosen, since this portion was shown to be the HDM2-interaction partner by crystallography (cfr. Figure 4:3) and since its binding constant ($K_D = 575 \text{ nM}$ ¹²¹) seemed to be at the same time suitably strong to close the sensor in the absence of inhibitors and weak enough to allow the sensor's opening in presence of inhibitors in the nM- μM range. As for HDM2, after having encountered some difficulties in the expression and purification of the sensor containing the full protein, the sensor was constructed using uniquely the portion 1-125, proven to be necessary and sufficient for p53-binding^{115, 122}. Moreover, since the crystal structure of the complex shows that the C-terminus of the p53₁₅₋₂₉-peptide and the N-terminus of HDM2 are pointing to the same direction (cfr. Figure 4:3, green and blue termini), the two interacting partners were placed respectively at the N-terminus and at the C-terminus of the fusion protein, in order to preserve the good relative orientation (cfr. Figure 4:4).

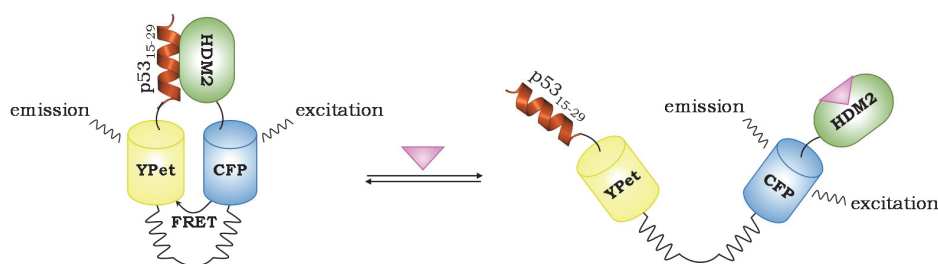


Figure 4:4 Design and working mechanism of the p53-based sensor.

The binding partners being in this case portions of two proteins, the sensor was entirely genetically encodable and no labelling was required to make it functional. This feature made it particularly attractive for intracellular application, since the experiments could be performed without any preliminary cell treatment and with minimal perturbation of the cells.

4.3 Sensing inhibitors of the interaction p53-HDM2 *in vitro*

4.3.1 *In vitro* titration of inhibitors of the p53-HDM2 interaction

The sensor was successfully expressed in HEK 293 cells and isolated by affinity purification thanks to its C-terminal His-tag and N-terminal Strep-tag: 1L of doxycycline-induced HEK 293 cell culture yielded 3.7 mg of pure sensor (cfr. Figure 4:5).

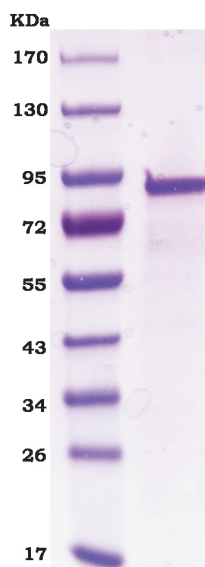


Figure 4:5 SDS-PAGE of the p53-based sensor protein purified from HEK 293 cells.

The ability of the protein to sense both small molecules and peptides inhibitors of the p53-HDM2 interaction was evaluated *in vitro*.

The inhibitors employed in the test (see sequences and structures in Table 4:1 and Figure 4:6) are:

- ✓ three small molecules, namely **Nutlin 3a** and two other imidazole-derivatives (**1CFY** and **5CGU**);

- ✓ the stapled peptide **sMTide CIS**, derived from the sequence of the above-mentioned PMI peptide and isomer of the previously published strong peptide inhibitor called sMTide-02A¹²³;
- ✓ the **D-peptide**, phenylalanine-fluorinated analogue of the PMI-based proteolysis-resistant ^DPMI₇ peptide¹²⁴.

With the exception of Nutlin 3a which is commercially available, all the inhibitors were provided by the industrial partner Dr. T. Vorherr (Director Peptide Discovery, Novartis Institute of BioMedical Research).

Peptide	Sequence
<i>p53</i> ₁₅₋₂₉	NH ₂ -SQETFSDLWKLLPEN-COOH
<i>sMTide CIS</i>	Ac-TSFX _R EYW _{6-Cl} ALLX _S -NH ₂
<i>D-peptide</i>	NH ₂ -dwwplaf _{CF3} eallr-NH ₂

Table 4:1 Sequences of the p53₁₅₋₂₉-peptide and of the peptide inhibitors employed in the experiments. The *i*, *i*+7 isomeric stapling sites in sMTide CIS are indicated with X_R and X_S. D-amino acids are indicated in lowercase letters. W_{6-Cl} is a tryptophan derivatized with a Cl on carbon-6, f_{CF3} is a *para*-trifluoromethyl derivatized D-phenylalanine.

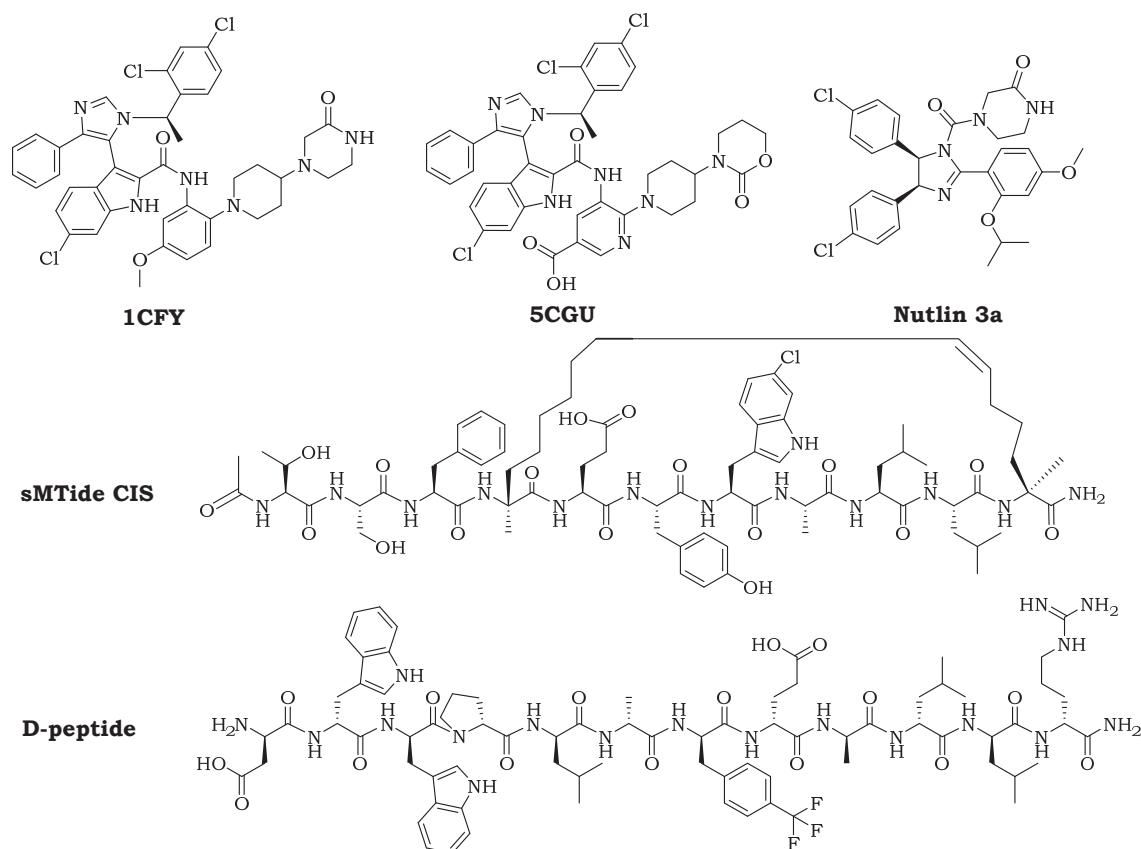


Figure 4:6 Chemical structures of the inhibitors of the interaction p53-HDM2 employed in the experiments.

As explained in Chapter 1.2.1 and 3.3.3 for the HCA-based sensor, in absence of inhibitors the sensor was expected to maintain a closed conformation, characterized by the proximity between CFP and YPet which leads to high FRET; on the other hand, the presence of increasing concentration of inhibitor displaces progressively the intramolecular ligand, shifts

the sensor to the open conformation and provokes therefore a decrease of FRET. This gradual effect is clearly visible in the emission spectra of the sensor on varying the sMTide CIS concentration (cfr. Figure 4:7 (B)).

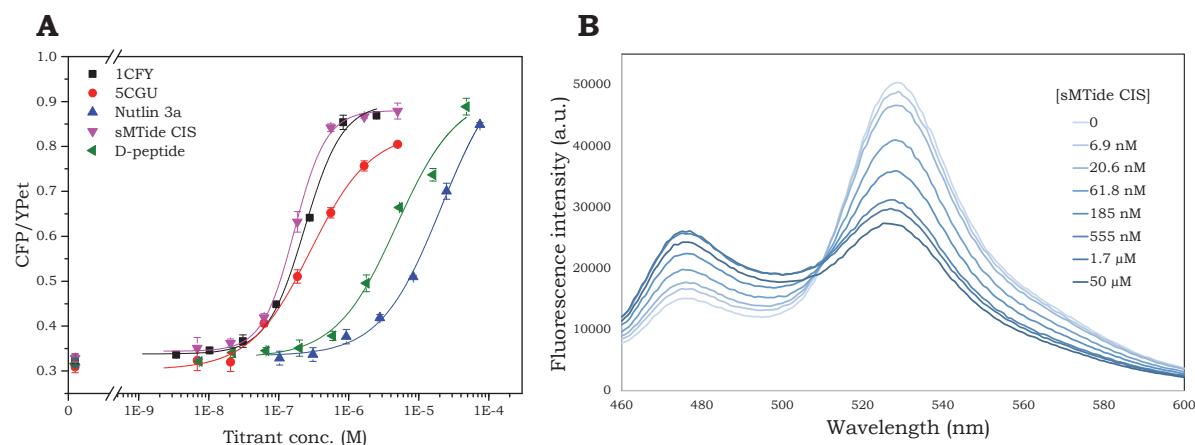


Figure 4:7 (A) Fluorescence titration curve of different inhibitors with the p53-based sensor. Each plot shows the ratio donor (CFP) over acceptor (YPet) emission against the concentration of inhibitor; the data were fitted to a single-site binding isotherm or to a Hill's equation (cfr. Chapter 6.2.4). (B) Fluorescence emission spectra of the p53-based sensor in presence of different concentrations of sMTide CIS.

<i>Inhibitor</i>	C_{50} (nM)	K_D^{comp} (nM)	K_D (nM)	K_D ref. (nM)	<i>Solubility</i> (μM)
1CFY	331 ± 67	258 ± 37	2.3 ± 0.5	2 ¹²⁵	<4 ^[a]
5CGU	205 ± 12	74 ± 6	0.7 ± 0.1	2 ¹²⁵	120 ^[a]
Nutlin 3a	~ 20 · 10 ³	<10 · 10 ³	<90	90 ¹¹⁶ , 9 ¹²⁵	<130 ^[b]
sMTide CIS	212 ± 38	166 ± 24	1.5 ± 0.3	(7, sMTide-02A ¹²³)	240 ^[a]
D-peptide	~ 5 · 10 ³	<5 · 10 ³	<45	(53, ^D PMI _V ¹²⁴)	n.d.

Table 4:2 *In vitro* C_{50} , K_D^{comp} and K_D of the analytes for the p53-based sensor. The reference K_D were either published for analogues of the peptide used or calculated by the coworkers at Novartis by TR-FRET assay (displacement of N-terminally Cy5- labelled p53(18-26)). The solubility limits were calculated: [a] by the coworkers at Novartis¹²⁵, at pH=6.8; [b] in our laboratory by light absorbance at 280 nm, at pH=7.2.

As noticeable in Figure 4:7 (A), for 5CGU, Nutlin 3a and D-peptide the titration curves could not be completed at high concentrations because of their limited solubility in aqueous solution. This prevented a precise calculation of the sensor binding parameters (in particular for Nutlin 3a and D-peptide, cfr. Table 4:2); yet these values could be estimated. Noteworthy, the titration curves of 1CFY and sMTide CIS required a fitting with binding isotherms characterized by an Hill's coefficient equal to 2 (cfr. Chapter 6.2.4), which might indicate the presence of two binding sites on HDM2 for these compounds; however, this hypothesis was not further investigated.

The p53-based sensor displayed an average maximum FRET-ratio change of $170 \pm 6\%$ and was proven to be suitable for the detection of inhibitors characterized by K_D for HDM2 in the low nanomolar range, which is the typical range of binding constants of most of the drug candidates developed by pharmaceutical companies to target the p53-HDM2 interaction⁵⁶.

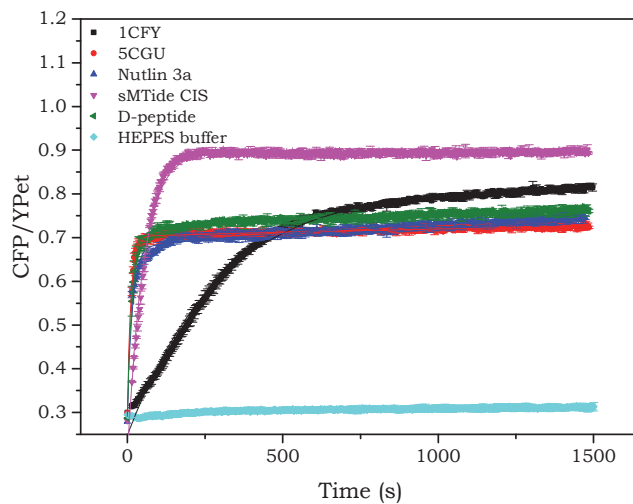
The poor solubility of the peptide p53₁₅₋₂₉ made the measure of its K_D^{comp} impossible by direct titration with the sensor. The M_{eff} of the latter was estimated by replacing the constants of with the values calculated for one of the inhibitors (*e.g.* Nutlin 3a) in the titration experiment:

$$M_{eff} = \frac{K_D^{comp, analyte}}{K_D^{analyte}} \times K_D^{int. ligand} \sim \frac{10000 \text{ nM}}{90 \text{ nM}} \times 575 \text{ nM} = 64 \mu\text{M}$$

The $K_D^{analyte}$ listed in Table 4:2 were calculated on the basis of this value of M_{eff} and they are in close agreement with those found in literature. This value was significantly higher than the one obtained for the HCA-based sensor (*cfr.* Chapter 3.3.3).

4.3.2 *In vitro* opening kinetics of the sensor in presence of inhibitors of the interaction p53-HDM2

The *in vitro* characterization of the p53-based sensor was complemented with the measurements of the opening kinetics at 37°C upon addition of inhibitors. The compounds were tested at the highest concentration employed in the titration experiment: as visible in the titration curves of Figure 4:7, the concentration was saturating for sMTide CIS, right at the limit of saturation for 1CFY and below saturation for 5CGU, Nutlin 3a and D-peptide. The FRET-ratio curve against time for each inhibitor shown in Figure 4:8 required to be fit with a bi-exponential function (*cfr.* Chapter 6.2.4): the first component mainly describes the opening of the sensor protein (first part of the curve) and the second component describes a slight increase of FRET ratio over the time of the experiment that was more pronounced with some inhibitors and that could not be rationalized (end of the curve). For each inhibitor, the half-life of the first exponential component of the fitting was calculated as mean and standard deviation of three independent experiments and reported in Table 4:3.



Inhibitor	$t_{1/2, open}^1$ (s) <i>in vitro</i>
1CFY (2.5 μM)	217 \pm 12
5CGU (10 μM)	9.4 \pm 0.2
Nutlin 3a (75 μM)	12.0 \pm 0.4
sMTide CIS (5 μM)	43 \pm 13
D-peptide (48 μM)	12 \pm 4

Table 4:3 *In vitro* opening half-lives of the first component of the bi-exponential fitting function of the p53- based sensor in presence of inhibitors at 37°C.

Figure 4:8 Example of opening kinetics *in vitro* of the p53-based sensor in presence of the inhibitors or HEPES buffer.

The results of the experiment showed that the fastest opening kinetics were attained with 5CGU, Nutlin 3a and D-peptide, despite the fact that these inhibitors were employed at undersaturating concentrations. This showed that, contrary to what was obtained with the

HCA-based sensor (cfr. Chapter 3.3.4), the unbinding of the internal peptide ligand was fast enough to allow the differentiation between the sensor's binding kinetics of sMTide CIS and 1CFY versus those of the fast binders 5CGU, Nutlin 3a and D-peptide. Unfortunately the presence of a dead time of 15 seconds between the addition of inhibitor and the beginning of the fluorescence recording prevented the precise measurement of the k_{off} of the internal p53-peptide, which however was estimated higher than $60 \cdot 10^{-3} \text{ s}^{-1}$. Slower sensor's opening kinetics were obtained with the inhibitors sMTide CIS and 1CFY, which also required an Hill's coefficient equal to 2 in the fitting of the titration curves: these two effects might be related, but further investigation would be necessary for drawing any relevant conclusion.

4.4 Sensing inhibitors of the interaction p53-HDM2 *in cellulo*

To verify the applicability of the biosensor for intracellular detection of disruptors of the p53-HDM2 interaction, a doxycycline-inducible U2OS cell line was generated and tested in both titration and kinetic experiments, exactly as described in Chapter 3.4 for the sensor for HCA inhibitors. The U2OS cell line was particularly suitable for the validation of the biosensor: it expresses wild-type p53 and normal levels of the HDM2 protein¹²⁶ and it is therefore considered as a good background cell line for a p53-based probe. The sensor showed a relatively homogeneous cellular distribution (cfr. Figure 4:9).

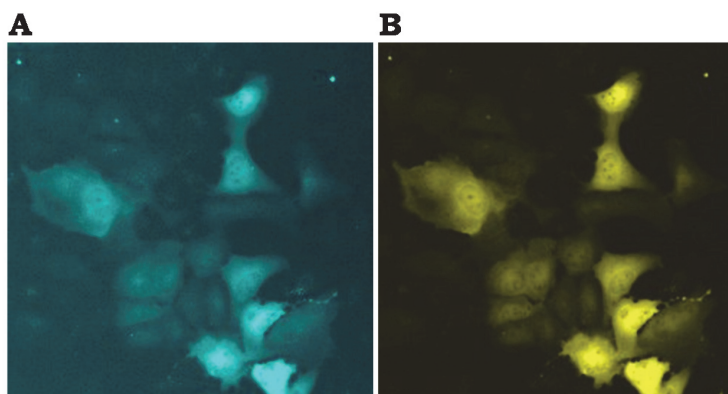
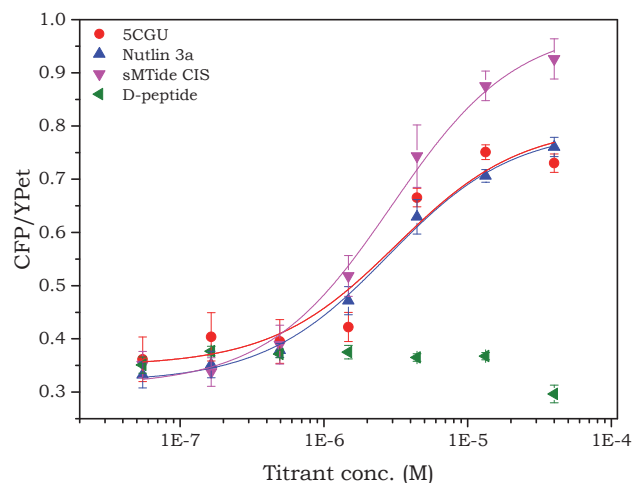


Figure 4:9 Example of microscopy images of the U2OS cell line expressing the p53-based sensor. After CFP excitation, the CFP emission image (A) and the YPet emission image (B) were registered.

4.4.1 *In cellulo* titration of the p53-HDM2 interaction inhibitors

Intracellular titration experiments were performed with all the inhibitors previously characterized *in vitro* except for compound 1CFY, considered unsuitable for cellular assays because of its low solubility. As visible in Figure 4:10, the titration showed that the p53-based sensor responded to the inhibitors in a dose-dependent manner, as expected.



<i>Inhibitor</i>	<i>C₅₀ in cellulo (μM)</i>	<i>C₅₀ in vitro (nM)</i>
5CGU	3 ± 2	205 ± 12
Nutlin 3a	2.8 ± 0.4	~ 20 · 10 ³
sMTide CIS	~3.0 ± 0.6	212 ± 38
D-peptide	n.d.	~ 5 · 10 ³

Table 4:4 Comparison between *in cellulo* and *in vitro* C₅₀s of the p53-HDM2 interaction inhibitors.

Figure 4:10 *In cellulo* fluorescence titration curve of different inhibitors with the p53-based sensor.

The similarity between the *in cellulo* C₅₀ of 5CGU and of Nutlin 3a did not reflect the difference of two orders of magnitude measured *in vitro*: this result suggested that in the cell line the sensor was titrated instead of the inhibitors, because presumably its doxycycline-induced intracellular concentration reached levels comparable to the C₅₀ of the compounds (around 3 μM). However, a direct measure of the intracellular sensor's concentration would be necessary to confirm this hypothesis.

Interestingly, the highest concentration of sMTide CIS employed in the titration (40 μM) showed a high degree of cytotoxicity against the U2OS cell line: in just 2h of incubation this concentration of compound triggered the acute death of approximately 60-70% of the cells (estimation by eye, cfr. Figure 4:11).

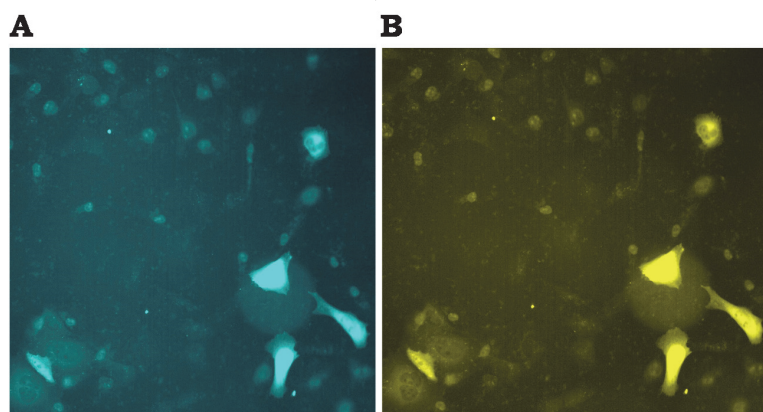


Figure 4:11 Microscopy images of the U2OS cell line 2h after incubation with sMTide CIS 40 μM. After CFP excitation, the CFP emission image (A) and the YPet emission image (B) were registered.

Nevertheless, the FRET-ratio could still be measured in the surviving cells, and this allowed to complete the curve and to get a plausible estimation of its C₅₀ around 3 μM. This toxic effect was observed only for the peptide sMTide CIS at concentration above 10 μM and was also monitored in time-lapse imaging experiments.

Another important result of the titration experiment consisted in the unresponsiveness of the intracellular sensor to the incubation with D-peptide (cfr. Figure 4:10, green dots), which might prove that the peptide is as poorly permeable to the cell membrane as its analogue $^D\text{PMI}_\gamma$ peptide¹²⁴. As this latter moreover, when applied to the cells the D-peptide did not show any toxicity either in the titration or in kinetic experiments.

Overall, the p53-based sensor exhibited a good intracellular FRET-ratio change of about 170% with sMTide CIS and 130% with compounds 5CGU and Nutlin 3a. These values were close to the one obtained *in vitro* and were optimal to allow reliable fluorescence microscopy measurements of the cell entry kinetics of the small molecule and peptide inhibitors in hand.

4.4.2 *In cellulo* kinetic characterization of the sensor in presence of inhibitors of the interaction p53-HDM2

The p53-based sensor was successively tested for time-resolved *in cellulo* sensing of the inhibitors, as described in Chapter 3.4.2 for the HCA-based sensor: the cell line was seeded in 96-well plates, the compounds were added at suitable concentrations (below the limit of solubility and toxicity) and the time-lapse microscopy imaging was started. Also, washout experiments were performed on the cells incubated with small molecule inhibitors, which displayed fast kinetics. On the other hand, they were not performed on the cells incubated with peptidic inhibitors: the hours-long incubation in HBSS nutriment-free buffer required in this case, in fact, was likely to trigger undesired cellular stress responses.

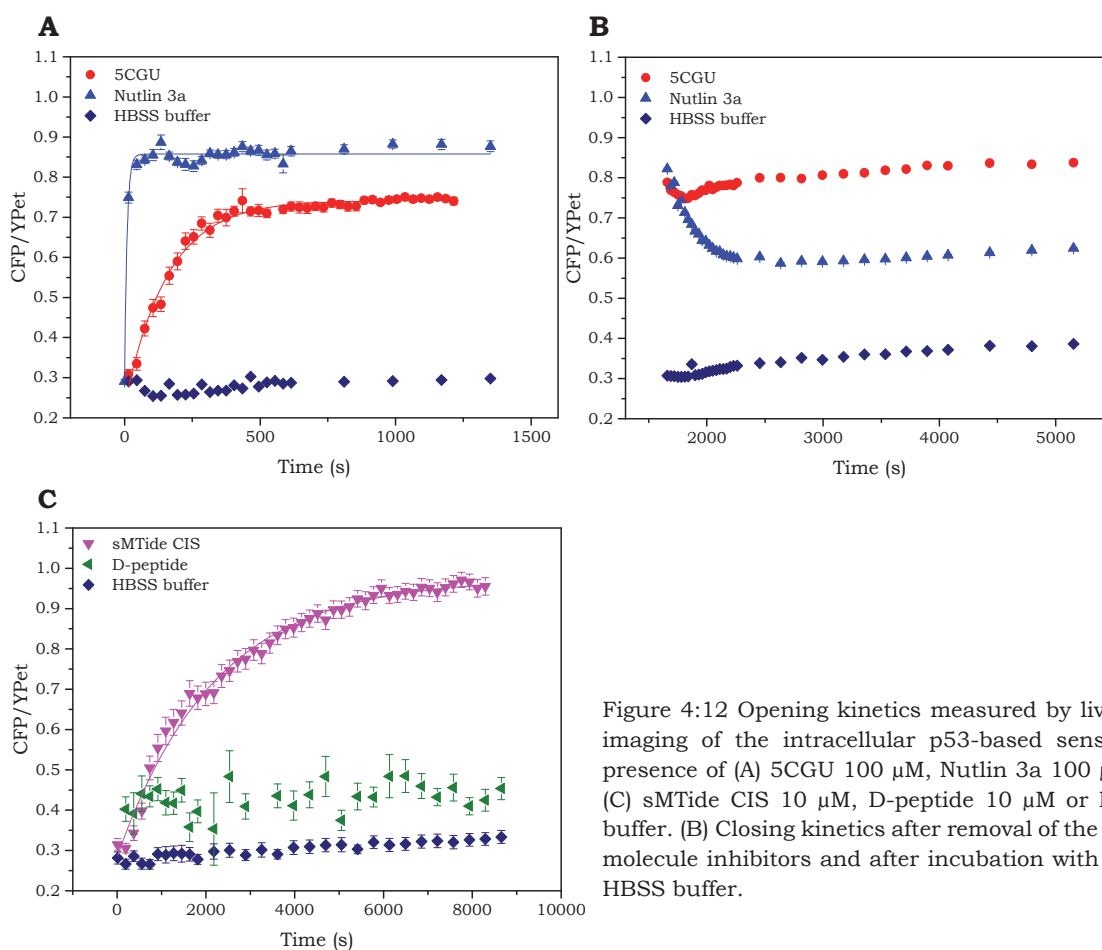


Figure 4:12 Opening kinetics measured by live cell imaging of the intracellular p53-based sensor in presence of (A) 5CGU 100 μM , Nutlin 3a 100 μM or (C) sMTide CIS 10 μM , D-peptide 10 μM or HBSS buffer. (B) Closing kinetics after removal of the small molecule inhibitors and after incubation with fresh HBSS buffer.

<i>Inhibitor</i>	<i>t_{1/2,open}(s)</i> <i>in cellulo</i>	<i>t_{1/2,open}¹(s)</i> <i>in vitro</i>
5CGU (100 μ M)	115 \pm 7	n.d.
Nutlin 3a (100 μ M)	6 \pm 1	n.d.
5CGU (10 μ M)	651 \pm 94	9.4 \pm 0.2
Nutlin 3a (10 μ M)	83 \pm 16	n.d.
sMTide CIS (10 μ M)	1518 \pm 92	43 \pm 13
D-peptide (10 μ M)	n.d.	12 \pm 4

Table 4:5 Comparison between the opening half-lives measured *in cellulo* and *in vitro* of the p53-based sensor in presence of inhibitors.

In accordance with what expected following the results of the *in vitro* characterization, the fast opening kinetics of the p53-based sensor allowed the differentiation between the cell entry rates of the small molecule inhibitors tested (cfr. Figure 4:12 (A)), even though a precise measurement of the maximal intracellular sensor opening rate was prevented by the presence of a deadtime of about 15 seconds between the addition of inhibitor and the beginning of the fluorescence microscopy imaging.

Despite the technical limitations, we could observe that the opening of the intracellular sensor triggered by the addition of Nutlin 3a at 100 μ M to the cells took place in less than 10 seconds, which is in agreement with previously published data on the intracellular inhibition kinetics of p53–HDM2 interaction induced by Nutlin 3¹²⁷. Compound 5CGU, which *in vitro* exhibited a C₅₀ two orders of magnitude lower than Nutlin 3a and comparable sensor interaction kinetics, opened the intracellular sensor 8 to 18 times slower than Nutlin 3a, the applied concentration of the inhibitors being equal. This outcome reflects an inferior ability of 5CGU to transit through the cell membrane, presumably because of the presence of a carboxylic acid in the molecular structure of the compound (cfr. Figure 4:6). As for sMTide CIS, the intracellular sensor's opening half-life obtained with the peptide was remarkably slow compared to that of the small molecules (cfr. Figure 4:12 (C)): at the same concentration 5CGU and Nutlin 3a enter the cells 2 to 18 times faster. This difference might reflect the fact that the peptide is internalized via active transport, since endosomal release has to be accomplished before the opening of the cytosolic sensor can take place.

The cell clearance rates of the two small molecule inhibitors were also evaluated (cfr. Figure 4:12 (B)). Interestingly, Nutlin 3a showed to be able to move very fast both in and out the cellular space, whereas no FRET-ratio decrease was detected in the cells treated with 5CGU following the incubation with fresh HBSS buffer: the compound seemed to be retained in the intracellular environment, in a similar way as acetazolamide (cfr. Chapter 3.4.2).

4.4.3 Conclusions and outlook

In this chapter the design and the performances of a novel FRET-based biosensor for disruptors of the p53-HDM2 interaction is presented. The sensor consists in a single-chain fusion protein molecule, which offers the advantage of being entirely genetically encodable and not requiring any labelling with synthetic molecules. Moreover, as additional benefit with respect to previously published p53-HDM2 PPI targeting systems^{127, 128}, our biosensor

provides an intramolecular ratiometric readout, which eliminates the problem of the relative stoichiometry of the FRET-partners¹²⁹.

At first, the sensor was tested and characterized *in vitro*, where it displayed a high and reproducible FRET-ratio change of about 170%, very fast opening kinetics and a response that falls in an appropriate inhibitors' concentration window (high nM to high μ M), where most of the developed p53-HDM2 interaction disruptors show therapeutic efficacy. Afterwards, in live cells fluorescence imaging, the sensor maintained a high FRET-ratio dynamic range and allowed to follow in real-time the disruption of the intra-sensor p53-HDM2 interaction triggered by a selection of small molecule and peptidic inhibitors. These assays revealed the low cellular permeability of the D-peptide and important differences between the cell entry kinetics of small molecule and peptide inhibitors. Two compounds with equally fast binding kinetics *in vitro*, 5CGU and Nutlin 3a, showed significative differences in cellular uptake rates, which might be explained by considerations on their chemical structure.

The described biosensor presents itself as a valuable technology for time-resolved monitoring of the cellular uptake of various unmodified p53-HDM2 PPI inhibitors. Its simplicity and the minimal manipulation required for cellular assays makes it a promising tool for characterizing new drugs, improving their rational design and, eventually, for high-throughput screening. Further work on the project would focus on the applicability of the sensor for reliable measurements of intracellular inhibitors' concentration, which would require a tighter control of the sensor's expression level in the cells to keep them below the range of C_{50} of the compounds of interest. Finally, the presented strategy, thanks to its versatility and practicality, could be adapted to investigate other protein-protein interactions and their inhibition in living cells.

Chapter 5 General conclusions

The existing techniques to estimate the cellular permeability of molecules when they are non-cell based often fail in properly mimicking the complexity of biological membranes. On the other hand, cell-based techniques are too laborious, cell-type specific and have poor temporal-resolution. The work presented in this thesis aims to offer an alternative method.

The two biosensors described here enable one to evaluate in real-time in living cells the extent and the kinetics of cellular uptake and clearance of underivatized molecules. Two big families of clinically relevant, underivatized compounds were targeted: inhibitors of the enzyme human carbonic anhydrase II (HCAII), most of which are already commercialized drugs, and inhibitors of the p53-HDM2 interaction, whose disruptors are nowadays protagonists of several cancer therapies. Our strategy was proved to be versatile and adaptable to the characterization of inhibitors of both ligand-protein and protein-protein interactions. Compounds belonging to the same family could be compared with respect to their binding constants to the target and, most importantly, with respect to their ability to access and exit the intracellular space. Significant differences were detected, could often be rationalized based on the chemical structure of the molecules and resulted in agreement with previously published data, when available.

Pharmaceutical companies have always had great interest in improving the efficiency and reducing the time and costs of drug candidates' profiling. The biosensors presented in the thesis can find applications in this context, for the establishment of fast, cheap, non-invasive and versatile assays that allow the combined evaluation of biological activity and cellular permeability of potential drug leads. Finally, thanks to its modular design, our technology can eventually be adapted to the detection of different families of clinically relevant chemical entities.

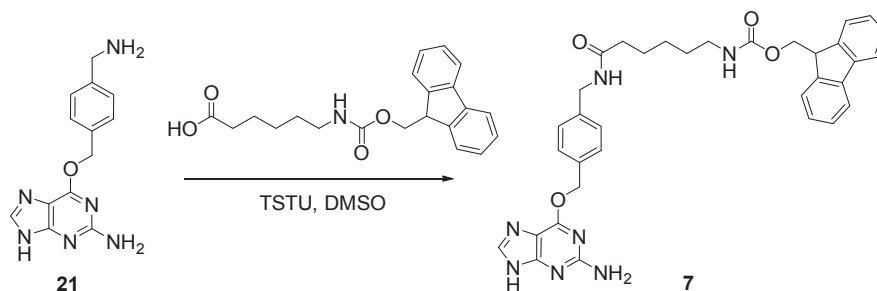
Chapter 6 Materials and Methods

6.1 Chemical synthesis

6.1.1 General information

All solvents and chemicals were purchased from Sigma-Aldrich, Fisher Scientific, Merck, Fluka, Acros and were used without any further purification. Reverse-phase preparative high-pressure liquid chromatography (Prep-HPLC) was performed on a Dionex system equipped with an UltiMate 3000 pump and an UV D170U UV-Vis detector for product visualization on a Waters SunFire Prep C18 OBD 5 μm 10 \times 150 mm Column. Buffer A: 0.1% TFA in H₂O Buffer B: acetonitrile. Typical gradient was from 0% to 100% B within 25 min with 4 ml min⁻¹ flow. ¹H and ¹³C nuclear magnetic resonance (NMR) spectra were recorded at room temperature respectively on a Bruker DPX 400 (400 MHz) and on a Bruker Avance III HD 600 (600 MHz), with chemical shifts (δ) reported in ppm relative to the solvent residual signals. CD₂Cl₂: δ H 5.3 ppm, δ C 53.84; D₆-DMSO: δ H 2.5 ppm, δ C 39.5 ppm; CD₃OD: δ H 3.31 ppm, δ C 49.0 ppm. Coupling constants are reported in Hz. High resolution mass spectra (HRMS) were measured on a Micromass Q-ToF Ultima spectrometer with electron spray ionization (ESI).

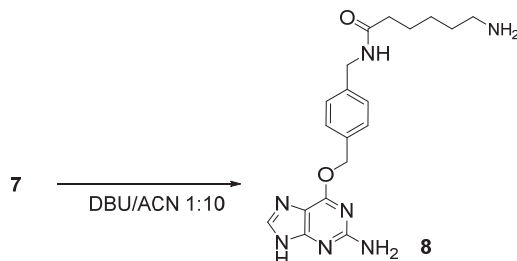
6.1.2 Synthesis of compounds



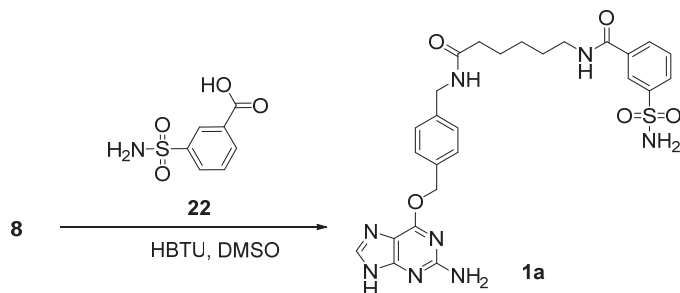
(9H-fluoren-9-yl)methyl 6-((((2-amino-9H-purin-6-yl)methoxy)methyl)benzyl)amino)-6-oxohexylcarbamate (7) 6-((((9H-fluoren-9-yl)methoxy)carbonyl)amino)hexanoic acid (106 mg, 300 μmol) was dissolved in 0.4 ml of DMSO; DIPEA (105 μl , 600 μmol) and TSTU (100 mg, 330 μmol) were then added, and the mixture was stirred during 15 min at room temperature. A solution of 6-((((aminomethyl)benzyl)oxy)-9H-purin-2-amine (**21***, 81 mg, 300 μmol) in 0.4 ml of DMSO was added to the previous mixture and the stirring continued for other 60 min. 0.3 ml of H₂O and 250 μl of glacial acetic acid were then added and the mixture was purified by preparative HPLC. The fractions containing the product were checked by HRMS (ESI) and lyophilized to give compound **7** (54.0 mg, 89 μmol , 30%). [HRMS (ESI) calculated for C₃₄H₃₆N₇O₄⁺ [M+H]⁺ 606.2823; found 606.2823. ¹H NMR (400 MHz, DMSO-d₆) δ 8.43 (s, 1 H), 8.33 (t, 1 H, J = 5.9 Hz), 7.89 (d, 2 H, J = 7.4 Hz), 7.69 (d, 2 H, J = 7.4 Hz), 7.49 (d, 2 H, J = 8.0 Hz), 7.41 (t, 2 H, J = 7.4 Hz), 7.33 (td, 2 H, J = 1.1,

7.4 Hz), 7.29 (d, 2 H, J = 8.0 Hz), 5.52 (s, 2 H), 4.3 (d, 2 H, J = 6.9 Hz), 4.27 (d, 2 H, J = 5.9 Hz), 4.21 (t, 1 H, J = 6.9 Hz), 3.00-2.94 (m, 2 H), 2.13 (t, 2 H, J = 7.4 Hz), 1.56-1.48 (m, 2 H), 1.44-1.37 (m, 2 H), 1.28-1.20 (m, 2 H)].

***21** was synthesized as reported before⁴⁵.

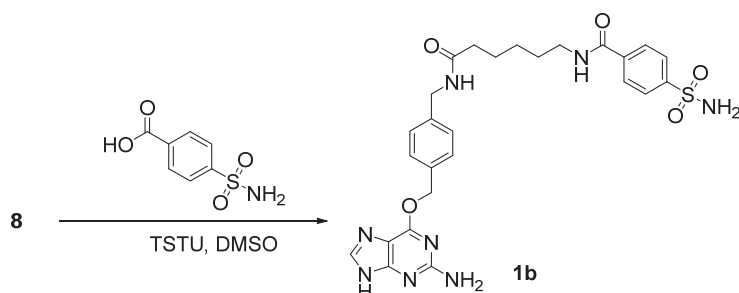


6-amino-N-(4-(((2-amino-9H-purin-6-yl)oxy)methyl)benzyl)hexanamide (8) Compound **7** (28 mg, 46.2 μ mol) was dissolved in 1 ml of a mixture DBU/ACN 1:10 and stirred at room temperature for 30 min; then 250 μ l of glacial acetic acid were added to neutralize the base. After solvent evaporation the mixture was dissolved in 1.5 ml of DMSO, purified by preparative HPLC and lyophilized to give compound **8** (16 mg, 42 μ mol, 91%). [HRMS (ESI) calculated for $C_{19}H_{26}N_7O_2^+$ $[M+H]^+$ 384.2142; found 384.2147. 1H NMR (400 MHz, DMSO- d_6) δ 8.37 (t, 1 H, J = 5.9 Hz), 8.29 (s, 1 H), 7.72 (s, 2 H), 7.49 (d, 2 H, J = 8.0 Hz), 7.28 (d, 2 H, J = 8.0 Hz), 5.52 (s, 2 H), 4.27 (d, 2 H, J = 5.9 Hz), 2.81-2.73 (m, 2 H), 2.14 (t, 2 H, J = 7.4 Hz), 1.57-1.49 (m, 4 H), 1.33-1.24 (m, 2 H)].

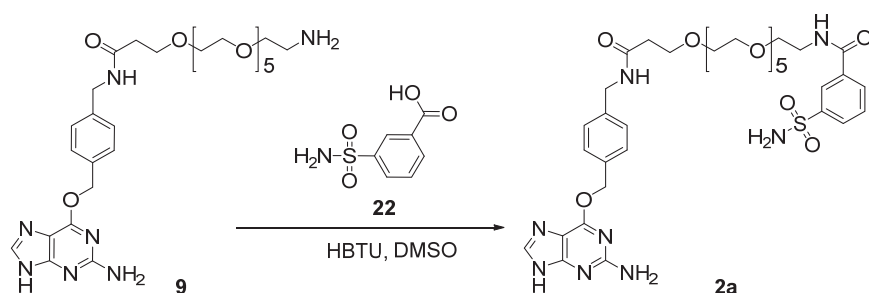


N-(6-((4-(((2-amino-9H-purin-6-yl)oxy)methyl)benzyl)amino)-6-oxohexyl)-3-sulfamoylbenzamide (1a) 3-sulfamoylbenzoic acid (**22***, 13 mg, 65 μ mol) was dissolved in 0.7 ml of DMSO together with HBTU (25 mg, 65 μ mol) and DIPEA (66 μ l, 379 μ mol); the mixture was stirred at room temperature for 15 min. Compound **8** was then added and the reaction was left under stirring during 30 min at room temperature. 200 μ l of H_2O and 200 μ l of glacial acetic acid were added. The reaction mixture was purified by preparative HPLC and lyophilized to give the product **1a** (18 mg, 32 μ mol, 76%). [HRMS (ESI) calculated for $C_{26}H_{31}N_8O_5S^+$ $[M+H]^+$ 567.2133; found 567.2139. 1H NMR (400 MHz, DMSO- d_6) δ 8.63 (t, 1 H, J = 5.9 Hz), 8.26-8.23 (m, 2 H), 7.98-7.95 (dm, 1 H, J = 7.8 Hz), 7.88 (ddd, 1 H, J = 7.8, 1.8, 1.1 Hz), 7.60 (t, 1 H, J = 7.8 Hz), 7.41 (d, 2 H, J = 8.0 Hz), 7.37 (s, 2 H), 7.20 (d, 2 H, J = 8.0 Hz), 5.44 (s, 2 H), 4.19 (d, 2 H, J = 5.9 Hz), 3.22-3.17 (m, 2 H), 2.08 (t, 2 H, J = 7.4 Hz), 1.53-1.43 (m, 4 H), 1.27-1.17 (m, 2 H). ^{13}C NMR (151 MHz, MeOD) δ 174.6, 167.2, 159.7, 144.3, 139.6, 135.4, 134.0, 130.1, 128.8, 127.4, 124.7, 69.4, 42.3, 39.6, 35.5, 28.7, 26.2, 25.3].

***22** was synthesized as reported before⁵⁰.

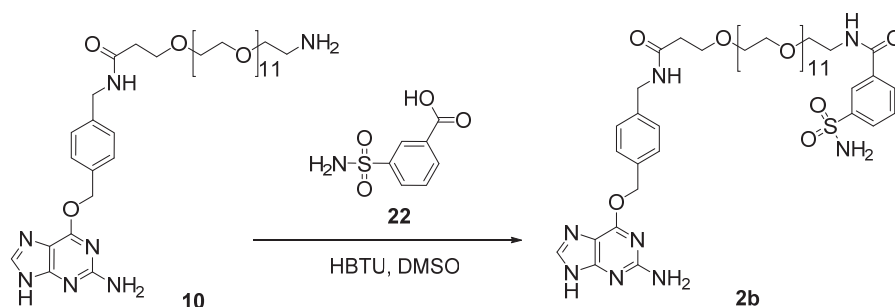


N-(6-((4-((2-amino-9H-purin-6-yl)oxy)methyl)benzyl)amino)-6-oxohexyl)-4-sulfamoylbenzamide (1b**)** 4-sulfamoylbenzoic acid (16 mg, 80 μ mol) was dissolved in 0.75 ml of DMSO together with TSTU (8 mg, 26 μ mol) and DIPEA (20 μ l, 209 μ mol); the mixture was stirred at room temperature for 15 min. Compound **8** (10 mg, 26 μ mol) was then added and the reaction was left under stirring during 30 min at room temperature. 200 μ l of H₂O and 200 μ l of glacial acetic acid were added. The reaction mixture was purified by preparative HPLC and lyophilized to give the product **1b** (3 mg, 5.3 μ mol, 20%). [HRMS (ESI) calculated for C₂₆H₃₁N₈O₅S⁺ [M+H]⁺ 567.2133; found 567.2139. ¹H NMR (600 MHz, MeOD) δ 8.32 (s, 1 H), 7.98-7.93 (m, 4 H), 7.50 (d, 2 H, J = 8.1 Hz), 7.34 (d, 2 H, J = 8.1 Hz), 5.63 (s, 2 H), 4.39 (s, 2 H), 3.40 (t, 2 H, J = 7.1 Hz), 2.68 (s, 1 H), 2.29 (t, 2 H, J = 7.3 Hz), 1.77-1.62 (m, 4 H), 1.48-1.40 (m, 2 H). ¹³C NMR (151 MHz, MeOD) δ 174.6, 167.4, 146.3, 139.6, 137.8, 128.8, 127.5, 127.4, 125.9, 69.3, 42.3, 39.6, 35.5, 28.7, 26.2, 25.6, 25.2].



N-(4-((2-amino-9H-purin-6-yl)oxy)methyl)benzyl)-1-oxo-1-(3-sulfamoylphenyl)-6,9,12,15,18,21-hexaoxa-3-azatetracosan-24-amide (2a**)** Compound **22** (25 mg, 125 μ mol) was dissolved in 1 ml of DMSO together with HBTU (47 mg, 125 μ mol) and DIPEA (72 μ l, 415 μ mol); the mixture was stirred at room temperature for 15 min. 1-amino-N-(4-((2-amino-9H-purin-6-yl)oxy)methyl)benzyl)-3,6,9,12,15,18-hexaoxahenicosan-21-amide (**9***, 50 mg, 83 μ mol) was then added and the reaction was left under stirring during 30 min at room temperature. 200 μ l of glacial acetic acid were added. The reaction mixture was purified by preparative HPLC and lyophilized to give the product **2a** (60 mg, 76 μ mol, 92%). [HRMS (ESI) calculated for C₃₅H₄₉N₈O₁₁S⁺ [M+H]⁺ 789.3236; found 789.3243. ¹H NMR (400 MHz, DMSO-d₆) δ 8.78 (t, 1 H, J = 5.4 Hz), 8.47 (s, 1 H), 8.39 (t, 1 H, J = 6.0 Hz), 8.31 (t, 1 H, J = 1.7 Hz), 8.05 (dt, 1 H, J = 7.8, 1.1 Hz), 7.96 (ddd, 1 H, J = 7.8, 1.7, 1.1 Hz), 7.67 (t, 1 H, J = 7.8 Hz), 7.49 (d, 2 H, J = 8.1 Hz), 7.45 (s, 2 H), 7.29 (d, 2 H, J = 8.1 Hz), 5.53 (s, 2 H), 4.28 (d, 2 H, J = 6.0 Hz), 3.63 (t, 2 H, J = 6.4 Hz), 3.56-3.41 (m, 24 H), 2.38 (t, 2 H, J = 6.4 Hz). ¹³C NMR (101 MHz, DMSO-d₆) δ 170.7, 166.7, 165.6, 159.2, 159.0, 158.6, 145.1, 144.9, 140.6, 135.5, 134.2, 132.9, 132.0, 130.6, 130.2, 130.1, 129.6, 129.5, 128.6, 127.7, 126.9, 125.2, 70.2, 70.1, 70.0, 69.3, 69.0, 67.3].

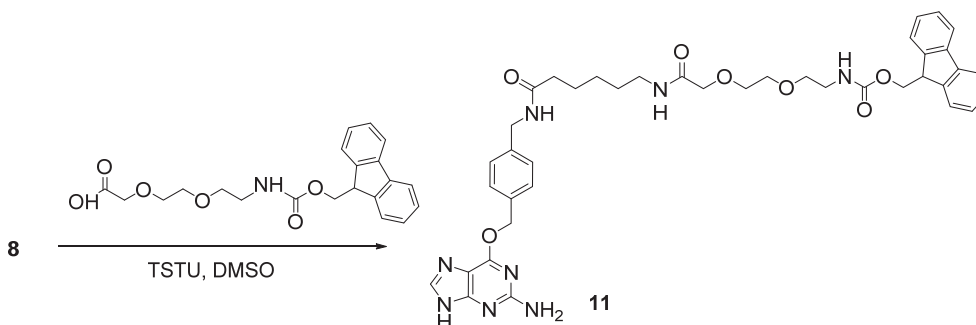
9* was synthesized as reported before¹³⁰.



N-(4-(((2-amino-9H-purin-6-yl)oxy)methyl)benzyl)-1-oxo-1-(3-sulfamoylphenyl)-6,9,12,15,18,21,24,27,30,33,36,39-dodecaoxa-3-azadotetracontan-42-amide (2b)

Compound **22** (6 mg, 30 μ mol) was dissolved in 0.75 ml of DMSO together with HBTU (11 mg, 30 μ mol) and DIPEA (27 μ l, 155 μ mol); the mixture was stirred at room temperature for 15 min. 1-amino-N-(4-(((2-amino-9H-purin-6-yl)oxy)methyl)benzyl)-3,6,9,12,15,18,21,24,27,30,33,36-dodecaoxanonatriacontan-39-amide (**10***, 18 mg, 20 μ mol) was then added and the reaction was left under stirring during 30 min at room temperature. 50 μ l of glacial acetic acid were added. The reaction mixture was purified by preparative HPLC and lyophilized to give the product **2b** (9.5 mg, 9 μ mol, 43%). [HRMS (ESI) calculated for $C_{47}H_{73}N_8O_{17}S^+$ $[M+H]^+$ 1053.4809; found 1053.4813. 1H NMR (400 MHz, DMSO- d_6) δ 8.79 (t, 1 H, J = 5.4 Hz), 8.48 (s, 1 H), 8.40 (t, 1 H, J = 5.7 Hz), 8.32 (d, 1 H, J = 0.7 Hz), 8.06 (dd, 1 H, J = 7.8, 0.9 Hz), 7.97 (dd, 1 H, J = 7.8, 0.9 Hz), 7.68 (t, 1 H, J = 7.8 Hz), 7.50 (d, 2 H, J = 7.8 Hz), 7.43 (s, 2 H), 7.29 (d, 2 H, J = 7.8 Hz), 5.53 (s, 2 H), 4.29 (d, 2 H, J = 5.9 Hz), 3.63 (t, 2 H, J = 6.4 Hz), 3.60-3.40 (m, 48 H), 2.39 (t, 2 H, J = 6.4 Hz). ^{13}C NMR (151 MHz, DMSO- d_6) δ 170.6, 165.5, 144.9, 135.5, 130.6, 129.6, 129.3, 128.6, 127.7, 125.2, 82.3, 70.2, 69.3, 67.3, 42.3, 36.6].

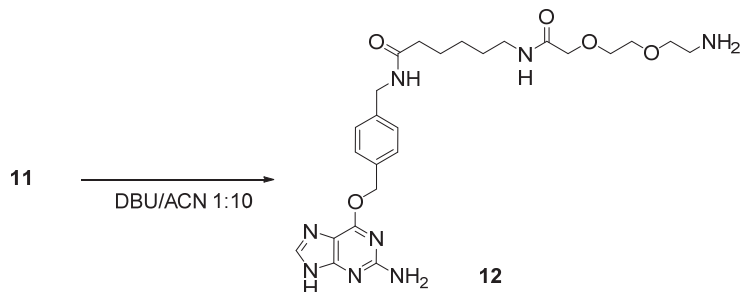
***10** was synthesized as reported before⁴⁴.



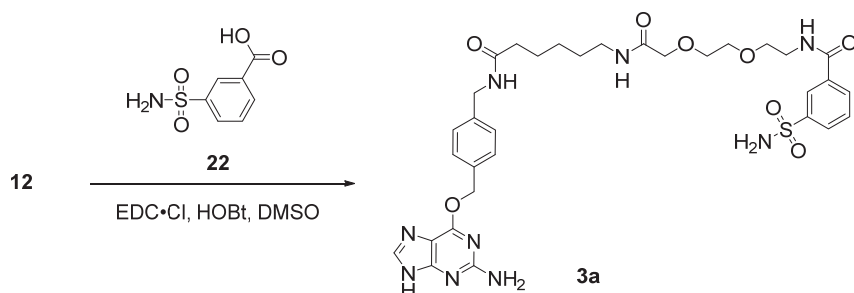
(9H-fluoren-9-yl)methyl (1-(4-(((2-amino-9H-purin-6-yl)oxy)methyl)phenyl)-3,10-dioxo-12,15-dioxa-2,9-diazaheptadecan-17-yl)carbamate (11)

1-(9H-fluoren-9-yl)-3-oxo-2,7,10-trioxa-4-azadodecan-12-oic acid (117 mg, 303 μ mol) was dissolved in 2 ml of DMSO together with TSTU (100 mg, 332 μ mol) and DIPEA (131 μ l, 758 μ mol); the mixture was stirred at room temperature for 30 min. Compound **8** (116 mg, 303 μ mol) was then added and the reaction was left under stirring during 60 min at room temperature. 300 μ l of glacial acetic acid were added. The solution was extracted with 2 \times 40 ml EtOAc and 2 \times 50 ml H_2O . The organics were dried over Mg_2SO_4 , filtered and concentrated. The reaction mixture was purified by preparative HPLC and lyophilized to give the product **11** (150 mg, 200 μ mol, 66%). [HRMS (ESI) calculated for $C_{40}H_{47}N_8O_7^+$ $[M+H]^+$ 751.3562; found 751.3566. 1H NMR (400 MHz, DMSO- d_6) δ 8.30 (t, 1 H, J = 5.9 Hz), 7.90 (d, 2 H, J = 7.5 Hz), 7.70 (d, 2 H, J = 7.5 Hz), 7.67-7.64 (m, 1 H), 7.48 (d, 2 H, J = 8.0 Hz), 7.42 (t, 2 H, J = 7.4 Hz), 7.37-

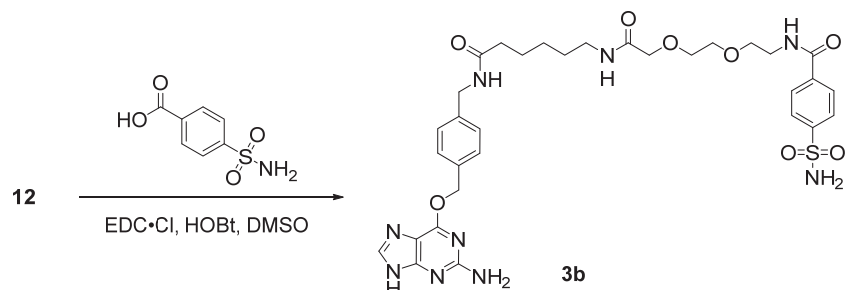
7.31 (m, 3 H), 7.27 (d, 2 H, $J = 8.0$ Hz), 5.50 (s, 2 H), 4.30 (d, 2 H, $J = 6.8$ Hz), 4.26 (d, 2 H, $J = 5.7$ Hz), 4.22 (m, 1 H), 3.86 (s, 2 H), 3.43 (t, 2 H, $J = 5.9$ Hz), 3.18-3.14 (m, 2 H), 3.11-3.06 (m, 2 H), 2.12 (t, 2 H, $J = 7.4$ Hz), 1.55-1.48 (m, 2 H), 1.45-1.38 (m, 2 H), 1.27-1.21 (m, 2 H)].



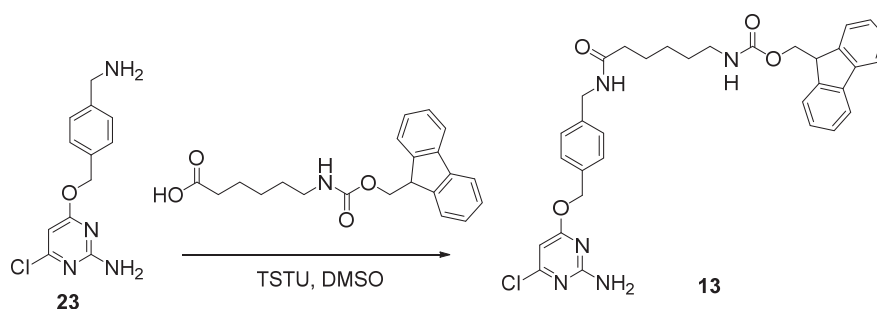
N-(4-(((2-amino-9H-purin-6-yl)oxy)methyl)benzyl)-6-(2-(2-(2-aminoethoxy)ethoxy)acetamido)hexanamide (12) Compound **11** (34 mg, 45 μ mol) was dissolved in 2 ml of a mixture DBU/ACN 1:10 and stirred at room temperature for 45 min; then 300 μ l of glacial acetic acid were added to neutralize the base. After solvent evaporation the mixture was dissolved in 1.5 ml of DMSO, purified by preparative HPLC and lyophilized to give compound **12** (22 mg, 42 μ mol, 93%). [HRMS (ESI) calculated for $C_{25}H_{37}N_8O_5^+$ $[M+H]^+$ 529.2881; found 529.2886. 1H NMR (400 MHz, DMSO- d_6) δ 8.32 (t, 1 H, $J = 5.9$ Hz), 7.75-7.72 (m, 3 H), 7.48 (d, 2 H, $J = 8.1$ Hz), 7.28 (d, 2 H, $J = 8.1$ Hz), 5.49 (s, 2 H), 4.28 (d, 2 H, $J = 5.8$ Hz), 3.90 (s, 2 H), 3.12-3.07 (m, 2 H), 3.02-2.98 (m, 2 H), 2.14 (t, 2 H, $J = 7.4$ Hz), 1.57-1.50 (m, 2 H), 1.47-1.40 (m, 2 H), 1.29-1.21 (m, 2 H)].



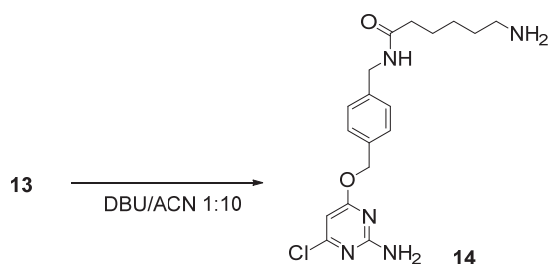
N-(1-(4-(((2-amino-9H-purin-6-yl)oxy)methyl)phenyl)-3,10-dioxo-12,15-dioxa-2,9-diazaheptadecan-17-yl)-3-sulfamoylbenzamide (3a) Compound **22** (6.5 mg, 31 μ mol) was dissolved in 0.75 ml of DMSO; DIPEA (4.5 μ l, 26 μ mol), EDC·Cl (6.5 mg, 34 μ mol) and HOBT (3.5 mg, 26 μ mol) were then added, and the mixture was stirred during 3 min at room temperature. Compound **12** (14 mg, 26 μ mol) was added to the previous mixture and the stirring continued for other 60 min. The mixture was purified by preparative HPLC. The fractions containing the product were checked by HRMS (ESI) and lyophilized to give compound **3a** (13 mg, 18 μ mol, 70%). [HRMS (ESI) calculated for $C_{32}H_{42}N_9O_8S^+$ $[M+H]^+$ 712.2872; found 712.2876. 1H NMR (400 MHz, MeOD) δ 8.37 (s, 1 H), 8.07-8.02 (m, 2 H), 7.64 (t, 1 H, $J = 7.8$ Hz), 7.53 (d, 2 H, $J = 8.0$ Hz), 7.34 (d, 2 H, $J = 8.0$ Hz), 5.63-5.62 (m, 2 H), 4.39 (s, 2 H), 3.99 (s, 2 H), 3.73-3.69 (m, 6 H), 3.64-3.60 (m, 2 H), 3.19 (t, 2 H, $J = 7.1$ Hz), 2.25 (t, 2 H, $J = 7.4$ Hz), 1.67-1.60 (m, 2 H), 1.54-1.47 (m, 2 H), 1.37-1.31 (m, 2 H). ^{13}C NMR (101 MHz, MeOD) δ 174.6, 171.2, 167.4, 144.3, 139.7, 135.2, 133.9, 130.3, 129.1, 128.9, 127.4, 124.8, 70.6, 69.8, 69.5, 69.1, 42.3, 39.6, 39.0, 38.4, 35.5, 28.8, 26.1, 25.2].



N-(1-(4-(((2-amino-9H-purin-6-yl)oxy)methyl)phenyl)-3,10-dioxo-12,15-dioxadecan-17-yl)-4-sulfamoylbenzamide (3b) 4-sulfamoylbenzoic acid (4 mg, 20 μ mol) was dissolved in 0.75 ml of DMSO; DIPEA (3 μ l, 15 μ mol), EDC·Cl (4 mg, 20 μ mol) and HOBT (2 mg, 15 μ mol) were then added, and the mixture was stirred during 3 min at room temperature. Compound **12** (8 mg, 15 μ mol) was added to the previous mixture and the stirring continued for other 60 min. The mixture was purified by preparative HPLC. The fractions containing the product were checked by HRMS (ESI) and lyophilized to give compound **3b** (10 mg, 14 μ mol, 93%). [HRMS (ESI) calculated for $C_{32}H_{42}N_9O_8S^+$ $[M+H]^+$ 712.2872; found 712.2870. 1H NMR (400 MHz, MeOD) δ 7.99-7.95 (m, 4 H), 7.64 (s, 0 H), 7.53 (d, 2 H, J = 8.0 Hz), 7.34 (d, 2 H, J = 8.0 Hz), 5.64-5.63 (m, 2 H), 4.39 (s, 2 H), 3.98 (s, 2 H), 3.73-3.69 (m, 6 H), 3.64-3.60 (m, 2 H), 3.20 (t, 2 H, J = 7.1 Hz), 2.25 (t, 2 H, J = 7.4 Hz), 1.68-1.60 (m, 2 H), 1.55-1.48 (m, 2 H), 1.37-1.31 (m, 2 H). ^{13}C NMR (101 MHz, MeOD) δ 128.8, 127.6, 127.4, 125.9, 70.6, 69.8, 69.2, 69.1, 42.3, 39.6, 39.0, 38.4, 35.5, 28.8, 26.1, 25.2].

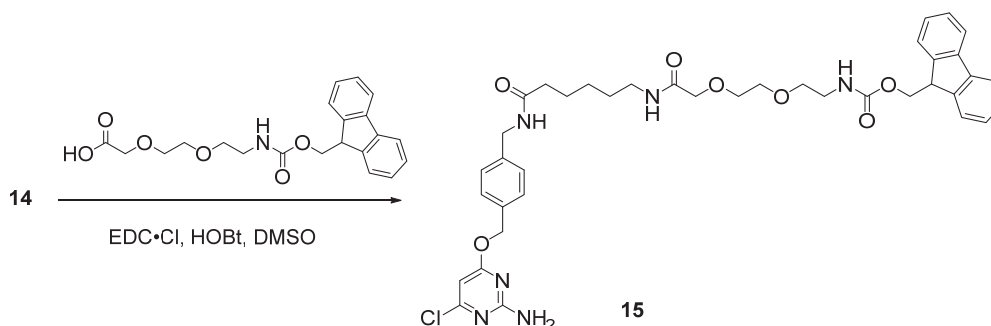


(9H-fluoren-9-yl)methyl (6-(((2-amino-6-chloropyrimidin-4-yl)oxy)methyl)benzyl)amino)-6-oxohexyl)carbamate (13) 6-(((9H-fluoren-9-yl)methoxy)carbonyl)amino)hexanoic acid (80 mg, 226 μ mol) was dissolved in 2.5 ml of DMSO together with TSTU (75 mg, 250 μ mol) and DIPEA (80 μ l, 460 μ mol); the mixture was stirred at room temperature for 30 min. Compound **23** (60 mg, 226 μ mol) was then added and the reaction was left under stirring during 60 min at room temperature. 300 μ l of glacial acetic acid were added. The solution was extracted with 2 \times 30 ml EtOAc and 2 \times 50 ml H_2O . The organics were dried over Mg_2SO_4 , filtered and concentrated. The reaction mixture was purified by preparative HPLC and lyophilized to give the product **13** (70 mg, 117 μ mol, 52%). [HRMS (ESI) calculated for $C_{34}H_{37}ClN_4O_4^+$ $[M+H]^+$ 600.2498; found 600.2372. 1H NMR (400 MHz, DMSO- d_6) δ 8.30 (t, 1 H, J = 5.9 Hz), 7.90 (d, 2 H, J = 7.5 Hz), 7.69 (d, 2 H, J = 7.5 Hz), 7.44-7.38 (m, 4 H), 7.34 (td, 2 H, J = 7.5, 1.0 Hz), 7.30-7.24 (m, 3 H), 7.11 (s, 2 H), 6.13 (s, 1 H), 5.29 (s, 2 H), 4.30 (d, 2 H, J = 6.8), 4.26 (d, 2 H, J = 5.9 Hz), 4.21 (t, 1 H, J = 6.8), 3.00-2.95 (m, 2 H), 2.13 (t, 2 H, J = 7.4 Hz), 1.56-1.49 (m, 2 H), 1.44-1.37 (m, 2 H), 1.28-1.21 (m, 2 H)].



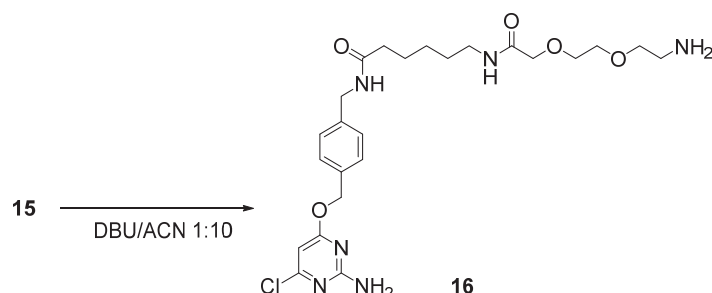
6-amino-N-(4-(((2-amino-6-chloropyrimidin-4-yl)oxy)methyl)benzyl)hexanamide (14)

Compound **13** (70 mg, 117 μmol) was dissolved in 2 ml of a mixture DBU/ACN 1:10 and stirred at room temperature for 45 min; then 300 μl of glacial acetic acid were added to neutralize the base. After solvent evaporation the mixture was dissolved in 2 ml of DMSO, purified by preparative HPLC and lyophilized to give compound **14** (42 mg, 106 μmol , 90%). [HRMS (ESI) calculated for $\text{C}_{18}\text{H}_{25}\text{ClN}_5\text{O}_2$ $[\text{M}+\text{H}]^+$ 378.1691; found 378.1690. ^1H NMR (400 MHz, $\text{DMSO}-d_6$) δ 8.30 (t, 1 H, $J = 5.9$), 7.38 (d, 2 H, $J = 8.1$ Hz), 7.25 (d, 2 H, $J = 8.1$ Hz), 7.11 (s, 2 H), 6.14 (s, 1 H), 5.29 (s, 2 H), 4.25 (d, 2 H, $J = 5.9$ Hz), 2.12 (t, 2 H, $J = 7.4$ Hz), 1.94-1.88 (m, 2 H), 1.55-1.47 (m, 2 H), 1.37-1.30 (m, 2 H), 1.27-1.23 (m, 2 H)].

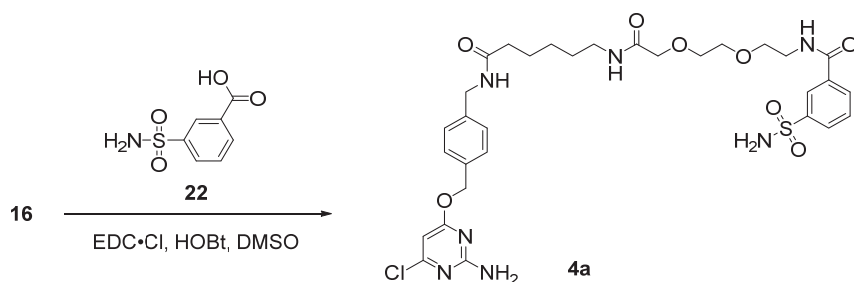


(9H-fluoren-9-yl)methyl (1-(4-(((2-amino-6-chloropyrimidin-4-yl)oxy)methyl)phenyl)-3,10-dioxo-12,15-dioxa-2,9-diazaheptadecan-17-yl)carbamate (15)

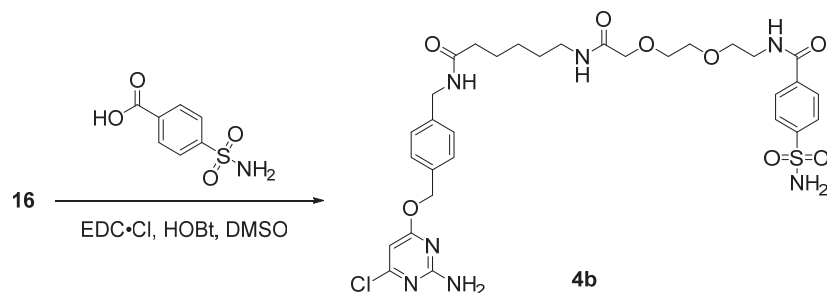
1-(9H-fluoren-9-yl)-3-oxo-2,7,10-trioxa-4-azadodecan-12-oic acid (40 mg, 104 μmol) was dissolved in 2 ml of DMSO; DIPEA (17 μl , 97 μmol), EDC·Cl (22 mg, 113 μmol) and HOBt (12 mg, 87 μmol) were then added, and the mixture was stirred during 3 min at room temperature. Compound **14** (33 mg, 87 μmol) was added to the previous mixture and the stirring continued for other 60 min. The mixture was purified by preparative HPLC. The fractions containing the product were checked by HRMS (ESI) and lyophilized to give compound **15** (40 mg, 54 μmol , 62%). [HRMS (ESI) calculated for $\text{C}_{39}\text{H}_{45}\text{ClN}_6\text{NaO}_7$ $[\text{M}+\text{Na}]^+$ 767.2930; found 767.2932. ^1H NMR (400 MHz, $\text{DMSO}-d_6$) δ 8.30 (t, 1 H, $J = 5.9$ Hz), 7.90 (d, 2 H, $J = 7.5$ Hz), 7.69 (d, 2 H, $J = 7.5$ Hz), 7.43-7.37 (m, 4 H), 7.35-7.31 (m, 2 H), 7.24 (d, 2 H, $J = 8$ Hz), 6.13 (s, 1 H), 5.28 (s, 2 H), 4.30 (d, 2 H, $J = 6.7$), 4.26 (d, 2 H, $J = 5.6$ Hz), 4.21 (t, 1 H, $J = 6.7$), 3.85 (s, 2 H), 3.58-3.53 (m, 4 H), 3.18-3.13 (m, 2 H), 3.11-3.05 (m, 2 H), 2.11 (t, 2 H, $J = 7.3$ Hz), 1.55-1.47 (m, 2 H), 1.45-1.38 (m, 2 H), 1.27-1.20 (m, 2 H)].



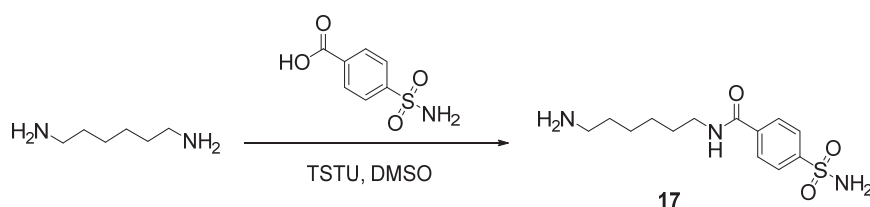
N-(4-(((2-amino-6-chloropyrimidin-4-yl)oxy)methyl)benzyl)-6-(2-(2-(2-aminoethoxy)ethoxy)acetamido)hexanamide (16) Compound **15** (40 mg, 54 μ mol) was dissolved in 2 ml of a mixture DBU/ACN 1:10 and stirred at room temperature for 45 min; then 300 μ l of glacial acetic acid were added to neutralize the base. After solvent evaporation the mixture was dissolved in 2 ml of DMSO, purified by preparative HPLC and lyophilized to give compound **16** (27 mg, 52 μ mol, 96%). [HRMS (ESI) calculated for $C_{24}H_{36}ClN_6O_5^+$ $[M+H]^+$ 523.2430; found 523.2447. 1H NMR (400 MHz, DMSO- d_6) δ 8.31 (t, 1 H, J = 5.9 Hz), 7.78 (s, 2 H), 7.75-7.72 (t, 1 H, J = 5.9 Hz), 7.39 (d, 2 H, J = 8.1 Hz), 7.25 (d, 2 H, J = 8.1 Hz), 7.11 (s, 2 H), 6.13 (s, 1 H), 5.29 (s, 2 H), 4.25 (d, 2 H, J = 5.9 Hz), 3.89 (s, 2 H), 3.62-3.59 (m, 4 H), 3.11-3.06 (m, 2 H), 3.01-2.97 (m, 2 H), 2.13 (t, 2 H, J = 7.4 Hz), 1.56-1.48 (m, 2 H), 1.46-1.39 (m, 2 H), 1.27-1.20 (m, 2 H)].



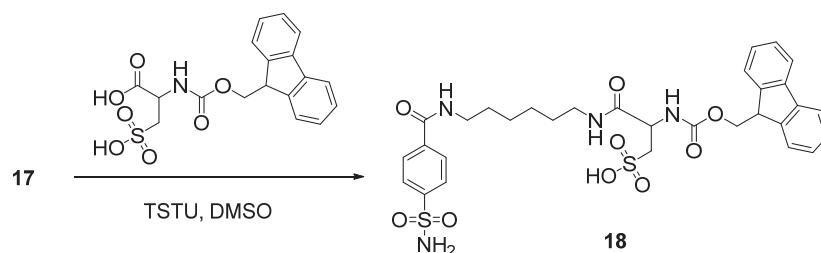
N-(1-(4-(((2-amino-6-chloropyrimidin-4-yl)oxy)methyl)phenyl)-3,10-dioxo-12,15-dioxo-2,9-diazaheptadecan-17-yl)-3-sulfamoylbenzamide (4a) Compound **22** (23 mg, 114 μ mol) was dissolved in 1.5 ml of DMSO; DIPEA (16 μ l, 92 μ mol), EDC·Cl (23 mg, 120 μ mol) and HOBt (13 mg, 92 μ mol) were then added, and the mixture was stirred during 3 min at room temperature. Compound **16** (48 mg, 92 μ mol) was added to the previous mixture and the stirring continued for other 60 min. The mixture was purified by preparative HPLC. The fractions containing the product were checked by HRMS (ESI) and lyophilized to give compound **4a** (15 mg, 21 μ mol, 23%). [HRMS (ESI) calculated for $C_{31}H_{41}ClN_7O_8S^+$ $[M+H]^+$ 706.2420; found 706.2430. 1H NMR (400 MHz, DMSO- d_6) δ 8.79 (t, 1 H, J = 5.6 Hz), 8.32 (t, 1 H, J = 1.6 Hz), 8.29 (t, 1 H, J = 5.9 Hz), 8.06 (ddd, 1 H, J = 7.8, 1.6, 1.1 Hz), 7.97 (ddd, 1 H, J = 7.8, 1.8, 1.0 Hz), 7.70-7.65 (m, 2 H), 7.45 (s, 2 H), 7.39 (d, 2 H, J = 8.3 Hz), 7.25 (d, 2 H, J = 8.3 Hz), 7.11 (s, 2 H), 6.14 (s, 1 H), 5.30 (s, 2 H), 4.26 (d, 2 H, J = 5.9 Hz), 3.87 (s, 2 H), 3.61-3.57 (m, 6 H), 3.47 (q, 2 H, J = 5.7 Hz), 3.10-3.05 (q, 2 H, J = 6.8 Hz), 2.12 (t, 2 H, J = 7.4 Hz), 1.55-1.48 (m, 2 H), 1.45-1.38 (m, 2 H), 1.26-1.19 (m, 2 H). ^{13}C NMR (151 MHz, DMSO- d_6) δ 172.5, 170.8, 169.4, 165.8, 163.3, 160.5, 146.7, 140.2, 137.7, 135.1, 128.9, 128.9, 128.3, 127.7, 126.1, 94.9, 70.7, 70.7, 69.8, 69.3, 67.7, 42.2, 40.9, 38.5, 35.7, 29.5, 26.6, 25.6.].



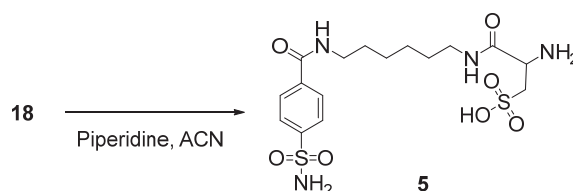
N-(1-(4-(((2-amino-6-chloropyrimidin-4-yl)oxy)methyl)phenyl)-3,10-dioxo-12,15-dioxo-2,9-diazaheptadecan-17-yl)-4-sulfamoylbenzamide (4b) 4-sulfamoylbenzoic acid (23 mg, 114 μmol) was dissolved in 1.5 ml of DMSO; DIPEA (16 μl , 92 μmol), EDC·Cl (23 mg, 120 μmol) and HOBT (13 mg, 92 μmol) were then added, and the mixture was stirred during 3 min at room temperature. Compound **16** (48 mg, 92 μmol) was added to the previous mixture and the stirring continued for other 60 min. The mixture was purified by preparative HPLC. The fractions containing the product were checked by HRMS (ESI) and lyophilized to give compound **4b** (11 mg, 16 μmol , 17%). [HRMS (ESI) calculated for $\text{C}_{31}\text{H}_{40}\text{ClN}_7\text{NaO}_8\text{S}^+$ $[\text{M}+\text{Na}]^+$ 728.2240; found 728.2248. ^1H NMR (400 MHz, DMSO-d_6) δ 8.73 (t, 1 H, $J = 5.5$ Hz), 8.29 (t, 1 H, $J = 5.9$ Hz), 8.00 (d, 2 H, $J = 8.5$ Hz), 7.91 (t, 2 H, $J = 8.5$ Hz), 7.66 (t, 1 H, $J = 5.9$ Hz), 7.49 (s, 2 H), 7.39 (d, 2 H, $J = 8.2$ Hz), 7.25 (d, 2 H, $J = 8.2$ Hz), 6.14 (s, 1 H), 5.30 (s, 2 H), 4.26 (d, 2 H, $J = 5.9$ Hz), 3.87 (s, 2 H), 3.61-3.57 (m, 6 H), 3.46 (q, 2 H, $J = 5.5$ Hz), 3.08 (q, 2 H, $J = 6.8$ Hz), 2.12 (t, 2 H, $J = 7.4$), 1.55-1.48 (m, 2 H), 1.45-1.38 (m, 2 H), 1.26-1.19 (m, 2 H). ^{13}C NMR (151 MHz, DMSO-d_6) δ 172.5, 170.8, 169.4, 165.6, 163.2, 160.5, 158.8, 158.6, 144.8, 140.2, 135.5, 135.1, 130.6, 129.6, 128.9, 128.6, 127.7, 125.2, 94.9, 70.7, 70.7, 70.4, 69.8, 69.3, 67.7, 42.2, 40.9, 38.5, 35.7, 29.5, 26.6, 25.5].



N-(6-aminohexyl)-4-sulfamoylbenzamide (17) 4-sulfamoylbenzoic acid (40 mg, 200 μmol) was dissolved in 2.5 ml of DMSO together with TSTU (72 mg, 240 μmol) and DIPEA (138 μl , 800 μmol); the mixture was stirred at room temperature for 30 min. Hexane-1,6-diamine (46 mg, 400 μmol) was then added and the reaction was left under stirring during 60 min at room temperature. 1 ml of H_2O and 500 μl of glacial acetic acid were added. The reaction mixture was purified by preparative HPLC and lyophilized to give the product **17** (58 mg, 195 μmol , 98%). [HRMS (ESI) calculated for $\text{C}_{13}\text{H}_{22}\text{N}_3\text{O}_3\text{S}^+$ $[\text{M}+\text{H}]^+$ 300.1376; found 300.1382. ^1H NMR (400 MHz, DMSO-d_6) δ 8.65 (t, 1 H, $J = 5.5$ Hz), 7.98 (d, 2 H, $J = 8.7$), 7.90 (d, 2 H, $J = 8.7$), 7.62 (s, 2 H), 7.49 (s, 2 H), 3.28 (q, 2 H, $J = 6.8$ Hz), 2.78 (t, 2 H, $J = 7.4$ Hz), 1.58-1.50 (m, 4 H), 1.36-1.31 (m, 4 H).].



2-(((9H-fluoren-9-yl)methoxy)carbonyl)amino)-3-oxo-3-((6-(4-sulfamoylbenzamido)hexyl)amino)propane-1-sulfonic acid (18) (((9H-fluoren-9-yl)methoxy)carbonyl)(sulfo)alanine (16 mg, 41 μmol) was dissolved in 1.5 ml of DMSO together with TSTU (13 mg, 43 μmol) and DIPEA (19 μl , 110 μmol); the mixture was stirred at room temperature for 30 min. Compound **17** (11 mg, 37 μmol) was then added and the reaction was left under stirring during 60 min at room temperature. 100 μl of glacial acetic acid were added. The reaction mixture was purified by preparative HPLC and lyophilized to give the product **18** (22 mg, 33 μmol , 80%). [HRMS (ESI) calculated for $\text{C}_{31}\text{H}_{36}\text{N}_4\text{NaO}_9\text{S}_2^+$ $[\text{M}+\text{Na}]^+$ 695.1816; found 695.1825. ^1H NMR (400 MHz, MeOD) δ 8.00-7.95 (m, 4 H), 7.80 (d, 2 H, J = 7.4 Hz), 7.71-7.69 (m, 2 H), 7.42-7.38 (m, 2 H), 7.35-7.31 (m, 2 H), 4.50 (dd, 1 H, J = 7.8, 4.8 Hz), 4.38-4.31 (m, 2 H), 4.26 (q, 1 H, J = 6.9 Hz), 3.26-3.20 (m, 3 H), 1.65-1.59 (m, 2 H), 1.59-1.52 (m, 2 H), 1.44-1.38 (m, 4 H)].



2-amino-3-oxo-3-((6-(4-sulfamoylbenzamido)hexyl)amino)propane-1-sulfonic acid (5) Compound **18** (22 mg, 33 μmol) was dissolved in 2 ml of a mixture piperidine/ACN 1:10 and stirred at room temperature for 30 min. After solvent and piperidine evaporation, the solid was washed 3 times with portions of 4 ml of ACN. The solid was then dissolved in 2 ml of DMSO, purified by preparative HPLC and lyophilized to give compound **5** (3 mg, 7 μmol , 21%). [HRMS (ESI) calculated for $\text{C}_{16}\text{H}_{26}\text{N}_4\text{NaO}_7\text{S}_2^+$ $[\text{M}+\text{Na}]^+$ 473.1135; found 473.1138. ^1H NMR (600 MHz, MeOD) δ 8.01-7.96 (m, 4 H), 4.21 (dd, 1 H, J = 3.4, 10.0 Hz), 3.42 (t, 2 H, J = 7.1 Hz), 3.29-3.28 (m, 1 H), 3.27-3.26 (m, 2 H), 3.15 (dd, 1 H, J = 14.5, 10.0 Hz), 1.69-1.65 (m, 2 H), 1.61-1.56 (m, 2 H), 1.44 (m, 2 H). ^{13}C NMR (151 MHz, MeOD) δ 167.4, 166.9, 146.3, 137.8, 127.5, 125.9, 50.5, 50.4, 39.5, 39.3, 28.9, 28.7, 26.2.].

6.2 Biology

6.2.1 Cloning

The vectors pET-51b(+) encoding for either SNAP-YPet-P₁₅(GGS)₂P₁₅-CFP-HCA or SNAP-CLIP were kindly provided by Dr. Rudolf Griss (Laboratory of Protein Engineering, EPFL); the pEBTet vector¹³¹ encoding for HDM2 was a kind gift from Dr. Grazvydas Lukinavicius (Laboratory of Protein Engineering, EPFL). DNA primers and oligos were provided by Microsynth. QIAquick Gel Extraction Kits, QIAprep Spin Miniprep Kits and Qiagen Plasmid Midi Kit were purchased from Qiagen. All the polymerase chain reactions (PCRs) were per-

formed using KOD Hot Start Polymerase (Novagen). Restriction enzymes, antarctic phosphatase, ligases and polymerases were purchased from New England Biolabs (NEB) and Thermo Fischer.

The assembly of vectors and PCR products was performed either by classical restriction/ligation techniques or using the Gibson Assembly¹³² Master Mix prepared in house. All the cloning steps were performed following the manufacturer protocols.

6.2.1.1 Amino acid sequence of the HCA-based sensor

MAS^{purple}W^{red}SH^{orange}P^{dark blue}Q^{light blue}FE^{green}K^{green}GADDDDKVP^{red}MDKDC^{orange}EMKRTTLD^{orange}SPLGKLELSGCEQGLHEIIFLGKGTSAADAVEVPAPAAVLGGPEPLMQATAWLNAYFHQPEAIEEFVVPALHHPVFQQESFTRQVLWKLKLVVKFGEVISYSHLAALAGNPAATAAVKTALSGNPVPIPIPCHRVVQGDLDVGGYEGGLAVKEWLLAHEGHRLGKPG^{orange}LG^{orange}TS^{orange}MSKGEELFTGVVPILVELDGDVNGHKFSVSGEGEGDATYGKLTLLCTTGKLPVPWP^{orange}TLVTTLGYGVQCFARYPDHMKQHDFFKSAMPEGYVQERTIFFKDDGNYKTRAEVKFEGDTLVNRIELKGIDFKEDGNILGHKLEYN^{orange}YN^{orange}SHNVYITADKQKNGIKANFKIRHNI^{orange}EDGGVQLADHYQQNTPIGDGPVLLPDNHYLSYQSALFKDPNEKRDHMLLEFLTAAGITEGMNELY^{orange}KE^{orange}FP^{dark blue}PPPPPPPPPPPPPPPGSGGS^{dark blue}PPPPPPPPPPPPPPPGGRMVSKGEELFTGVVPILVELDGDVNGHRFSVSGEGEGDATYGKLT^{dark blue}LFICTTGKLPVPWP^{dark blue}TLVTTLTWGVQCFSRYPDHMKQHDFFKSAMPEGYVQERTIFFKDDGNYKTRAEVKFEGDTLVNRIELKGIDFKEDGNILGHKLEYNYISHNVYITADKQKNGIKAHFKIRHNIEDGSVQLADHYQQNTPIGDGPVLLPDNHYLSTQSALSKDPNEKRDHMLLEFVTAATSAGGMSHHWGYGKHNGPEHWHKDFPIAKGERQSPVDIDTHTAKYDPSLKPLSVSYDQATSLRILNNGHAFNVEFDDSDQKAVLKGGLDGTYRLIQHFHWGSLDGQSEHTVDKKKYAAELHLVHWNTKYGDFGKAVQQPDGLAVLGIFLKVGSAPGLQKVVDVLDSIKTKGKSADFTNFDPRGLLPESLDYWTYPGSLTTPPLECWTWIVLKEPISVSSEQVLKFRKLNFN^{green}GE^{green}PEELMVDNWRPAQPLKNRQIKASFKRAPGFSSISA^{purple}HHHHHHHHHHH

^{purple}: Strep-tag II, His₁₀-tag for protein purification

^{red}: SNAP-tag

^{orange}: YPet

^{dark blue}: polyproline-(GGG)₂-polyproline linker

^{light blue}: CFP

^{green}: HCAII

6.2.1.2 Amino acid sequence of the p53-based sensor

MA^{purple}W^{red}SH^{orange}P^{dark blue}Q^{light blue}FE^{green}K^{green}GADDDDKVP^{red}S^{orange}QET^{orange}FDLWKLLEN^{red}ST^{orange}MSKGEELFTGVVPILVELDGDVNGHKFSVSGEGEGDATYGKLTLLCTTGKLPVPWP^{orange}TLVTTLGYGVQCFARYPDHMKQHDFFKSAMPEGYVQERTIFFKDDGNYKTRAEVKFEGDTLVNRIELKGIDFKEDGNILGHKLEYN^{orange}YN^{orange}SHNVYITADKQKNGIKANFKIRHNIEDGGVQLADHYQQNTPIGDGPVLLPDNHYLSYQSALFKDPNEKRDHMLLEFLTAAGITEGMNELY^{orange}KE^{orange}FP^{dark blue}PPPPPPPPPPPPPPPGSGGS^{dark blue}PPPPPPPPPPPPPPPPPGGRMVSKGEELFTGVVPILVELDGDVNGHRFSVSGEGEGDATYGKLT^{dark blue}LFICTTGKLPVPWP^{dark blue}TLVTTLTWGVQCFSRYPDHMKQHDFFKSAMPEGYVQERTIFFKDDGNYKTRAEVKFEGDTLVNRIELKGIDFKEDGNILGHKLEYNYISHNVYITADKQKNGIKAHFKIRHNIEDGSVQLADHYQQNTPIGDGPVLLPDNHYLSTQSALSKDPNEKRDHMLLEFVTAATSMCNTNMSVPTDGAVTTSQIPASEQETLVRPKPLLLKLLKSVGAQKDTYTMKEVLGYLQYIMTKRLYDEKQQHIVYCSNDLLGLFGVPSFSVKEHRKIYTM^{green}IYRN^{green}LVVN^{green}Q^{green}QESSDSGTSVSEN^{green}RAPGFSSISA^{purple}HHHHHHHHHHH

^{purple}: Strep-tag II, His₁₀-tag for protein purification

^{red}: p53 (15-29) fragment

^{orange}: YPet

dark blue: polyproline-(GGS)₂-polyproline linker

light blue: CFP

green: HDM2 (1-125) fragment

6.2.1.3 Amino acid sequence of the SNAP-CLIP

MAS^{dark blue}WSHPQFEK^{light blue}GADDDDKVPH^{dark blue}MDKDCEMKRTTLDSP^{light blue}LGKLELSGCEQGLHEIIFLGKGTSA
ADAVEVPAPAAVLGGPEPLMQATAWLNAYFHQPEAIEEFVVPALHHPVFQQESFTRQVLWKLL
KVVKFGEVISYSHLAALAGNPAATAAVKTALSGNPVPIIPCHR^{green}VVQGDLDVGGYEGGLAVKE
WLLAHEGHRLGK^{green}PGLG^{green}GRLEVL^{green}FQGP^{green}KA^{green}FLEMDKDCEMKRTTLDSP^{light blue}LGKLELSGCEQGLHK
IIFLGKGTSAADAVEVPAPAAVLGGPEPLIQATAWLNAYFHQPEAIEEFVVPALHHPVFQQESFT
RQVLWKLLKVVKFGEVISESHLAALVG^{green}NPAATAAVNTALDGNP^{green}VPIIPCHR^{green}VVQGDSDVGPYL
GGLAVKEWLLAHEGHRLGK^{green}PGLG^{green}GAPGFSSISA^{purple}HHHHHHHHHH

^{purple}: Strep-tag II, His₁₀-tag for protein purification

^{red}: SNAP-tag

^{green}: HDM2 (1-125) fragment

6.2.2 Sensor expression and purification from HEK293 EBNA1 cells

Phosphate buffered saline (PBS), FreeStyle 293 medium and PageRuler Prestained Protein Ladder 10-170KDa were purchased from Life Technologies. ExCell 293 medium, RPMI 1640 medium with 0.1% pluronic F68 were purchased from SAFC Biosciences. Doxycycline hydrochloride, polyethylenimine and CellLytic M were purchased from Sigma. EDTA-free protease inhibitor cocktail tablets were purchased from Roche, Strep-Tactin Superflow columns were bought from IBA, Ni-NTA Agarose was purchased from Macherey-Nagel and centrifugal filters for protein concentration were purchased from Millipore. Cell incubators were set at 37°C, 5% v/v CO₂, shaking speed 120 rpm, unless otherwise indicated. The concentration of protein solutions was measured with Nanodrop provided by Thermofisher.

Suspension-adapted HEK293 EBNA1 cells were routinely maintained in serum-free ExCell 293 medium with 4 mM glutamine. On the day before transfection, cells were inoculated into fresh medium at a density of 1·10⁶ cells/ml. The next day, 1·10⁹ cells were harvested by centrifugation (1200 rpm, 5 min) and resuspended at a density of 20·10⁶ cells in 50 ml of RPMI 1640 medium prewarmed at 37°C and supplemented with 0.1% pluronic F-68. Then 1.5 mg of plasmid DNA and 3 mg, 1 mg/ml in H₂O of linear polyethyleneimine were added and mixed. The cells were incubated under orbital shaking at 180 rpm. After 1 hour the transfected culture was transferred to a 5L glass bottle containing 950 ml of prewarmed FreeStyle 293 medium with 4 mM glutamine. The culture was transferred to an incubator shaker with agitation at 120 rpm for one day. After this time, doxycycline 1 µg/ml was added for expression enhancement, and the cells were incubated for 4 more days.

The cells were then pelleted (800 rpm, 5 min) and washed three times with 100 ml of PBS. The cell pellet was then resuspended in 40 ml of CellLytic M precooled to 4°C and supplemented with EDTA-free protease inhibitor cocktail and imidazole 5 mM. The solution was incubated at 4°C for 20 min with mild shaking; the cells debris were harvested by centrifugation, and the sensor protein contained in the supernatant was purified using a Ni-NTA column followed by a Strep-Tactin column according the suppliers' instructions. The resulting protein solution was concentrated on a centrifugal filter 50 KDa cutoff and the protein concentration was calculated based on the extinction coefficient of YPet (ϵ_{517} =

104000). The protein was stocked in 50% glycerol at -20°C and its mass was checked by electrophoresis.

6.2.3 Determination of the HCA sensor labeling kinetics *in vitro*

Bovine serum albumin (BSA) heat shock fraction was purchased from Sigma; SNAP-Cell TMR-Star was purchased from New England Biolabs (NEB).

A solution of the HCA-based sensor 1 μM and substrate of interest 4 μM in 50 mM HEPES pH=7.2, 50 mM NaCl, BSA 0.5 mg/ml was prepared. At different time points an aliquot of the sensor solution was mixed 1:2 with a solution of TMR-Star 50 μM freshly prepared. An aliquot of sensor without any substrate was also prepared and mixed in the same way with TMR-Star. The aliquots were then loaded on a gel for electrophoresis and for each band the fluorescence in the TMR channel was quantified and inversely related to the degree of the sensor labelling with the substrate of interest. The quantification of the TMR-fluorescence intensity was performed using the software ImageJ: the integrated intensity of the rectangular selection around each band was compared to the one of the unlabelled sensor aliquot (0% labelling). Therefore, the higher the labelling degree, the weaker the TMR-fluorescence intensity of the band. The final results summarized in Figure 3:6 are presented as average of three independent measurements followed by standard deviation.

6.2.4 Titration of analytes *in vitro*

Black, non-binding, flat bottom 96-well plates were purchased from Greiner Bio-One, centrifugal filters Amicon Ultra were purchased from Millipore. Fluorescence measurements were performed using an Infinite M1000 spectrofluorometer Tecan.

The labelling HCA-based sensor was performed by adding it 1 μM to a solution of BG or CP substrates 4 μM in 50 mM HEPES pH=7.2, 50 mM NaCl, 0.5 mg/ml BSA; the mixture was then incubated for 1 hour at room temperature. The p53-based sensor did not require labelling. The inhibitors of the p53-HDM2 interaction were provided by the industrial partner Dr. T. Vorherr (Director Peptide Discovery, Novartis Institute of BioMedical Research) as lyophilized and salt-free powders, which were dissolved and stored as DMSO solutions. The concentration of the small molecules was calculated based on weight, the one of the peptides based on Trp and Tyr absorbance at 280 nm ($\epsilon_{280}(\text{Trp}) = 5690 \text{ M}^{-1}\text{cm}^{-1}$, $\epsilon_{280}(\text{Tyr}) = 1280 \text{ M}^{-1}\text{cm}^{-1}$)¹³³.

. In a 96-well plate the sensor protein was diluted down to 50 nM with 50 mM HEPES pH=7.2, 50 mM NaCl, 0.5 mg/ml BSA, 0.7% DMSO containing defined concentrations of analytes; for all analytes, in the well corresponding to the lowest concentration just pure DMSO was added. The solutions were incubated at room temperature for 1 hour before the fluorescence measurement. The excitation was carried out at 434 nm with a bandwidth of 15 nm and the spectra were recorded from 460 to 600 nm using a step size of 1 nm and bandwidth of 15 nm.

In accordance with the design principles, increasing concentrations of analytes resulted in a reduction of the emission intensity of YPet (527 nm) and in a growth of the emission intensity of CFP (476 nm). The values of C_{50} were determined by plotting the ratio of CFP emission (476 nm, bandwidth 3 nm) over YPet emission (527 nm, bandwidth 3 nm) against the analyte concentration and by fitting the data with a single-site binding isotherm as previously described⁴⁴:

$$R = R_{zero} + \frac{R_{sat} - R_{zero}}{1 + \frac{C_{50}}{[analyte]}}$$

R_{zero} represents the ratio in absence of analyte and R_{sat} represents the one at saturating concentration of analyte. The ratio change is defined as the ratio R_{sat} / R_{zero} or, if expressed in percent, $100 \cdot (R_{sat} - R_{zero}) / R_{zero}$. In the case of the titrations of 1CFY and sMTide CIS with the p53-based sensor the fitting was performed with the following binding isotherm containing the Hill's coefficient (n):

$$R = R_{zero} + \frac{R_{sat} - R_{zero}}{1 + (\frac{C_{50}}{[analyte]})^n}$$

The C_{50} value corresponds to the concentration of analyte at which the half maximal ratio change is reached. It should be noted that the C_{50} does not necessarily correspond to the K_D^{comp} , concentration at which the sensor molecules are half in the open and half in the closed state: this condition is reached when each single channel separately gets to 50 % of the maximum change. The values of K_D^{comp} were obtained by fitting the intensity ratio data with the following binding isotherm^{54, 79}:

$$R = \frac{I_{CFP-b}[analyte] + I_{CFP-u}[K_D^{comp}]}{I_{YPet-b}[analyte] + I_{YPet-u}[K_D^{comp}]}$$

where I_{CFP-b} and I_{CFP-u} represent the intensities at the CFP emission respectively of the analyte-bound and unbound sensor, I_{YPet-b} and I_{YPet-u} represent the intensities at the YPet emission respectively of the analyte-bound and unbound sensor, $[analyte]$ is the concentration of the corresponding analyte and K_D^{comp} is the dissociation constant. The fitting for the calculation of K_D^{comp} of 1CFY and sMTide CIS was modified to contain the Hill's coefficient:

$$R = \frac{I_{CFP-b}[analyte]^n + I_{CFP-u}[K_D^{comp}]^n}{I_{YPet-b}[analyte]^n + I_{YPet-u}[K_D^{comp}]^n}$$

The fluorescence intensities at the CFP and YPet emissions of the bound and unbound sensor were calculated by fitting the curves of intensity against concentration of analyte with the following isotherm:

$$I = I_u \frac{I_b - I_u}{1 + \frac{K_D'}{[analyte]}}$$

where I is the emission intensity of either the donor or the acceptor, I_b and I_u are the respective emission intensities for the analyte-bound and unbound sensor, $[analyte]$ is the concentration of analyte. In the case of the intensity curves obtained with 1CFY and sMTide CIS, the fitting was modified as follows:

$$I = I_u \frac{I_b - I_u}{1 + (\frac{K_D'}{[analyte]})^n}$$

The final results are presented as average of three independent measurements followed by standard deviation.

6.2.5 Determination of the sensor's opening kinetic *in vitro*

Fluorescence measurements were performed using an Infinite M1000 spectrofluorometer Tecan, which is equipped with an automatic injector. All kinetic experiments were performed at 37°C, unless otherwise indicated.

The protein sensor was diluted to 100 nM in 50 mM HEPES pH=7.2, 50 mM NaCl, 0.5 mg/ml BSA and mixed 1:2 with a solution of analyte of interest at time zero. An orbital-type mixing step of 3 seconds was introduced before the recording of the fluorescence emission intensities, in order to guarantee a good degree of homogeneity in the sensor-analyte solution. The excitation was carried out at 434 nm and the fluorescence emissions of CFP (476 ± 3 nm) and YPet (527 ± 3 nm) were recorded over time.

In accordance with the design principles, with the progressive binding of the analyte to the sensor resulted in a reduction of the emission intensity of YPet and in a growth of the emission intensity of CFP. The values of the sensor half-life of opening $t_{1/2}$ were determined by plotting the ratio of CFP emission over YPet emission against time and by fitting the data with a mono- (for the HCA-based sensor) or a bi-exponential (for the p53-based sensor) function:

$$R_{zero} = R_{sat} + (R_{zero} - R_{sat}) e^{\frac{-t}{t_{1/2}}}$$

$$R_{zero} = R_{sat} + (R_{zero} - R_{sat}) e^{\frac{-t}{t_{1/2}}} + A e^{\frac{-t}{t_{1/2}^2}}$$

R_{zero} represents the ratio at time zero, R_{sat} represents the ratio at saturation of the sensor. The value of the opening rate constant can be calculated from the value of $t_{1/2}$:

$$k = \frac{\ln 2}{t_{1/2}}$$

The final results summarized in Table 3:2 are presented as average of three (in the case of the HCA-based sensor) or two (in the case of the p53-based sensor) independent measurements followed by standard deviation.

6.2.6 Semi stable adherent cell line generation

Dubelcco's modified eagle medium (DMEM), fetal bovine serum (FBS), Hank's buffered salt solution (HBSS), GlutaMAX, trypsin-EDTA (0.05%) and puromycin dihydrochloride were purchased from Thermo Fisher. Tissue culture flasks were purchased from TPP and Lipofectamine 2000 by Invitrogen. Unless otherwise indicated, all cell lines were cultured in DMEM high glucose medium supplemented with 10% FBS and GlutaMAX; all semi-stable cell lines were cultured in DMEM high glucose medium supplemented with 10% FBS, GlutaMAX and puromycin at different concentrations depending on the cell type.

U2OS or HEK 293T cells were cultured on tissue culture flasks and splitted twice a week. The cells were transfected with pEBTet vectors using lipofectamine according to the provider's instructions. Starting from 24 hours after transfection the cells were cultured in

DMEM high glucose medium supplemented with 10% FBS and GlutaMAX and puromycin 1 or 3 $\mu\text{g/ml}$ respectively for U2OS and HEK 293T cells.

6.2.7 Determination of the cell permeability of SNAP-tag substrates

The CLIP-tag substrate BC-SiR was a kind gift of Dr. Luc Reymond (Laboratory of Protein Engineering, EPFL).

The U2OS semi-stable cell line expressing the protein SNAP-CLIP was seeded in 6-well cultured plates in presence of doxycycline 1 $\mu\text{g/ml}$. 24 hours later the cells were labelled by exchanging the medium with fresh one containing doxycycline 1 $\mu\text{g/ml}$ and, per well, a different substrate 5 μM . One well was left in the old medium, without labelling; in another the cells were labelled with SNAP-Cell Block, a non-fluorescent substrate that blocks the SNAP's active site. The cells were then incubated overnight. The following day the medium was substituted with fresh one containing TMR-Star 5 μM . The cells were incubated for 30 min, washed 3 times with HBSS, incubated for 20 min at 4°C with CellLytic supplemented with protease inhibitor cocktail and BC-SiR 5 μM . Aliquots of the lysate of each well were loaded in an electrophoresis gel. For each band the fluorescence in the TMR channel was quantified, normalized for the fluorescence in the SiR channel (normalization for the protein concentration in each lysate) and inversely related to the degree of the sensor labelling with the different substrates. The quantification of the TMR-fluorescence intensity was performed using the software ImageJ. The integrated intensity of the rectangular selection around each band in the TMR-channel was normalized by the one in the SiR-channel. The normalized values were then compared to the ones of the cells labelled with just TMR-Star (0% labelling) and SNAP-Cell Block (100% labelling): the higher the labelling degree, the weaker the TMR-fluorescence intensity of the band. The final results summarized in Figure 3:5 are presented as average of three independent measurements followed by standard deviation.

6.3 Microscopy

6.3.1 General information

Wide-field microscopy experiment were carried out with IN Cell Analyser 2200 from GE equipped with: a Nikon 20X objective, NA 0.75, Plan Apo, CFI/60; CFP excitation (438 nm, bandwidth 24 nm) and emission (475 nm, bandwidth 24 nm) filter and YFP emission filter (548 nm, bandwidth 22 nm) on QUAD 3 Polychroic mirror; plate and lid heater, CO₂ chamber. For each frame, two fluorescence emission images (CFP and FRET) were recorded consecutively with exposure time 100 ms, Binning 4X4, Laser Autofocus power level 10%, refocus at each time point during time-course experiments. All live cell imaging experiments were performed at 37°C, 5% v/v CO₂. Tissue culture treated 96-well plate, black, flat bottom with lid were purchased from Corning.

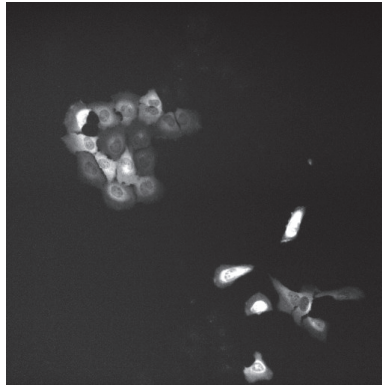


Figure 6:1 Example of microscopy image (YPet emission) of the U2OS cell line expressing the HCA-based sensor.

After recording, the images were analysed with the software Cell Profiler 2.1.1. The Analysis Modules list consisted in:

1. ImageMath, to sum CFP and FRET images;
2. Morph, to perform the operation Tophat with the structuring element Octagon;
3. IdentifyPrimaryObjects, to identify cells with A Global Threshold strategy, Background Thresholding Method;



Figure 6:2 Outline of the cells identified after the first image manipulation modules.

4. ExpandOrShrinkObjects, to expand cells of 5 pixels;



Figure 6:3 Outline of the 5 pixels-expanded cells.

5. IdentifySecondaryObjects, to identify as an object the region between the image borders and the cells identified in Module 3 expanded of 15 pixels;

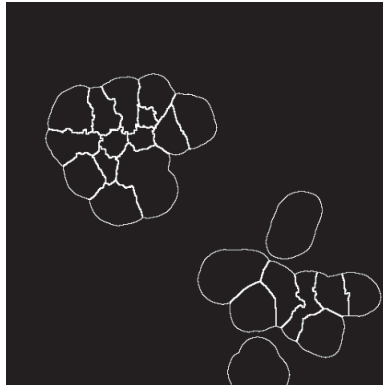


Figure 6:4 Outline of the 15 pixels-expanded cells.

6. IdentifyTertiaryObjects, to identify the background region as the difference between the image resulting from Module 5 and the expanded cells identified in Module 4;



Figure 6:5 Outline of the regions included between the 15 pixels and the 5 pixels-expanded cells.

7. RelateObjects, to relate each cell to its specific background;
8. TrackObjects, to track cells with an Overlap method;

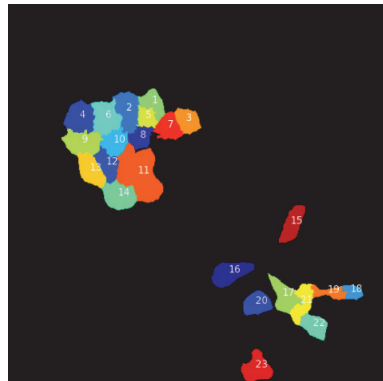


Figure 6:6 Assignment of an ID number to each cell.

9. MeasureObjectIntensity, to measure in the CFP and FRET images the average intensity of the regions identified in Module 3 and 6 (respectively cells and background);
10. ExportToSpreadsheet, to export the results of the measurement in an Excel file.

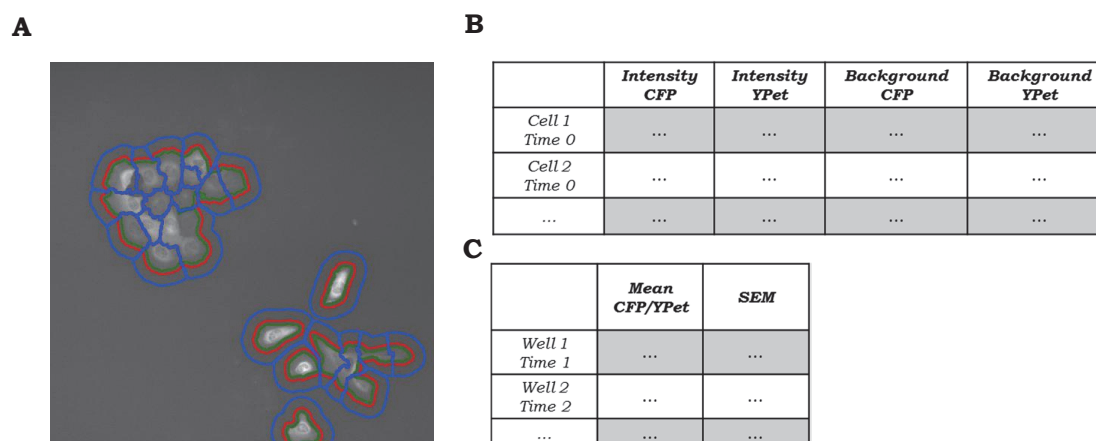


Figure 6:7 (A) Overlay of the outlines of the cells (green), the 5 pixels-expanded cells (red) and the 15 pixels-expanded cells (blue). As background, the region included between the red and the blue line was used. (B) Output table summarizing the average intensity values per cell and per time. (C) Output table of the mathematical analysis of the data collected in (B).

CFP and FRET intensity means and standard deviations of the mean for the cells treated in the same conditions were calculated and used for intensity ratio plots. The average number of cells per condition was above 100.

6.3.2 Titration of analytes *in cellulo*

The semi-stable U2OS cell line expressing a protein sensor was seeded in a 96-well plate in presence of doxycycline 1 µg/ml. If needed (for the HCA-based sensor), 24 hours later the cells were labelled by exchanging the medium with fresh one containing the substrate 5 µM and doxycycline 1 µg/ml. One day later the cells were washed 3 times with HBSS and incubated for 30 min after the last washing step. Then the cells were incubated with different dilutions of analytes in HBSS, 0.7% DMSO for 1 or 2 hours (the latter incubation time was used for peptides who have slower cellular uptake) and imaged. The final results are presented as average of two (for the p53-based sensor) or three (for the HCA-based sensor) independent measurements followed by standard deviation of the mean; at least 100 cells were tested per condition.

6.3.3 Cell entry and washout kinetics *in cellulo*

The semi-stable U2OS cell line expressing a protein sensor was seeded in a 96-well plate in presence of doxycycline 1 $\mu\text{g/ml}$. If needed (for the HCA-based sensor), 24 hours later the cells were labelled by exchanging the medium with fresh one containing the substrate 5 μM and doxycycline 1 $\mu\text{g/ml}$. One day later the cells were washed 3 times with HBSS and incubated for 30 min after the last washing step. The supernatant was then manually exchanged with a solution of analyte in HBSS, 0.7% DMSO and the time-course imaging was started, with a delay of 15 seconds between the addition of analyte and the first recorded frame. For washout experiments, the analyte solution over the cells was manually exchanged with fresh HBSS and the time-course imaging was restarted. The opening half-life values were calculated as average of two (for the p53-based sensor) or three (for the HCA-based sensor) independent measurements followed by standard deviation of the mean; at least 100 cells were tested per condition.

References

1. Luo, D. & Saltzman, W.M. Synthetic DNA delivery systems. *Nat Biotechnol* **18**, 33-37 (2000).
2. Jang, M., Kim, J.H., Nam, H.Y., Kwon, I.C. & Ahn, H.J. Design of a platform technology for systemic delivery of siRNA to tumours using rolling circle transcription. *Nat Commun* **6**, 7930 (2015).
3. Press, A.T. et al. Cell type-specific delivery of short interfering RNAs by dye-functionalised theranostic nanoparticles. *Nat Commun* **5**, 5565 (2014).
4. Morris, M.C., Depollier, J., Mery, J., Heitz, F. & Divita, G. A peptide carrier for the delivery of biologically active proteins into mammalian cells. *Nat Biotechnol* **19**, 1173-1176 (2001).
5. Erazo-Oliveras, A. et al. Protein delivery into live cells by incubation with an endosomolytic agent. *Nat Methods* **11**, 861-867 (2014).
6. Liu, B.R., Huang, Y.W., Winiarz, J.G., Chiang, H.J. & Lee, H.J. Intracellular delivery of quantum dots mediated by a histidine- and arginine-rich HR9 cell-penetrating peptide through the direct membrane translocation mechanism. *Biomaterials* **32**, 3520-3537 (2011).
7. Fu, Y. & Kraitchman, D.L. Stem cell labeling for noninvasive delivery and tracking in cardiovascular regenerative therapy. *Expert Rev Cardiovasc Ther* **8**, 1149-1160 (2010).
8. EFPIA The Pharmaceutical Industry in Figures, 2008 edition.
9. Kerns, E. Pharmaceutical profiling in drug discovery. *Drug Discovery Today* **8**, 316-323 (2003).
10. Kerns, E.H. & Di, L. in *Drug-like Properties: Concepts, Structure Design and Methods* 17-1 (Academic Press, San Diego; 2008).
11. Lipinski, C.A., Lombardo, F., Dominy, B.W. & Feeney, P.J. Experimental and computational approaches to estimate solubility and permeability in drug discovery and development settings. PII of original article: S0169-409X(96)00423-1. The article was originally published in *Advanced Drug Delivery Reviews* 23 (1997) 3-25.1. *Advanced Drug Delivery Reviews* **46**, 3-26 (2001).
12. Shah, V.P. & Amidon, G.L. A theoretical basis for a biopharmaceutic drug classification: the correlation of in vitro drug product dissolution and in vivo bioavailability. *AAPS J* **16**, 894-898 (2014).
13. Wang, J., Urban, L. The impact of early ADME profiling on drug discovery and development strategy. *Drug Discovery World*, 73-86 (Fall 2004).
14. Matsson, P., Doak, B.C., Over, B. & Kihlberg, J. Cell permeability beyond the rule of 5. *Adv Drug Deliv Rev* **101**, 42-61 (2016).
15. Flaten, G.E., Dhanikula, A.B., Luthman, K. & Brandl, M. Drug permeability across a phospholipid vesicle based barrier: a novel approach for studying passive diffusion. *Eur J Pharm Sci* **27**, 80-90 (2006).
16. Gomes, M.J. et al. A new approach for a blood-brain barrier model based on phospholipid vesicles: Membrane development and siRNA-loaded nanoparticles permeability. *Journal of Membrane Science* **503**, 8-15 (2016).
17. Taillardat-Bertschinger, A., Carrupt, P.A., Barbato, F. & Testa, B. Immobilized artificial membrane HPLC in drug research. *J Med Chem* **46**, 655-665 (2003).
18. Tsopelas, F., Vallianatou, T. & Tsantili-Kakoulidou, A. The potential of immobilized artificial membrane chromatography to predict human oral absorption. *Eur J Pharm Sci* **81**, 82-93 (2016).
19. Kansy, M., Senner, F. & Gubernator, K. Physicochemical high throughput screening: parallel artificial membrane permeation assay in the description of passive absorption processes. *J Med Chem* **41**, 1007-1010 (1998).

20. Kerns, E.H. & Di, L. in *Drug-like Properties: Concepts, Structure Design and Methods* 287-298 (Academic Press, San Diego; 2008).
21. Verma, R.P., Hansch, C. & Selassie, C.D. Comparative QSAR studies on PAMPA/modified PAMPA for high throughput profiling of drug absorption potential with respect to Caco-2 cells and human intestinal absorption. *J Comput Aided Mol Des* **21**, 3-22 (2007).
22. Avdeef, A. & Tsinman, O. PAMPA--a drug absorption in vitro model 13. Chemical selectivity due to membrane hydrogen bonding: in combo comparisons of HDM-, DOPC-, and DS-PAMPA models. *Eur J Pharm Sci* **28**, 43-50 (2006).
23. Sugano, K., Hamada, H., Machida, M. & Ushio, H. High Throughput Prediction of Oral Absorption: Improvement of the Composition of the Lipid Solution Used in Parallel Artificial Membrane Permeation Assay. *Journal of Biomolecular Screening* **6**, 189-196 (2001).
24. Kerns, E.H. & Di, L. in *Drug-like Properties: Concepts, Structure Design and Methods* 86-99 (Academic Press, San Diego; 2008).
25. Buckley, S.T., Fischer, S.M., Fricker, G. & Brandl, M. In vitro models to evaluate the permeability of poorly soluble drug entities: challenges and perspectives. *Eur J Pharm Sci* **45**, 235-250 (2012).
26. Sugano, K. et al. Coexistence of passive and carrier-mediated processes in drug transport. *Nat Rev Drug Discov* **9**, 597-614 (2010).
27. Irvine, J.D. et al. MDCK (Madin-Darby canine kidney) cells: A tool for membrane permeability screening. *J Pharm Sci* **88**, 28-33 (1999).
28. Braun, A. et al. Cell cultures as tools in biopharmacy. *European Journal of Pharmaceutical Sciences* **11**, S51-S60 (2000).
29. Zhang, Y. & Yu, L.C. Single-cell microinjection technology in cell biology. *Bioessays* **30**, 606-610 (2008).
30. Luft, C. & Ketteler, R. Electroporation Knows No Boundaries: The Use of Electrostimulation for siRNA Delivery in Cells and Tissues. *J Biomol Screen* **20**, 932-942 (2015).
31. Escoffre, J.-M. & Bouakaz, A. Therapeutic Ultrasounds. *Advances in Experimental Medicine and Biology* **880**, 175-189 (2016).
32. Klein, T.M., Wolf, E.D., Wu, R. & Sanford, J.C. High-velocity microprojectiles for delivering nucleic acids into living cells. *Nature* **327**, 70-73 (1987).
33. Sherazee, N. & Alvarez, V.A. DiOlistics: delivery of fluorescent dyes into cells. *Methods Mol Biol* **940**, 391-400 (2013).
34. Scheiblhofer, S., Ritter, U., Thalhamer, J. & Weiss, R. Protein antigen delivery by gene gun-mediated epidermal antigen incorporation (EAI). *Methods Mol Biol* **940**, 401-411 (2013).
35. Webster, A., Coupland, P., Houghton, F.D., Leese, H.J. & Aylott, J.W. The delivery of PEBBLE nanosensors to measure the intracellular environment. *Biochem Soc Trans* **35**, 538-543 (2007).
36. Pandey, A.P. & Sawant, K.K. Polyethylenimine: A versatile, multifunctional non-viral vector for nucleic acid delivery. *Mater Sci Eng C Mater Biol Appl* **68**, 904-918 (2016).
37. Vitiello, G. et al. Cationic liposomes as efficient nanocarriers for the drug delivery of an anticancer cholesterol-based ruthenium complex. *J. Mater. Chem. B* **3**, 3011-3023 (2015).
38. Tortorella, S. & Karagiannis, T.C. Transferrin receptor-mediated endocytosis: a useful target for cancer therapy. *J Membr Biol* **247**, 291-307 (2014).
39. Zhan, C., Li, C., Wei, X., Lu, W. & Lu, W. Toxins and derivatives in molecular pharmaceuticals: Drug delivery and targeted therapy. *Adv Drug Deliv Rev* **90**, 101-118 (2015).
40. Ramsey, J.D. & Flynn, N.H. Cell-penetrating peptides transport therapeutics into cells. *Pharmacol Ther* **154**, 78-86 (2015).
41. Henriques, S.T., Melo, M.N. & Castanho, M.A. Cell-penetrating peptides and antimicrobial peptides: how different are they? *Biochem J* **399**, 1-7 (2006).

42. Bechara, C. & Sagan, S. Cell-penetrating peptides: 20 years later, where do we stand? *FEBS Lett* **587**, 1693-1702 (2013).
43. Hochreiter, B., Garcia, A.P. & Schmid, J.A. Fluorescent proteins as genetically encoded FRET biosensors in life sciences. *Sensors (Basel)* **15**, 26281-26314 (2015).
44. Brun, M.A., Tan, K.T., Nakata, E., Hinner, M.J. & Johnsson, K. Semisynthetic fluorescent sensor proteins based on self-labeling protein tags. *J Am Chem Soc* **131**, 5873-5884 (2009).
45. Keppler, A. et al. A general method for the covalent labeling of fusion proteins with small molecules in vivo. *Nat Biotechnol* **21**, 86-89 (2003).
46. Juillerat, A. et al. Directed evolution of O6-alkylguanine-DNA alkyltransferase for efficient labeling of fusion proteins with small molecules in vivo. *Chem Biol* **10**, 313-317 (2003).
47. Gautier, A. et al. An engineered protein tag for multiprotein labeling in living cells. *Chem Biol* **15**, 128-136 (2008).
48. Reymond, L. et al. Visualizing biochemical activities in living cells through chemistry. *Chimia (Aarau)* **65**, 868-871 (2011).
49. Lukinavicius, G., Reymond, L. & Johnsson, K. Fluorescent labeling of SNAP-tagged proteins in cells. *Methods Mol Biol* **1266**, 107-118 (2015).
50. Brun, M.A. et al. Semisynthesis of fluorescent metabolite sensors on cell surfaces. *J Am Chem Soc* **133**, 16235-16242 (2011).
51. Masharina, A., Reymond, L., Maurel, D., Umezawa, K. & Johnsson, K. A fluorescent sensor for GABA and synthetic GABA(B) receptor ligands. *J Am Chem Soc* **134**, 19026-19034 (2012).
52. Brun, M.A. et al. A semisynthetic fluorescent sensor protein for glutamate. *J Am Chem Soc* **134**, 7676-7678 (2012).
53. Schena, A. & Johnsson, K. Sensing acetylcholine and anticholinesterase compounds. *Angew Chem Int Ed Engl* **53**, 1302-1305 (2014).
54. Xue, L., Prifti, E. & Johnsson, K. A General Strategy for the Semisynthesis of Ratiometric Fluorescent Sensor Proteins with Increased Dynamic Range. *J Am Chem Soc* **138**, 5258-5261 (2016).
55. Frommer, W.B., Davidson, M.W. & Campbell, R.E. Genetically encoded biosensors based on engineered fluorescent proteins. *Chem Soc Rev* **38**, 2833-2841 (2009).
56. Wang, S., Zhao, Y., Bernard, D., Aguilar, A. & Kumar, S. Targeting the MDM2-p53 Protein-Protein Interaction for New Cancer Therapeutics. **8**, 57-79 (2012).
57. Krishnamurthy, V.M. et al. Carbonic anhydrase as a model for biophysical and physical-organic studies of proteins and protein-ligand binding. *Chem Rev* **108**, 946-1051 (2008).
58. Innocenti, A. et al. Carbonic anhydrase inhibitors. Inhibition of the membrane-bound human and bovine isozymes IV with sulfonamides. *Bioorg Med Chem Lett* **15**, 1149-1154 (2005).
59. Esbaugh, A.J. & Tufts, B.L. The structure and function of carbonic anhydrase isozymes in the respiratory system of vertebrates. *Respir Physiol Neurobiol* **154**, 185-198 (2006).
60. Supuran, C.T. Carbonic anhydrases: novel therapeutic applications for inhibitors and activators. *Nat Rev Drug Discov* **7**, 168-181 (2008).
61. Supuran, C.T. & Scozzafava, A. Carbonic anhydrases as targets for medicinal chemistry. *Bioorg Med Chem* **15**, 4336-4350 (2007).
62. Fisher, S.Z. et al. Neutron structure of human carbonic anhydrase II: implications for proton transfer. *Biochemistry* **49**, 415-421 (2010).
63. Supuran, C.T. & Scozzafava, A. Applications of carbonic anhydrase inhibitors and activators in therapy. *Expert Opinion on Therapeutic Patents* **12**, 217-242 (2005).
64. Ozawa, Y. et al. Therapeutic potential and molecular mechanism of a novel sulfonamide anticancer drug, indisulam (E7070) in combination with CPT-11 for cancer treatment. *Cancer Chemother Pharmacol* **69**, 1353-1362 (2012).

65. Dvorak, M.M. et al. Thiazide diuretics directly induce osteoblast differentiation and mineralized nodule formation by interacting with a sodium chloride co-transporter in bone. *J Am Soc Nephrol* **18**, 2509-2516 (2007).
66. Tan, K.-T., Brun, M., Griss, R., Reymond, L. & Johnsson, K. Unpublished Material.
67. Lavis, L.D. & Raines, R.T. Bright ideas for chemical biology. *ACS Chem Biol* **3**, 142-155 (2008).
68. Dye, B.T. Flow cytometric analysis of CFP-YFP FRET as a marker for in vivo protein-protein interaction. *Clinical and Applied Immunology Reviews* **5**, 307-324 (2005).
69. Kremers, G.J., Goedhart, J., van Munster, E.B. & Gadella, T.W., Jr. Cyan and yellow super fluorescent proteins with improved brightness, protein folding, and FRET Forster radius. *Biochemistry* **45**, 6570-6580 (2006).
70. Lindenburg, L.H. et al. Quantifying stickiness: thermodynamic characterization of intramolecular domain interactions to guide the design of forster resonance energy transfer sensors. *Biochemistry* **53**, 6370-6381 (2014).
71. Evers, T.H., van Dongen, E.M., Faesen, A.C., Meijer, E.W. & Merkx, M. Quantitative understanding of the energy transfer between fluorescent proteins connected via flexible peptide linkers. *Biochemistry* **45**, 13183-13192 (2006).
72. Reddy Chichili, V.P., Kumar, V. & Sivaraman, J. Linkers in the structural biology of protein-protein interactions. *Protein Sci* **22**, 153-167 (2013).
73. Arora, P.S., Ansari, A.Z., Best, T.P., Ptashne, M. & Dervan, P.B. Design of Artificial Transcriptional Activators with Rigid Poly-l-proline Linkers. *Journal of the American Chemical Society* **124**, 13067-13071 (2002).
74. Chen, X., Zaro, J.L. & Shen, W.C. Fusion protein linkers: property, design and functionality. *Adv Drug Deliv Rev* **65**, 1357-1369 (2013).
75. Daniels, D.S. et al. Active and alkylated human AGT structures: a novel zinc site, inhibitor and extrahelical base binding. *EMBO J* **19**, 1719-1730 (2000).
76. Correa, I. et al. Substrates for Improved Live-Cell Fluorescence Labeling of SNAP-tag. *Current Pharmaceutical Design* **19**, 5414-5420 (2013).
77. Barrese, A.A.I. High-Throughput Screening Studies of Inhibition of Human Carbonic Anhydrase II and Bacterial Flagella Antimicrobial Activity. *Western Michigan University Dissertations Paper* **500** (2010).
78. Krishnamurthy, V.M., Semetey, V., Bracher, P.J., Shen, N. & Whitesides, G.M. Dependence of effective molarity on linker length for an intramolecular protein-ligand system. *J Am Chem Soc* **129**, 1312-1320 (2007).
79. Pomorski, A., Kochanczyk, T., Miloch, A. & Krezel, A. Method for accurate determination of dissociation constants of optical ratiometric systems: chemical probes, genetically encoded sensors, and interacting molecules. *Anal Chem* **85**, 11479-11486 (2013).
80. Enami, S., Hoffmann, M.R. & Colussi, A.J. Ozone oxidizes glutathione to a sulfonic acid. *Chem Res Toxicol* **22**, 35-40 (2009).
81. Kuznetsova, I.M., Turoverov, K.K. & Uversky, V.N. What macromolecular crowding can do to a protein. *Int J Mol Sci* **15**, 23090-23140 (2014).
82. Ettinger, A. & Wittmann, T. Fluorescence live cell imaging. *Methods Cell Biol* **123**, 77-94 (2014).
83. Waters, J.C. Accuracy and precision in quantitative fluorescence microscopy. *J Cell Biol* **185**, 1135-1148 (2009).
84. Maren, T.H. Direct measurements of the rate constants of sulfonamides with carbonic anhydrase. *Molecular Pharmacology* **41**, 419-426 (1992).
85. Granero, G.E. et al. Biowaiver monographs for immediate release solid oral dosage forms: acetazolamide. *J Pharm Sci* **97**, 3691-3699 (2008).
86. DrugBank Acetazolamide.
87. DrugBank Methazolamide.
88. Søreide, J.A., Lea, O.A. & Kvinnsland, S. Cytosol Albumin Content in Operable Breast Cancer Correlations to Steroid Hormone Receptors, Other Prognostic Factors and Prognosis. *Acta Oncologica* **30**, 797-802 (1991).

89. Milo, R. What is the total number of protein molecules per cell volume? A call to rethink some published values. *Bioessays* **35**, 1050-1055 (2013).
90. Bhardwaj, N. & Lu, H. Correlation between gene expression profiles and protein-protein interactions within and across genomes. *Bioinformatics* **21**, 2730-2738 (2005).
91. Braun, P. & Gingras, A.C. History of protein-protein interactions: from egg-white to complex networks. *Proteomics* **12**, 1478-1498 (2012).
92. Lage, K. Protein-protein interactions and genetic diseases: The interactome. *Biochim Biophys Acta* **1842**, 1971-1980 (2014).
93. Ryan, D.P. & Matthews, J.M. Protein-protein interactions in human disease. *Curr Opin Struct Biol* **15**, 441-446 (2005).
94. Wells, J.A. & McClendon, C.L. Reaching for high-hanging fruit in drug discovery at protein-protein interfaces. *Nature* **450**, 1001-1009 (2007).
95. Moreira, I.S., Fernandes, P.A. & Ramos, M.J. Hot spots--a review of the protein-protein interface determinant amino-acid residues. *Proteins* **68**, 803-812 (2007).
96. Arkin, M.R., Tang, Y. & Wells, J.A. Small-molecule inhibitors of protein-protein interactions: progressing toward the reality. *Chem Biol* **21**, 1102-1114 (2014).
97. Bullock, B.N., Jochim, A.L. & Arora, P.S. Assessing helical protein interfaces for inhibitor design. *J Am Chem Soc* **133**, 14220-14223 (2011).
98. Jamieson, A. & Robertson, N. Regulation of protein-protein interactions using stapled peptides. *Reports in Organic Chemistry*, 65 (2015).
99. Kawamoto, S.A. et al. Design of triazole-stapled BCL9 alpha-helical peptides to target the beta-catenin/B-cell CLL/lymphoma 9 (BCL9) protein-protein interaction. *J Med Chem* **55**, 1137-1146 (2012).
100. Jackson, D.Y., King, D.S., Chmielewski, J., Singh, S. & Schultz, P.G. General approach to the synthesis of short .alpha.-helical peptides. *Journal of the American Chemical Society* **113**, 9391-9392 (1991).
101. Phelan, J.C., Skelton, N.J., Braisted, A.C. & McDowell, R.S. A General Method for Constraining Short Peptides to an α -Helical Conformation. *Journal of the American Chemical Society* **119**, 455-460 (1997).
102. Verdine, G.L. & Hilinski, G.J. Stapled peptides for intracellular drug targets. *Methods Enzymol* **503**, 3-33 (2012).
103. Walensky, L.D. & Bird, G.H. Hydrocarbon-stapled peptides: principles, practice, and progress. *J Med Chem* **57**, 6275-6288 (2014).
104. Chu, Q. et al. Towards understanding cell penetration by stapled peptides. *Med. Chem. Commun.* **6**, 111-119 (2015).
105. Sawyer, T.K. AILERON Therapeutics. *Chem Biol Drug Des* **73**, 3-6 (2009).
106. Liang, Y., Liu, J. & Feng, Z. The regulation of cellular metabolism by tumor suppressor p53. *Cell Biosci* **3**, 9 (2013).
107. Sionov, R.V. & Haupt, Y. The cellular response to p53: the decision between life and death. *Oncogene* **18**, 6145-6157 (1999).
108. Hollstein, M., Sidransky, D., Vogelstein, B. & Harris, C. p53 mutations in human cancers. *Science* **253**, 49-53 (1991).
109. Burgess, A. et al. Clinical Overview of MDM2/X-Targeted Therapies. *Front Oncol* **6**, 7 (2016).
110. Lu, X. Tied up in loops: positive and negative autoregulation of p53. *Cold Spring Harb Perspect Biol* **2**, a000984 (2010).
111. Wu, X., Bayle, J.H., Olson, D. & Levine, A.J. The p53-mdm-2 autoregulatory feedback loop. *Genes Dev* **7**, 1126-1132 (1993).
112. Nag, S. et al. Targeting MDM2-p53 Interaction for Cancer Therapy: Are We There Yet? *Current Medicinal Chemistry* **21**, 553-574 (2014).
113. Roth, J., Dobbelsstein, M., Freedman, D.A., Shenk, T. & Levine, A.J. Nucleocytoplasmic shuttling of the hdm2 oncoprotein regulates the levels of the p53 protein via a pathway used by the human immunodeficiency virus rev protein. *EMBO J* **17**, 554-564 (1998).

114. Ofir-Rosenfeld, Y., Boggs, K., Michael, D., Kastan, M.B. & Oren, M. Mdm2 regulates p53 mRNA translation through inhibitory interactions with ribosomal protein L26. *Mol Cell* **32**, 180-189 (2008).
115. Kussie, P.H. et al. Structure of the MDM2 Oncoprotein Bound to the p53 Tumor Suppressor Transactivation Domain. *Science* **274**, 948-953 (1996).
116. Vassilev, L.T. et al. In vivo activation of the p53 pathway by small-molecule antagonists of MDM2. *Science* **303**, 844-848 (2004).
117. Vu, B. et al. Discovery of RG7112: A Small-Molecule MDM2 Inhibitor in Clinical Development. *ACS medicinal chemistry letters* **4**, 466-469 (2013).
118. Andreeff, M. et al. Results of the Phase I Trial of RG7112, a Small-Molecule MDM2 Antagonist in Leukemia. *Clin Cancer Res* **22**, 868-876 (2016).
119. Chang, Y.S. et al. Stapled alpha-helical peptide drug development: a potent dual inhibitor of MDM2 and MDMX for p53-dependent cancer therapy. *Proc Natl Acad Sci U S A* **110**, E3445-3454 (2013).
120. Pazgier, M. et al. Structural basis for high-affinity peptide inhibition of p53 interactions with MDM2 and MDMX. *Proc Natl Acad Sci U S A* **106**, 4665-4670 (2009).
121. Schon, O., Friedler, A., Bycroft, M., Freund, S.M.V. & Fersht, A.R. Molecular Mechanism of the Interaction between MDM2 and p53. *Journal of Molecular Biology* **323**, 491-501 (2002).
122. Liu, Z., Olejniczak, E.T. & Fesik, S.W. Over-expression of the human MDM2 p53 binding domain by fusion to a p53 transactivation peptide. *Protein Expr Purif* **37**, 493-498 (2004).
123. Brown, C.J. et al. Stapled peptides with improved potency and specificity that activate p53. *ACS Chem Biol* **8**, 506-512 (2013).
124. Liu, M. et al. D-peptide inhibitors of the p53-MDM2 interaction for targeted molecular therapy of malignant neoplasms. *Proc Natl Acad Sci U S A* **107**, 14321-14326 (2010).
125. Vorherr, T. & Wille, R.M. Unpublished Material.
126. Tovar, C. et al. Small-molecule MDM2 antagonists reveal aberrant p53 signaling in cancer: implications for therapy. *Proc Natl Acad Sci U S A* **103**, 1888-1893 (2006).
127. Herce, H.D., Deng, W., Helma, J., Leonhardt, H. & Cardoso, M.C. Visualization and targeted disruption of protein interactions in living cells. *Nat Commun* **4**, 2660 (2013).
128. Dudgeon, D.D. et al. Characterization and optimization of a novel protein-protein interaction biosensor high-content screening assay to identify disruptors of the interactions between p53 and hDM2. *Assay Drug Dev Technol* **8**, 437-458 (2010).
129. Spiering, D., Bravo-Cordero, J.J., Moshfegh, Y., Miskolci, V. & Hodgson, L. Quantitative ratiometric imaging of FRET-biosensors in living cells. *Methods Cell Biol* **114**, 593-609 (2013).
130. Prifti, E. et al. A fluorogenic probe for SNAP-tagged plasma membrane proteins based on the solvatochromic molecule Nile Red. *ACS Chem Biol* **9**, 606-612 (2014).
131. Bach, M. et al. Fast set-up of doxycycline-inducible protein expression in human cell lines with a single plasmid based on Epstein-Barr virus replication and the simple tetracycline repressor. *FEBS J* **274**, 783-790 (2007).
132. Gibson, D.G. Enzymatic assembly of overlapping DNA fragments. *Methods Enzymol* **498**, 349-361 (2011).
133. Edelhoch, H. Spectroscopic Determination of Tryptophan and Tyrosine in Proteins*. *Biochemistry* **6**, 1948-1954 (1967).

Curriculum Vitae

CONTACT INFORMATION

Silvia Scarabelli
Avenue de Béthusy 1, 1005 Lausanne
+41767928909
silvia.scarabelli@epfl.ch

DATE AND PLACE OF BIRTH

03 October 1988, Merate (Lecco, IT)

EMPLOYMENT HISTORY

- 03/2010-04/2010 **National Research Council (CNR)** - Pisa, IT
Research Internship, Bachelor Thesis project
- 02/2011-06/2011 **Université Pierre et Marie Curie (UPMC)** - Paris, FR
Research Internship, Master 1 project
- 01/2012-06/2012 **Massachusetts Institute of Technology (MIT)** – Cambridge (MA), USA
Research Internships, Master Thesis project

EDUCATION

- 09/2002-06/2007 **Second Level College of Science** – Merate, IT
Specialization in modern languages, English and French
Final grade: 94/100.
- 09/2007-06/2010 **Bachelor's degree in Chemistry** – Pisa, IT
University of Pisa
Final grade: 110/110 cum laude
- 09/2010-06/2012 **Master's degree in Molecular Chemistry** – Paris, FR
École Normale Supérieure (ENS) – Ulm
Université Pierre et Marie Curie (UPMC)
Admission through International Selection (10 people selected/year from all over the world)
Final grade: B pass
- 11/2012-12/2016 **Ph.D. in Chemical Biology** – Lausanne, CH
École Polytechnique Fédérale de Lausanne (EPFL)

PUBLICATIONS

- [1] K.Guitot, **S.Scarabelli**, T.Drujon, G.Bolbach, M.Amoura, F.Burlina, A.Jeltsch, S.Sagan, D.Guianvarc'h, Label-free measurement of histone lysine methyltransferases activity by MALDI-TOF mass spectrometry, *Anal. Biochemistry* 456 (25-31), **2014**
- [2] **S.Scarabelli**, Ring the changes, *Research Highlights, Nature Nanotechnology*, **2013**